universität wien

MASTERARBEIT / MASTER'S THESIS

Titel der Masterarbeit / Title of the Master's Thesis

„Target Acquisition for Space Applications"

verfasst von / submitted by

Philipp Löschl, BSc

angestrebter akademischer Grad / in partial fulfilment of the requirements for the degree of

Master of Science (MSc)

Wien, 2018 / Vienna 2018

Studienkennzahl lt. Studienblatt / degree programme code as it appears on the student record sheet:	A 066 861
Studienrichtung lt. Studienblatt / degree programme as it appears on the student record sheet:	Astronomie
Betreut von / Supervisor:	ao. Univ.-Prof. Dr. Franz Kerschbaum
Mitbetreut von / Co-Supervisor:	Mag. Dr. Roland Ottensamer

Contents

1 Introduction **17**

1.1 Star Identification . . . 18

1.1.1 Early Identification Techniques . . . 18

1.1.2 Improved Search Techniques . . . 20

1.1.3 Advanced Identification Techniques . . . 21

1.2 CHEOPS - CHaracterising ExOPlanet Satellite . . . 23

1.2.1 Science Requirements . . . 23

1.2.2 Target Acquisition Requirements . . . 25

2 Target Acquisition **27**

2.1 Star Extraction . . . 29

2.1.1 Image Rebinning . . . 29

2.1.2 Pixel of Interest Selection . . . 29

2.1.3 Pixel of Interest Grouping I . . . 30

2.1.4 Pixel of Interest Group Reduction I . . . 30

2.1.5 Pixel of Interest Grouping II . . . 31

2.1.6 Pixel of Interest Group Reduction II . . . 31

2.1.7 Centre of Gravity Calculation . . . 31

2.1.8 Visualisation . . . 32

2.2 Angle Method Algorithm . . . 34

2.2.1 Star Database . . . 34

2.2.2 Matching Process . . . 42

2.3 Magnitude Validation Algorithms . . . 53

2.3.1 Magnitude Validation Algorithm (MVA) . . . 53

2.3.2 Magnitude Validation Acquisition Algorithm (MVAA) . . . 53

2.3.3 Radius Photometry . . . 54

2.3.4 Reference Target Signal Calculation . . . 56

3 Star Map Generation Tool **57**

3.1 Algorithm Parameter Determination . . . 58

3.1.1 Algorithm Selection . . . 58

3.1.2 Reference Star Selection . . . 58

3.1.3 Detection Threshold . . . 62

3.1.4 Cosmic Ray Stability . . . 63
3.2 Test Data Generation . . . 65
3.2.1 Star Coordinate Conversion . . . 65
3.2.2 Optical Distortion Simulation . . . 65
3.2.3 Star Signal Calculation . . . 67
3.2.4 Simulation with StarSim . . . 68
3.3 Target Acquisition Performance Simulation . . . 70
3.4 Star Map Generation . . . 70
3.4.1 Star Map Layout . . . 71
3.5 Visualisation . . . 72
3.5.1 Reference Frame FOV . . . 72
3.5.2 CHEOPS Frame FOV . . . 72
3.6 Input Data . . . 74
3.7 Simulation Log Files . . . 77

4 Performance Evaluation **79**
4.1 Prototype Test Campaign . . . 80
4.1.1 Brightness Distribution Model . . . 80
4.1.2 Star Extraction Performance . . . 81
4.1.3 Angle Method Performance . . . 83
4.1.4 Prototype Test Conclusions . . . 86
4.2 Performance Test Campaign . . . 87
4.2.1 Off Centre Acquisition Test . . . 88
4.2.2 Large Offset Test . . . 90
4.2.3 True Jitter Precision Test . . . 96
4.2.4 SAA Extreme Cosmic Ray Test . . . 97
4.2.5 Maximum Rotation Test . . . 98
4.2.6 Execution Times . . . 99
4.2.7 Performance Test Conclusions . . . 103
4.3 Science Case Test Campaign . . . 104

5 Conclusion **107**

List of Figures

1-1 FOV-sized sub catalogues 19
1-2 Liebe star pattern extraction 19
1-3 Quine's binary tree 20
1-4 *k-vector* construction 21
1-5 Padgett's grid pattern 22
1-6 CHEOPS spacecraft rendering 26
1-7 Roll around inertially fixed LoS direction 26

2-1 Step by step visualisation of the Star Extraction process. 33
2-2 General fingerprint construction 35
2-3 Fingerprint construction for the Observed Star Database 38
2-4 Ambiguous Fingerprint from Backup Reference Star 45
2-5 Effects of single interloping stars on the Observed Star Database. 50
2-6 Effects of two interloping stars on the Observed Star Database. 50
2-7 Simulated PSF shape 55
2-8 Real PSF shape 55

3-1 FOV grouping for the star selection 60
3-2 Reference star selection for the Angle Method Algorithm. 62
3-3 Cosmic Ray Flux in the SAA 64
3-4 CHEOPS Distortion Map 66
3-5 Visual output of the *SMGT* as seen by the operator 73

4-1 Cumulative Brightness Distribution of the Kepler Input Catalog. 80
4-2 Star Extraction Performance 82
4-3 Random FOV Angle Method Performance 84
4-4 Orientation Specific Angle Method Performance 85
4-5 TA_FF_01_verylarge_offset_09mag_10s_2_medium results 88
4-6 TA_FF_01_verylarge_offset_09mag_10s-CORNER_2_medium results 89
4-7 TA_FF_01_large_offset_06mag_01s_3_extreme results 90
4-8 TA_FF_01_large_offset_09mag_10s_2_medium results 91
4-9 TA_FF_01_large_offset_09mag_10s_3_extreme results 92
4-10 TA_FF_01_large_offset_12mag_60s_1_low results 93
4-11 TA_FF_01_large_offset_12mag_60s_2_medium results 94

4-12 TA_FF_01_large_offset_12mag_60s-ALT2_3_extreme results 95
4-13 TA_FF_01_true_jitter_09mag_10s_3_extreme results 96
4-14 TA_FF_01_true_jitter_09mag_10s_CR1000x_2_medium results 97
4-15 TA_FF_01_true_jitter_12mag_60s_MAXROT_3_extreme results 98
4-16 Target Acquisition Configuration Success 104
4-17 Duplicate Corrected Target Acquisition Configuration Success 105

List of Tables

1.1 CHEOPS Science Requirements 24
1.2 CHEOPS Target Acquisition Requirements 25

2.1 Fingerprint Set for the Reference Star Database. 36
2.2 Reference Star Database with Fingerprints for Fig.: 2-2 37
2.3 Fingerprints with uncertainties for the Observed Star Database 40
2.4 Observed Star Database with fingerprints for Fig.: 2-3 41
2.5 Raw Match Results 43
2.6 Translated Match Results 43
2.7 Match Results Histogram 44
2.8 Cross Base Correction for the Match Results Histogram 45
2.9 Base Star Correction Example 46
2.10 Difficult Match Result Validation 47

3.1 Cosmic Ray Signal Deposition 63
3.2 Magnitude to ADU conversion parameters 67
3.3 The detailed contents of the Star Map Telecommand. 71
3.4 Contents of a typical star catalogue FITS file. 75

4.1 TA_FF_01_verylarge_offset_09mag_10s_2_medium parameters 88
4.2 TA_FF_01_verylarge_offset_09mag_10s-CORNER_2_medium parameters . 89
4.3 TA_FF_01_large_offset_06mag_01s_3_extreme parameters 90
4.4 TA_FF_01_large_offset_09mag_10s_2_medium parameters 91
4.5 TA_FF_01_large_offset_09mag_10s_3_extreme parameters 92
4.6 TA_FF_01_large_offset_12mag_60s_1_low parameters 93
4.7 TA_FF_01_large_offset_12mag_60s_2_medium parameters 94
4.8 TA_FF_01_large_offset_12mag_60s-ALT2_3_extreme parameters 95
4.9 TA_FF_01_true_jitter_09mag_10s_3_extreme parameters 96
4.10 TA_FF_01_true_jitter_09mag_10s_CR1000x_2_medium parameters 97
4.11 TA_FF_01_true_jitter_12mag_60s_MAXROT_3_extreme parameters 98
4.12 Execution Times AMA 100
4.13 Execution Times MVA 101
4.14 Execution Times AMA & MVA 102
4.15 CHEOPS Science Team GTO Target List acquisition results 106

List of Acronyms

ADU	Analog Digital Unit
AMA	Angle Method Algorithm / Angle Method Acquisition
AOCS	Attitude and Orbital Control System
APE	Absolute Pointing Error
CCD	Charge Coupled Device
CHEOPS	CHaracterising ExOPlanet Satellite
CoG	Center of Gravity
CR	Cosmic Ray
DPU	Data Processing Unit
E-ELT	European Extremely Large Telescope
ESA	European Space Agency
FOV	Field of View
HST	Hubble Space Telescope
IFSW	Instrument Flight Software
JPL	Jet Propulsion Lab
JWST	James Webb Space Telescope
KIC	Kepler Input Catalog
MVA	Magnitude Validation Algorithm / Magnitude Validation Acquisition
MVAA	Magnitude Validation Acquisition Algorithm
ODB	Observed Star Database
OTA	Optical Telescope Assembly
POI	Pixel of Interest
PSF	Point Spread Function
RDB	Reference Star Database
ROI	Region of Interest
SAA	South Atlantic Anomaly
SE	Star Extraction
SMGT	Star Map Generation Tool
SOC	Science Operations Center
SSO	Sun-Synchronous Orbit
TESS	Transiting Exoplanet Survey Satellite

Abstract English

The prerequisite for any astronomical high precision observation is accurate knowledge of the telescope pointing. While this can be a difficult task to achieve for ground based observatories, it is especially challenging for the case of space telescopes due to their non stationary nature. The requirements for pointing accuracy are mission and observation dependent and are usually achieved with specialised attitude determination hardware such as star trackers or sun sensors. In some cases, it can also be necessary to further improve the pointing by the utilisation of the science instrument. Thus, observations with the final pointing are used to verify or improve the achieved accuracy. The CHaracterising ExO-Planet Satellite (CHEOPS) is such a case. It will perform ultra high precision photometry of stars that are confirmed hosts of exoplanets on a 3-axis stabilised sun-synchronous orbit. While this orbit is optimised for uninterrupted observations at minimum stray light conditions, it will periodically introduce thermal variations during close approaches for perigee passes. As a result, thermo-elastic deformations between the spacecraft bus and the optical telescope assembly will affect the alignment between the star trackers and the payload instrument. This introduces a periodic high pointing uncertainty, which will not only interfere with the reliable placement of the target star on its intended location, but also its respective identification. Therefore, an additional acquisition system for a distinct target identification became crucial for the nominal mission operation. In its current implementation it consists of software to locate star positions on observed full frame images and two independent star identification algorithms, which are designed to identify the target star by its photometric or the geometric properties of the surrounding field of view (FOV).

The main acquisition algorithm was built upon an algorithm that was originally developed for the use in star trackers that operate in lost in space scenarios, where no initial attitude information is available. It was adapted and optimised for the special case of CHEOPS, where an initial attitude up to a maximum pointing error is available for each observation. The design, implementation and configuration of said acquisition system is subject of this thesis, which is meant to be a compendium for the CHEOPS science operations staff. In addition, it features a detailed description of the various test campaigns that verified the optimal performance under all anticipated conditions.

Abstract German

Genaue Information über die aktuelle Ausrichtung eines Teleskops ist seit jeher die Voraussetzung für hochpräzise astronomische Beobachtungen. Während dies schon für erdgebundene Teleskope schwierig sein kann, ist es bei weltraumbasierten Teleskopen, aufgrund ihrer ständigen Orbitalbewegung, eine besondere Herausforderung. Die Anforderungen an die Genauigkeit sind dabei von Mission zu Mission unterschiedlich und werden in der Regel mit spezieller Hardware für die Lagebestimmung erfüllt. Dabei können dedizierte Instrumente wie Stern- oder Sonnensensoren, oder aber auch die wissenschaftliche Instrumentierung direkt zum Einsatz kommen. Im letzteren Fall wird nach der anfänglichen Ausrichtung die erzielte Lage mit dem Teleskop erneut vermessen und bestätigt bzw. gegebenenfalls korrigiert. Der Characterising ExOPlanet Satellite, oder auch CHEOPS genannt, ist ein Fall, wo diese Technik zum Einsatz kommt. CHEOPS ist für ultrahochpräzise Photometrie von Sternen mit bekannten Exoplaneten konzipiert und wird die Erde in einem 3-Achsen stabilisierten sonnensynchronen Orbit umkreisen. Dieser Orbit wurde zwar für ungestörte Beobachtungen bei minimalem Streulicht optimiert, ist bei Perigäumsdurchgängen allerdings thermischen Schwankungen ausgesetzt. Daraus entsteht eine periodische thermoelastische Deformation zwischen der Teleskopstruktur und dem Service-Modul, welche die präzise Ausrichtung zwischen den Sternsensoren und dem Teleskop beeinflusst und in weiterer Folge eine genaue Platzierung des beobachteten Sterns am CCD verhindert. Da der beobachtete Stern damit nicht auf der geplanten CCD Position abgebildet wird, ist es für die wissenschaftlichen Beobachtungen notwendig diesen über ein dediziertes Sternerkennungssystem zu finden und die Ausrichtung dementsprechend zu korrigieren. Dieses System wurde softwareseitig implementiert und besteht aus Softwarekomponenten zur Sterndetektierung und zwei unterschiedlichen Algorithmen, um die Sterne am Nachthimmel mittels geometrischen und photometrischen Eigenschaften eindeutig zu identifizieren. Der vermutlich hauptsächlich benutzte geometrische Identifikationsalgorithmus wurde ursprünglich für den Einsatz ohne jegliche Information zur momentanen Ausrichtung in Sternsensoren konzipiert. Da diese für CHEOPS bis auf einen bekannten maximalen Ausrichtungsfehler vorhanden ist, wurde er entsprechend adaptiert und optimiert. In dieser Masterarbeit wird das Design, die Implementierung und Konfiguration dieses maßgeschneiderten Sternerkennungssystems präsentiert. Zusätzlich wurden Leistungstests unter verschiedensten Beobachtungsbedingungen durchgeführt, um den reibungsfreien Einsatz zu garantieren.

Acknowledgements

First and foremost, I want to express my sincere gratitude to my supervisor ao. Univ.-Prof. Dr. Franz Kerschbaum for the unique opportunity and the generous funding to work on this exciting project.

Furthermore, I want to thank my co-supervisor Mag. Dr. Roland Ottensamer for all the helpful discussions, advices and invaluable insights into the sometimes peculiar nature of programming spacecraft.

I owe my deepest gratitude to my parents for their continuous support to this day. Thank you for never questioning my unusual choice of studies, even though you never fully understood what I'm actually doing.

Very special thanks goes to my lovely girlfriend Elisabetta. Thank you for all the work that you've taken off my shoulders during this thesis and especially for keeping me sane during the recent extraordinary accumulation of hardships in my family.

I also want to mention my fellow colleagues Christoph, Markus and Roman. Thank you for all the fun and challenges we had in pushing ourselves to overcome unrealistically large workloads during our first semesters. Especially to Roman, who spent a lot of time proof reading this work and whose own thesis has become an integral part of this project.

Another honorary mention goes to Dr. Nicolas Billot from the Université de Genève. Thank you for all your beta testing, valuable inputs and test data. This software certainly wouldn't be what it is today without you.

Last but not least, I want to thank my piano teacher Ronald for introducing me to jazz and in particular the wonderful works of Miles Davis. You have made the countless hours of hard work a lot more enjoyable.

This project was funded through the ESA PRODEX contract C4000112123.

1 Introduction

The problem of obtaining and maintaining a correct pointing to observe celestial objects has accompanied astronomers since the invention of the first observational instruments. While this can already be challenging for ground based telescopes, it is especially true for space based observatories with their constantly changing attitudes. For this reason, spacecraft usually have some form of dedicated Attitude and Orbit Control System (AOCS), which utilises sensors (star tracker, sun sensors, horizon sensors) and actuators (reaction wheels, thrusters, magnetorquers) to determine, maintain and change the vehicle's attitude [Larson & Wertz, 2013]. A common and currently the best method, is the use of star trackers [Zhang, 2016]. These are dedicated star cameras that try to identify imaged star positions with known positions in a star catalogue. In combination with algorithms such as QUEST or TRIAD [Shuster & Oh, 1981] the current attitude can be calculated and compared to its desired state. The requirements to the precision of such system varies greatly with each mission's specific science objectives. In some cases, the AOCS will not suffice to provide the required precision, due to various reasons that include, but are not limited to a financial or mechanical nature. A potential remedy for such insufficient attitude determination can be the inclusion of the payload instrument as a means to discover and correct a poor initial pointing. An example for such a case is the CHaracterising ExO-Planet Satellite (CHEOPS). Here, the mechanical mount structure of the optical telescope assembly is subject to periodic thermo-elastic deformations. This leads to a varying pointing error and demands the utilisation of the payload in the position correction [Benz et al., 2013]. In the context of this thesis, I will give an overview of different approaches to the star identification problem and present a software based pointing correction in the form of the dedicated CHEOPS target acquisition system. Following up on this, I will focus on the configuration and verification of the software and conclude with the qualification test results.

1.1 Star Identification

The research topic of star identification has been an ever evolving one since spacecraft computers became powerful enough to succeed the traditional ground station tracking that has been used for real-time orbit determination in the past. This section will give a short introduction to the milestones in the development of star identification algorithms in a historical order. Generally, these algorithms can be divided into two categories. The *lost-in-space algorithms*, that don't have any prior knowledge to the spacecraft attitude and the *recursive algorithms*, which work based on initial attitude information [Spratling & Mortari, 2009]. The first kind is used for initial attitude determination and the second as a follow-up for guiding operation. While star identification techniques come in many different varieties, they are typically built around specific features that are derived from inter-star angles and star brightnesses. These are built from the star positions of acquired images and subsequently compared to feature databases which comprise selected objects from existing star catalogues. The main difference between the *lost-in-space* and *recursive* algorithm, but also generally amongst the various methods, lies in the whole sky completeness of the databases and ability for fast search operations within them.

1.1.1 Early Identification Techniques

The first CCD-based star tracker evolved from earlier concepts that were used for missile guidance systems and was developed at NASA's Jet Propulsion Lab (JPL) by Salomon & Goss [1976]. Soon afterwards this lead Junkins et al. [1977] to work on the first star identification algorithm to be used in such a device and was eventually published as *"Star Pattern Recognition and Spacecraft Attitude Determination"* [Strikwerda & Junkins, 1981]. This first of its kind method measured the sine of the inter-star angles of a possible permutation of star triplets in the FOV and tried to match them with a catalogue which included all combinations of stars that are expected to be observed. Due to high execution times of search queries for whole sky catalogues ($\mathcal{O}(f^3)$ where f is the number of stars in the FOV), it was limited to operation with a priori estimates for the spacecraft's attitude and thus the use of sub-catalogues that only contain the relevant portion of the sky (Fig.: 1-1). Further developments to this approach tried to address the query times by sorting the catalogues [Groth, 1986] and alternative features made up from the area of a star triangle and the sum of their luminous intensities [Sasaki & Kosaka, 1986].

The *lost-in-space* problem eventually became feasible when Liebe [1992] suggested to limit the feature selection to be built from a star and his two closest neighbours rather than any arbitrary number of star triplets. For this, he used the angular separation of a star and

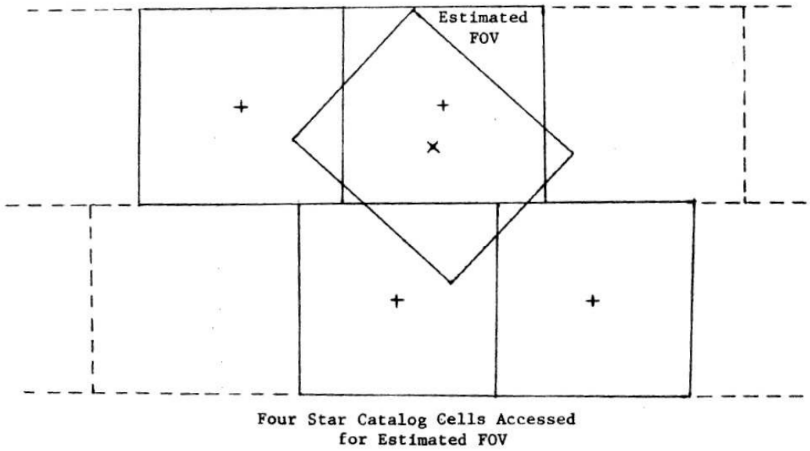

Figure 1-1: FOV-sized sub catalogues (reprinted from Strikwerda & Junkins [1981]).

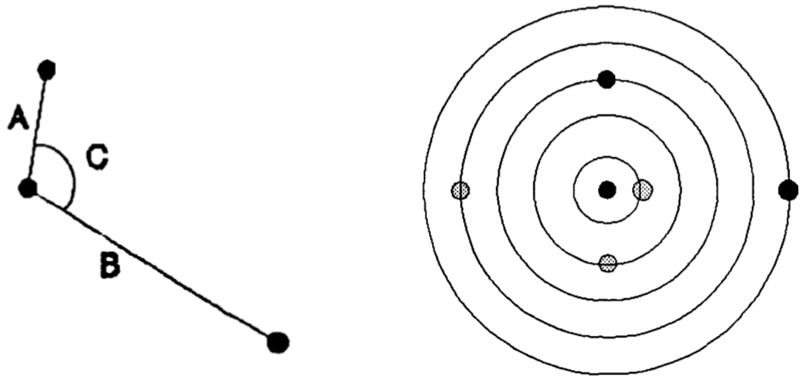

Figure 1-2: Liebe star pattern extraction with the inter-star distances A, B and the angle C (left). Selection of backup pattern (black) for non-guaranteed star detections (gray)(right) (reprinted from Liebe [1992]).

the two neighbours, as well as the angle between them. His features also included backup patterns with the next close stars if the closest are in doubt to be guaranteed detections. Consequently this dramatically reduced the database search times from $\mathcal{O}(f^3)$ to $\mathcal{O}(n)$, where n is the number of stars in the catalogue for which patterns are built. The feature extraction process is illustrated in Fig.: 1-2

Many of the following algorithms, including Baldini et al. [1993], built upon this method in one way or another. His approach was to take Liebe's inter-star distances but measured five angular separations from a sequence of the brightest b stars in the FOV. In an attempt to reduce search times, his algorithm built dynamic sub-databases that would only include features within an acceptable tolerance Δm of his measured separations. Combining the initial search time for the $\mathcal{O}(bn)$-sized sub database creation and the successive search of these $\mathcal{O}(\Delta mn)$, results in a total search time of the order of $\mathcal{O}(b(\Delta mn)^2)$. Therefore, this

method may be superior to Liebe's in terms of identification success but stays behind on execution times.
The same is true for an approach presented by Scholl [1995], who suggested to order all inter-star distances by their relative brightness, thus eliminating any permutations of the star triplet combinations. While his $\mathcal{O}(nf^2)$ sized catalogues and search time are also inferior to Liebe's method, they still represent an upgrade to the initial work by Strikwerda & Junkins [1981].

1.1.2 Improved Search Techniques

After numerous attempts to optimise identification times with new features, Quine & Durrant-Whyte [1996] were the first to solely address the search times. By using Liebe's method for feature extraction, they restructured the star pattern database in the form of a binary tree to utilize a binary search algorithm. This resulted in dramatically reduced search times of $\mathcal{O}(\log_2 n)$. His tree structure can be seen below in Fig.: 1-3.

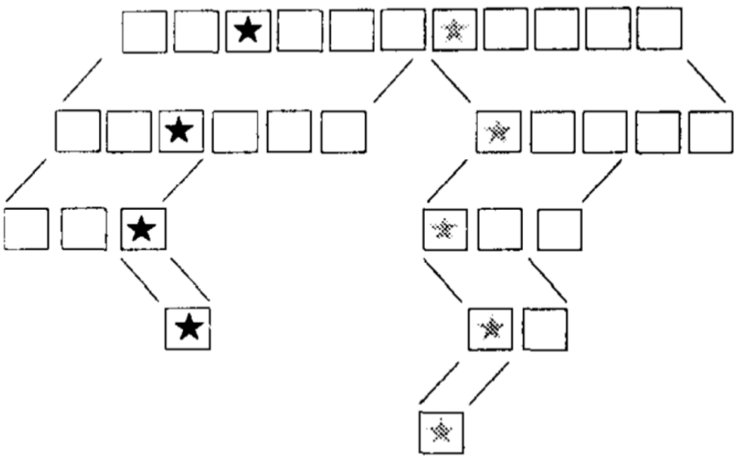

Figure 1-3: Binary tree feature database as used by Quine. (reprinted from Quine & Durrant-Whyte [1996]).

The second leap in search time improvements was the *"Search Less Algorithm"* as proposed by Mortari [1996], 1997 and 2000. This introduced the so-called *"k-vector"*, which is a tool to constrain the search operation to certain regions of the pattern database, thus making the search time independent of the database size. An example for this is given in Fig.: 1-4. Here a *k-vector* $(0,2,2,3,3,5,6,8,9,10)$ for a 10-element database is created. Each element in k represents the number of entries below one of equally spaced values, which range describes stored features in the pattern database. This method reduces search times down to $\mathcal{O}(bk^2)$, where b represents the number of stars in the pattern. Here k can be associated with the number of potentially matching inter-star distances and depends on the measurement uncertainty based quantisation of the database entries.

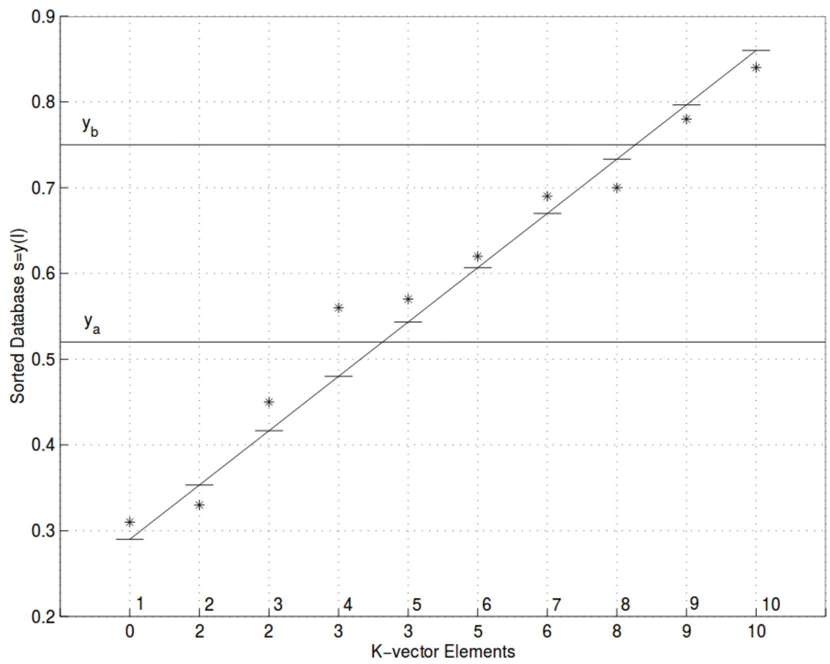

Figure 1-4: *k-vector* construction for the given example (reprinted from Mortari & Neta [2000]).

1.1.3 Advanced Identification Techniques

The first real novel approach that featured an actual pattern and that did not rely on the classical inter-star distances was the *Novel Grid Algorithm* suggested by Padgett & Kreutz-Delgado [1997]. Padgett's method centers the star positions in a FOV around the star in question and reorients all other stars so that its closest neighbour is aligned with the x-axis. The pattern is then formed by laying a loose grid over the stars, for which all grid cells that contain a star are considered to be *on* and the rest *off* (Fig.: 1-5). These binary grid patterns will be created for every object that should be identifiable with the feature database. While the method itself was quite robust to interloping stars, its downside was that the search times could not be improved beyond linear ($\mathcal{O}(n)$).

Further notable work includes a method with pyramid based features by Mortari et al. [2004] that is designed to work with his earlier developed *k-vectors*. This initially builds a triangle from a star triplet as the pyramid base. The inter-star distances within the triangle are then used to construct a *k-vector* that constrains the feature database for the combination with another star that will be the tip of the pyramid. Though demonstrated to be a reliable and quick method [Brady et al. [2002] & Crew et al. [2002]], it could not be used, since it is presently under an exclusive contract.

While most of the above methods were developed in cooperation with NASA or ESA, new

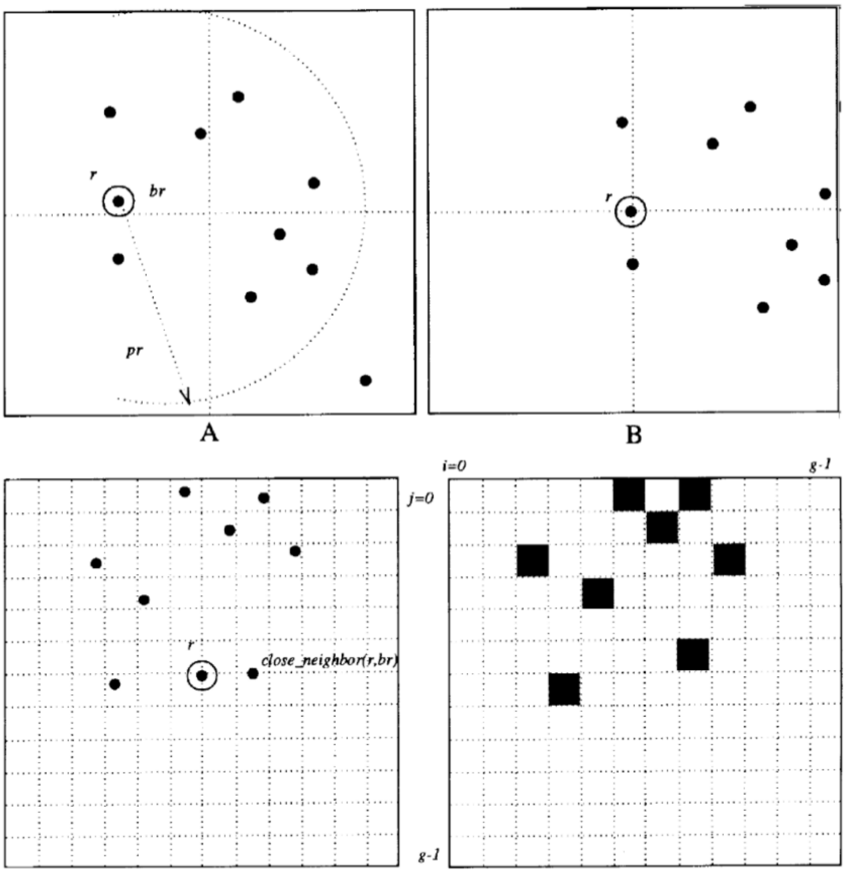

Figure 1-5: Binary grid construction (reprinted from Padgett & Kreutz-Delgado [1997]).

advances have been made in the vicinity of the Chinese space programme. For example Zhang et al. [2008], who proposed a method similar to Liebe [1992] with the difference that it builds the feature catalogue around combinations relative to a central star.

Finally, an idea that might become viable in the future is star identification based on neural networks. Though they have been repeatedly proposed over the last decades (Alvelda & Martin [1989], [Hong & Dickerson, 2000]) and recent advances in machine learning and computer vision are promising, the necessary large parallel CPU architectures are currently not available for spacecraft certified hardware.

With plenty of different approaches to the star identification problem, this introduction was limited to identification methods that have influenced and/or include approaches suitable for future improvements for the work which will be presented in the remainder of this thesis. A more thorough introduction is provided by Spratling & Mortari [2009].

1.2 CHEOPS - CHaracterising ExOPlanet Satellite

The CHaracterising ExOPlanet Satellite (CHEOPS) is the first ESA S-class mission and will be dedicated to perform ultra-high-precision photometry on bright stars that were confirmed to host exoplanets by high-precision Doppler spectroscopic surveys. Being designed as a follow-up mission for targets with known masses its prime mission goals are [Benz et al., 2013]:

- **Performing first-step characterisations of super-Earths** by measuring the radius, density and inferring the presence or absence of a significant atmospheric envelope for super-Earths.
- **Obtaining new insights into the physics and formation processes of Neptunes** by measuring accurate radii and precise densities as well as constraining their gas mass fractions.
- **Building a collection of "golden targets" for exoplanetology** by finding targets of interest for further follow-up observations with ground based telescopes like the *European Extremely Large Telescope (E-ELT)* as well as the *Transiting Exoplanet Survey Satellite (TESS)* and the *James Webb Space Telescope (JWST)*

  .

Furthermore, CHEOPS' secondary goals include the

- **Estimation of the albedo and cloud coverage of hot Jupiters** by measurements of the phase modulation of reflected light along the orbit of short-period giant planets.
- **Search for co-aligned, inner and smaller planets in systems with transiting Neptunes** by the observation of transit time variations.

These will put it into a unique position to give new insights into planetary formation and general exoplanetology. This will be achieved by transit photometry with a defocused 32 *cm* Ritchey-Chrétien telescope, that features a 0.4° FOV on a back-illuminated 1k CCD. In addition, a custom baffling system against straylight combined with a passive cooling as well as an active heating system for the CCD will provide stable observational conditions to achieve the necessary photometric precision. The mission is planned to perform observations from a Sun-synchronous orbit (SSO) with an altitude of 650-800 km at 98° inclination and an orbital period of about 100 min.

1.2.1 Science Requirements

The science requirements of the CHEOPS mission are divided into two levels, top level requirements (L1) and derived requirements (L2). The list in Tab.: 1.1 is a selection of the requirements that include the relevant information for the remainder of this thesis. For the full detailed list see Benz et al. [2013].

Photometric accuracy

SciReq 1.1	**Photometric precision for transit detection (L1)** CHEOPS shall be able to detect Earth-size planets transiting G5 dwarf stars [. . .] with V-band magnitudes in the range $6 \leq V \leq 9$ mag. [. . .] this requires achieving a photometric precision of 20 ppm [. . .]
SciReq 1.2	**Photometric precision for characterisation (l1)** C CHEOPS shall be able to detect Neptune-size planets transiting K-type dwarf stars [. . .] with V-band magnitudes as faint as $V = 12$ mag (goal: $V = 13$ mag). [. . .] a photometric precision of 84 ppm is to be obtained [. . .]
SciReq 1.3	**Point spread function (L2)** The point spread function (PSF) of CHEOPS shall be adjusted (e.g. defocused) as a function of the flat field precision (SciReq 1.4) and the pointing accuracy (SciReq 1.6) to reach the required photometric precision (SciReq 1.1, SciReq 1.2).
SciReq 1.4	**Flat-field precision (L2)** The flat field shall be measured down to a pixel-to-pixel precision of $\sigma_{ff} = 0.1\%$.
[. . .]	
SciReq 1.6	**Pointing Accuracy (L2)** CHEOPS pointing accuracy during observations shall be better than $8''$ rms. *[. . .] the half cone angle between the actual and desired payload line of sight (LoS) directions shall have an absolute performance error (APE) less than 8 $''$ at 68% confidence [. . .]*
[. . .]	

Target observability

[. . .]	
SciReq 3.2	**Earth stray light exclusion angle (L2)** In order to limit stray light contamination, the minimum angle allowed between the line-of-sight and any (visible) illuminated part of the Earth limb, the so-called *Earth stray light exclusion angle*, shall be 35° (goal: 28°).
SciReq 3.3	**Sun exclusion angle (L2)** The Sun must be outside the cone around the line of sight (LoS) of the telescope having a half-angle, the so-called *sun exclusion angle*, of 120°.
SciReq 3.4	**Moon exclusion angle (L2)** The bright Moon must not be inside a cone around the line-of-sight of the telescope having a half-angle, the so called *moon exclusion angle*, of 5°.

Magnitude range of targets and exposure times

SciReq 4.1	**Bright-to-faint target magnitudes (L1)** CHEOPS shall be able to observe bright to faint stars with V-band magnitudes in the range $6 \leq V \leq 12$ mag with the photometric precisions given in SciReqs 1.1 & 1.2.
SciReq 4.2	**Very bright target magnitudes (L1)** CHEOPS shall be able to obtain light curves from very bright stars down to a V-band magnitude of $V = 0$ mag. *There is no requirement on the photometric precision for such targets*
SciReq 4.3	**Exposure times (L1)** The exposure times for targets in the magnitude range defined in SciReq 4.1 shall range from 1 to 60 seconds.
[. . .]	

Table 1.1: Selected CHEOPS science requirements [Benz et al., 2013]

1.2.2 Target Acquisition Requirements

In an attempt to reach the desired pointing accuracy from SciReq 1.6 (Tab.: 1.1), the optical telescope assembly (OTA) was mounted onto a special carbon-fibre reinforce polymer structure. This is meant to reduce the susceptibility of the instrument to thermal variations that CHEOPS might experience in near-Earth orbit. Unfortunately, the requirements for the initial absolute pointing error (APE) could not be met with the final design and selection of the existing AS-250 platform for the spacecraft bus (Fig.: 1-6). The in-orbit thermal variations are now expected to introduce thermo-elastic deformations between the OTA and the bus, which will be strong enough to affect the alignment between the star trackers and the telescope. As a consequence both, the pointing stability and the initial APE will be degraded. While an upgrade to higher quality star trackers solved the issue with the pointing stability requirements, an additional AOCS software that utilises the instrument "in-the-loop" became necessary to address the APE[1], which can be as high as $180''$. This AOCS software is the previously mentioned *Target Acquisition System* that is subject of this thesis. The requirements for the design of the *Target Acquisition System* are listed in Tab.: 1.2.

TAcReq 1	**Initial absolute pointing error** The maximum initial absolute pointing error shall not exceed $180''$.
TAcReq 2	**Resulting pointing accuracy** The target star shall be identified within a pointing accuracy better than $8''$.
TAcReq 3	**FOV rotation** The algorithm shall be invariant to the FOV rotation caused by roll around the inertially fixed LoS direction. *This is required to ensure that the instrument radiator constantly points to cold space (see Fig.: 1-7).*
TAcReq 4	**Isolated target detection** The PSF of the target star shall not overlap with the signal of any other celestial object.
TAcReq 5	**Target Acquisition execution times** The target acquisition shall not exceed 3s to identify the target (initially was 1s).
TAcReq 6	**Cosmic ray stability** Target acquisition in the South Atlantic Anomaly (SAA) shall be possible until the flux of protons with energy > 50 MeV will exceed 2 $p^+/cm^2/s$. *This corresponds to the flux where science data will be deemed unusable and hence discarded.*

Table 1.2: CHEOPS Target Acquisition Requirements

The necessary design choices to combine the above requirements with the earlier introduced star identification methods, as well as the detailed description of the resulting implementation will be described in the next chapter.

[1] Simulations for the APE cannot be referenced due to NDA restrictions of the manufacturer.

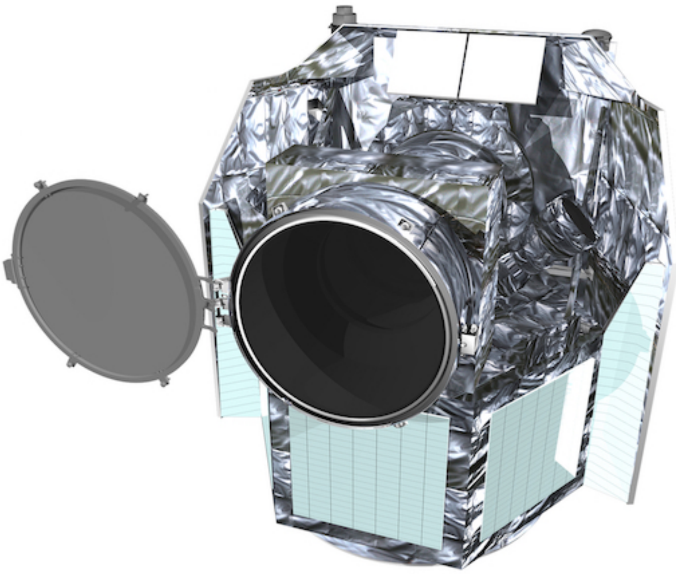

Figure 1-6: Artist impression of CHEOPS. Note the bus mounted star tracker below the OTA on the right side [Benz et al., 2013].

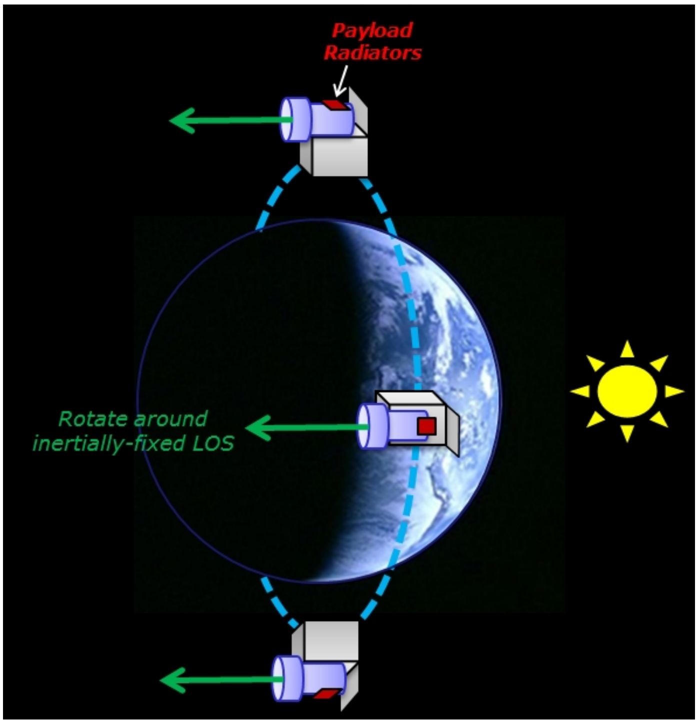

Figure 1-7: Roll around inertially fixed LoS direction [Benz et al., 2013].

2
Target Acquisition

The *Target Acquisition* consists of an initial *Star Extraction* algorithm that calculates star positions in a given image and is followed by one of two star identification algorithms. These include a simple photometric identification method, the *Magnitude Validation Algorithm* and a more complex geometrical identification, the *Angle Method Algorithm*. The latter was tailored to the target acquisition requirements (see section 1.2) and incorporates various ideas from different star identification approaches by Junkins, Liebe, Mortari and Zhang as introduced in section 1.1. In the early stages of the identification algorithm selection, Padgett's *Grid Algorithm* was also considered and implemented until its prototype stage. Even though initial tests produced good identification results, it was eventually discontinued due to concerns regarding its reliability and automated configuration for sparsely populated narrow FOVs. A detailed description of the *Grid Algorithm* prototype can be found in Loeschl et al. [2016].

The acquisition process is autonomously performed by CHEOPS and configured via the *Star Map Command* (section 3.4). This telecommand is configured for each observation by an operator in the ground segment. It is created by the *Star Map Generator Tool* (chapter 3) and contains observation specific information with all necessary parameters. At the start of every acquisition, the on-board routine (service 196.2) starts with memory allocation for all the variables required in the acquisition algorithm. Once they are in place, it receives the latest image data for the current observation as well as the respective acquisition algorithm parameters from the *Star Map Command*. This information is then used to scale the time dependent quantities such as the *reference target signal*, *background signal* and *detection thresholds* to the respective exposure time of the current observation.

After this preparation, each acquisition process continues as follows:

Star Extraction → Distortion Correction → Identification Algorithm

The *Star Extraction* is the first step for each acquisition and it is independent of the subsequent target identification methods. Then a distortion correction (see section 3.2.2) for the positions becomes necessary, as the optical distortion is strong enough that they might not be recognised by the *Angle Method*. The acquisition process is concluded with the execution of one of the identification algorithms. Their selection is observation specific and is decided by the operator during the parameter configuration for each *Star Map Command*. There are three possible options that are FOV specific and depend on their star density and distribution:

- Magnitude Validation Acquisition (MVAA)
- Angle Method Acquisition (AMA)
- Angle Method Acquisition + Magnitude Validation Algorithm (AMA + MVA)

More in depth information on the algorithms is given in their respective sections 2.2 and 2.3.

2.1 Star Extraction

The *Star Extraction* is the first step for every algorithm in the *Target Acquisition* routine. Its main task is to detect stars and measure their positions on the full frame images in CCD pixel coordinates. These positions are a crucial prerequisite for every subsequent type of target identification algorithm. Therefore, the *Star Extraction* is not only provided with the full frame image data, but also uses observation specific information such as a detection threshold for individual pixels, a detection threshold for the signal of the integrated point spread function (PSF) and an estimated background signal. The process is loosely based on [Bertin & Arnouts, 1996] and can be outlined by the following steps:

- Image Rebinning
- Pixel of Interest Selection
- Pixel of Interest Grouping I
- Pixel of Interest Group Reduction I
- Pixel of Interest Grouping II
- Pixel of Interest Group Reduction II
- Centre of Gravity Calculation

A detailed description for each step is provided in their dedicated subsections below.

2.1.1 Image Rebinning

In order to meet the *Target Acquisition* execution time requirement of three seconds (see TAcReq 5, Tab.: 1.2) the full frame image is rebinned by a factor 8 on both axes for any further use by the Star Extraction. This reduces the overall memory usage and increases the speed of any iteration over all image pixels by a factor of 64. In addition, it concentrates the spread out PSF of the stars to a more compact signal distribution within approximately binned 3×3 pixel, which makes it easier to locate.

2.1.2 Pixel of Interest Selection

Next, the rebinned image is scanned for pixels that exceed the *pixel detection threshold* (PDT). This PDT describes the minimum fraction of the signal that will be concentrated into the brightest rebinned pixel and is determined by simulating all possible orientations[1] on the rebinned grid. For the current PSF[2] this is about 20.29 % of the full signal. The coordinates of all eligible pixels are stored as *pixel of interest* (POI) for further processing. POI selection for observations with increased exposure times, as is the case with very faint targets, often come with an increased number of detected stars due to higher star densities. Since by design, memory for only 60 positions is reserved, the number of star detections

[1] Simulated with *Binned_Signal_Distribution.py* as provided by the *Star Map Generation Tool*
[2] Based on PSF_Z1.75mm_ima_bicubic_spline_corr_no_neg_norm_41x41.txt

has to be limited to this maximum. While this can usually be solved with increased detection thresholds, it is not always possible for observations of faint targets. Instead, the area on which the Star Extraction operates can be decreased. This is done with the *reduced extraction radius*, which limits the POI selection area to a circular subframe around the expected target location. Although it is not used under nominal observation conditions, it can become a necessity for very crowded FOV or smeared FOV. The latter is caused by image rotation, for which an exclusion of radially outward and smeared objects can be beneficial to avoid the possibly large position errors, that could interfere with the star identification algorithms.

2.1.3 Pixel of Interest Grouping I

The *pixel detection threshold* is defined such that multiple pixels will be detected within the signal distribution of relatively brighter stars. This behaviour is a direct result of the threshold definition, which is such that the corresponding faintest detectable magnitude will trigger at least one *pixel of interest*. To avoid multiple detections of single stars, it is necessary to reduce the POI to one per object. Therefore, close-by pixels within a distance of the typical rebinned PSF diameter are grouped together. Assuming a 3 x 3 pixel PSF, where all 9 pixels are identified as POI, two pixels threshold in the x and y directions are required for the grouping.

The row wise scanning process in the previous steps started in the lower left corner of the image array. As a consequence, all POI are sorted after their xy-coordinates, which minimises memory access for the grouping algorithm. Initially all POI are assigned to group -1, which indicates that they are not grouped yet. Then starting with the first, each POI position is compared to all following ungrouped positions in the POI list. If their separation is below the distance threshold they are assigned to the same group. This process repeats until each POI has been assigned to a group and conserves the order of the POI list.

2.1.4 Pixel of Interest Group Reduction I

With every *pixel of interest* assigned to a group and therefore a specific star, each group of POI can now be reduced to a single POI per object. Iterating over all available groups, the POI list is scanned for all other pixels associated with the respective group. The retrieved pixel coordinates in each group can then be averaged to a single and central POI. As a result of this operation most star locations are now described by this central single POI.

2.1.5 Pixel of Interest Grouping II

Long exposure times for bright stars can trigger *pixels of interest* on larger areas than the anticipated 3 x 3 pixel frame. Consequently and despite the reduction in the previous step, this can cause multiple reduced POI to describe the same star. To avoid the associated degradation of identification algorithm results from such multiple detections, the remaining POI are grouped again as described before. Since the POI should mostly be centered on their stars at this stage, a more rigorous separation criteria of four pixels can be employed. Other than that, the grouping process is identical to its first iteration.

2.1.6 Pixel of Interest Group Reduction II

The second *pixel of interest* reduction process is slightly different to the first one. Instead of averaging the POI positions for each group, the pixel signals are considered now. This is superior to geometric averaging, due to the changed nature of the remaining pixels. While the first grouping process is meant to work with POI that are spread all over the PSF, the distribution after the first reduction is different. If a star is described by multiple groups at this point, it most likely has one group with a POI in its centre and a second group with POI at the outer edge. Since the signal is concentrated in the central region of the rebinned PSF, it is the better indicator to find the best POI. Averaging the position instead would introduce a systematic positional offset for such cases. For this reason, the algorithm iterates over all available POI in each group and sorts them according to their signal. Before the brightest POI is chosen the signal of the pixel located between the two brightest ranked pixels is also considered. The overall brightest pixel in this comparison is used as the new POI and the rest is discarded.
The second iteration of the grouping and reduction processes as a whole provide a single POI per star for nominal cases. The remaining situations include saturated field stars and overlapping bright stars in image regions with high star density. Even though those scenarios are rare, they might occur once or twice per image. Therefore, the subsequent target identification algorithms are designed to be robust against small numbers of multiple detections per object.

2.1.7 Centre of Gravity Calculation

The final step of the Star Extraction routine uses the previously selected *pixels of interest* to determine star positions by calculating the *centres of gravity* (CoG) in a *region of interest* (ROI) around them.
Therefore, the CoG for the signal in a square region around the POI [x-2:x+2, y-2:y+2] is calculated on a subpixel scale. Before the calculated position can be converted back to full frame coordinates, the total signal in the ROI is checked against the *star detection threshold*

(SDT) for the full PSF. This is meant to prevent false positive detections of intense cosmic rays, as well as detections of stars below the desired magnitude on which the threshold was originally based. The latter is possible when the joint signals of overlapping faint stars or the combination of cosmic rays and faint stars satisfy the signal criteria to be considered a *pixels of interest*. Even though the results might be valid star positions, they must not be considered for the identification algorithm input data, as unexpected star detections can degrade the identification results. Finally, positions of all stars that pass the signal check are converted back to full resolution positions and are provided to subsequent functions as *observed positions*.

2.1.8 Visualisation

A step wise illustration that visualises the functionality of the *Star Extraction* process for a single star is provided in Fig.: 2-1. The steps describe the pictures from the top left to bottom right:

1. Starting with the full resolution image (top left), the image data are rebinned and scanned for POIs (top centre).
2. Two groups of POIs are formed due to the slightly extended signal distribution. One contains the yellow bottom left 3x3 pixels from $[62,62]$ to $[64,64]$ and the other the remaining blue pixels around the upper right corner from $[63,65]$ to the right to $[65,65]$ and down to $[65,63]$ (top centre).
3. The two groups are reduced to two POIs. Note that the average position of the blue group moved into the former area of the yellow group. This behaviour of the group reduction favours the convergence multiply detected objects to single positions. (top right)
4. After the second grouping and reduction process only one POI (red dot) remains at $[64,64]$. It is used to span the ROI (red square) for the centre of gravity calculation (bottom left).
5. The CoG on the rebinned frame is located at $[63.57,63.57]$ (bottom centre).
6. Transformation to full resolution coordinates gives $[512.55,512.54]$ (bottom right).

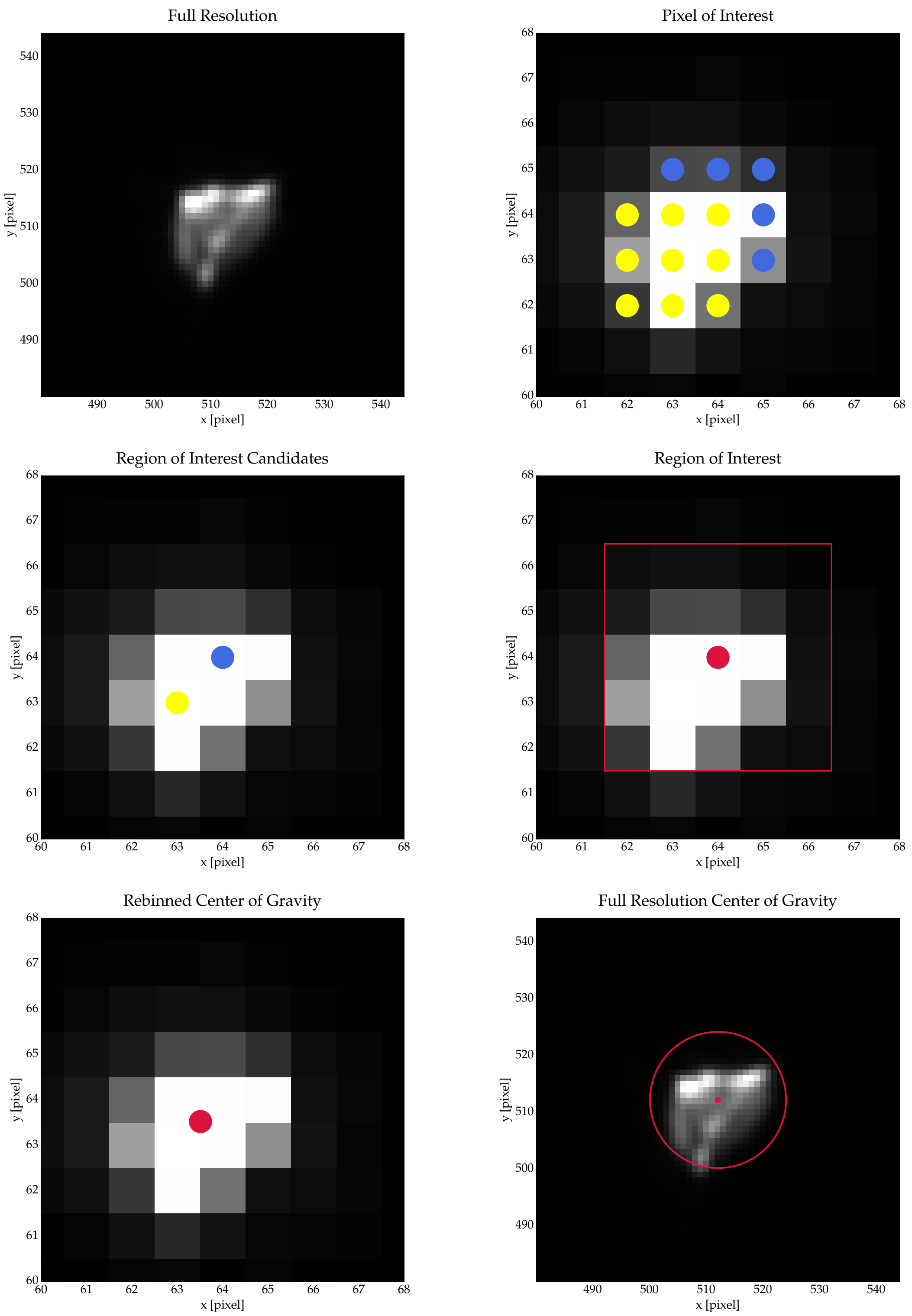

Figure 2-1: Step by step visualisation of the Star Extraction process.

2.2 Angle Method Algorithm

The *Angle Method Algorithm* (AMA) is a modified version of a technique that was originally suggested as a pattern recognition method for *lost-in-space* star tracker operation by Liebe [1992]. It is independent of photometric measurements and utilises the geometrical properties of the star distributions around the designated target star instead. More precisely, the angular distances between a potential target star and two of its neighbours are considered in combination with the spherical angle at their vertex. This triplet of information is considered to be a unique *fingerprint*, that can be matched with pre-calculated fingerprints in an observation specific *Reference Star Database*. Unlike Liebe's original algorithm, which is used to identify many stars in a given observation, only the identification of the target star is of interest in this case. Similar to Zhang et al. [2008], the fingerprints are only constructed for central stars, that qualify as potential targets. Like in original algorithm of Strikwerda & Junkins [1981], they are not only constructed from the closest neighbours but with all available extracted star positions. This has the advantage of several identifiable fingerprints per target. Thus, it opens the possibility to quantify the identification result and determine its validity. In combination with the known initial pointing within a worst case absolute pointing error (APE), it also enables the return to Strikwerda & Junkins' sub-catalogues for the Reference Star Database. Finally, and inspired by the *k-vectors* of Mortari [1996], all search operations are performed on a database index that constrains the stored locations of each fingerprint.

As one of two available identification methods, the Angle Method Algorithm is intended for acquisition procedures of non trivial identification cases, where the target star cannot easily be distinguished from other field stars by using the available photometric method. This will be the case for FOV with targets of 10 mag or fainter, where the chance for the presence of another star of similar brightness becomes a concern for misidentifications.

2.2.1 Star Database

The *Angle Method Algorithm* uses star positions to obtain the geometrical characteristics for an observation. On-board the satellite, they are determined by a dedicated *Star Extraction* routine for each image. The respective reference set of positions are taken from the GAIA star catalogue [Salgado et al., 2017]. These *reference positions*, along with other control parameters for the AMA are transmitted to the satellite with the *Star Map Command* (section 3.4) and have to be prepared by the science operations center (SOC) for every single observation. The process to create unique identifiers from those star catalogues is described below.

2.2.1.1 Fingerprint

All positions in the provided star catalogues are grouped with the target to form star triplets. The unique feature for the identification process is built from the relative distances between the target and the two other stars as well as the angle at the target vertex. The distances and vertex angle of such a triplet in their quantised form is what we call the *fingerprint*.

Each fingerprint consists of the combination of a *base star* and two of their neighbouring stars, which will be referred to as *first* and *second partner stars*. While the partner stars can be any detectable star in the FOV, the star that is to be identified by the algorithm is always chosen as the base star. A collection of such fingerprints forms the Reference Star Database. An example of such a fingerprint is presented in in Fig.: 2-2.

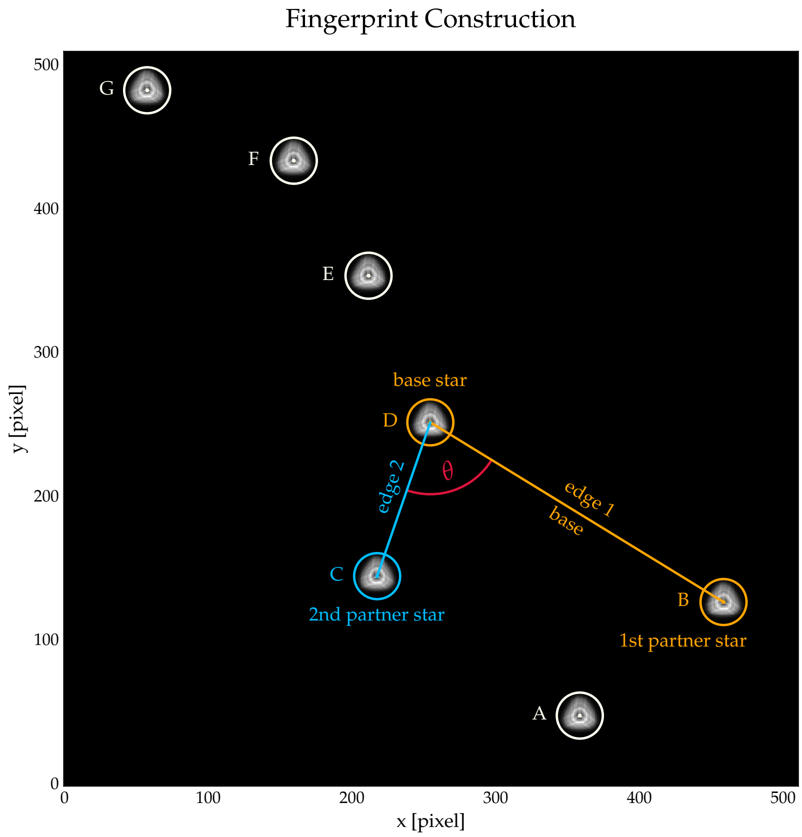

Figure 2-2: Visualisation of the fingerprint construction. Note that *edge 1* and *edge 2* are named *base 0* and *base 1* in the code as it predates a later change in nomenclature.

Fig.: 2-2 shows a FOV with $n = 7$ stars. They are marked from A to G in ascending order with respect to their Y, X-coordinates, which is the same sequence that the *Star Extraction* would produce. The target star (D) is in the center and marked as the base star (orange). Star B serves as the 1st partner star (orange) and star C as the second partner star (blue).

The distances between the base and the two partner stars B and D are measured in CCD pixels and the angle at the vertex of the base star (D) is measured in degrees. They are marked as *edge 1* (orange), *edge 2* (blue) and angle *theta* (red). Such a fingerprint will be described by the triplet ([DB], [DC], θ(DBC)), where [DB] marks the distance between stars D and B and Θ(DBC) refers to the angle at the vertex D. The detailed quantisation process will be explained for the creation of the *Observed Star Database* in section 2.2.1.3.

2.2.1.2 Reference Star Database

Identification with only a single *fingerprint* is prone to errors and may lead to misidentifications. Therefore, all possible fingerprints are formed for the edge that is represented by the base star (D) and its current first partner Star (B). This edge is also called the *base* ([DB]) of a *Fingerprint Set*. The set consists of all $(n-2)$ fingerprints that can be formed by combining the base with any available star as the Second Partner. The FOV in Fig.: 2-2 contains the following five fingerprints:

Set for Base DB
([DB], [DA], θ(DBA))
([DB], [DC], θ(DBC))
([DB], [DE], θ(DBE))
([DB], [DF], θ(DBF))
([DB], [DG], θ(DBG))

Table 2.1: Fingerprint Set for the Reference Star Database.

Although the full Fingerprint Set prevents the risk of misidentifications from single mismatched fingerprints, it does not address the problem of potentially missing stars in the star catalogue, that is used to produce the fingerprints. If the above set were provided to identify star D in an observation were star B is not present, none of the fingerprints would be detected. In order to conquer this problem, the sets for fingerprints of the remaining possible bases are also included to collectively form the *Reference Star Database* (RDB). Utilising all possible sets results in a total number of $(n-1)(n-2)$ fingerprints as can be seen in Tab.: 2.2.

Reference Star Selection The stars for a Reference Star Database are chosen such that the covered sky includes all possible orientations that could be observed by the spacecraft. The star positions are provided by the Gaia star catalogue and considered to be without error, since their milliarcseconds accuracy is magnitudes below the arcsecond accuracy of the *Star Extraction* [de Bruijne, 2012]. In order to prevent the detection of additional and unexpected stars, the Star Extraction parameters are configured to only find objects that were considered for the reference stars.

Set for Base DA	**Set for Base DB**	**Set for Base DC**
([DA], [DB], θ(DAB))	([DB], [DA], θ(DBA))	([DC], [DA], θ(DCA))
([DA], [DC], θ(DAC))	([DB], [DC], θ(DBC))	([DC], [DB], θ(DCB))
([DA], [DE], θ(DAE))	([DB], [DE], θ(DBE))	([DC], [DE], θ(DCE))
([DA], [DF], θ(DAF))	([DB], [DF], θ(DBF))	([DC], [DF], θ(DCF))
([DA], [DG], θ(DAG))	([DB], [DG], θ(DBG))	([DC], [DG], θ(DCG))

Set for Base DE	**Set for Base DF**	**Set for Base DG**
([DE], [DA], θ(DEA))	([DF], [DA], θ(DFA))	([DG], [DA], θ(DGA))
([DE], [DB], θ(DEB))	([DF], [DB], θ(DFB))	([DG], [DB], θ(DGB))
([DE], [DC], θ(DEC))	([DF], [DC], θ(DFC))	([DG], [DC], θ(DGC))
([DE], [DF], θ(DEF))	([DF], [DE], θ(DFE))	([DG], [DE], θ(DGE))
([DE], [DG], θ(DEG))	([DF], [DG], θ(DFG))	([DG], [DF], θ(DGF))

Table 2.2: Reference Star Database with Fingerprints for Fig.: 2-2

2.2.1.3 Observed Star Database

The counterpart to the *Reference Star Database* is the *Observed Star Database* (ODB), which is created from the *observed stars* that are provided by the *Star Extraction* process. While the basic principle of fingerprint creation is the same as described above, it comes with two major differences to the Reference Star Database:

- The target star position is not known and it can only be restricted to a subregion that is defined by the expected spacecraft pointing error. Therefore, every star in that area has to be considered as base star.
- Observed stars come with a positional error that is possibly high enough to affect the correct matching of the inter-star distances (edges) and angles.

This introduces two additional layers in comparison to the Reference Database Structure:

1. Reference Star Database
2. Sets of Fingerprints
3. Fingerprints

1. Observed Star Database
2. Sub-database for each Base Star
3. Sets of Fingerprints
4. Subsets of Fingerprints with Uncertainties
5. Fingerprints

Base Star Selection The *Observed Star Database* has to select the same *base star* as the *Reference Star Database* to achieve a positive matching result. Since the intended target star position on the image and the maximum pointing error of the spacecraft are known, this information can be utilised to reduce the full number of extracted star positions to a few potential *target candidates*. These candidates can then be used as base stars to create Sets of Fingerprints from combinations with the other observed stars (not only the candidates). Each candidate forms a database from its respective Sets of Fingerprints. These databases are considered to be the *sub-databases* that make up the whole *Observed Star Database* (see Fig.: 2-3).

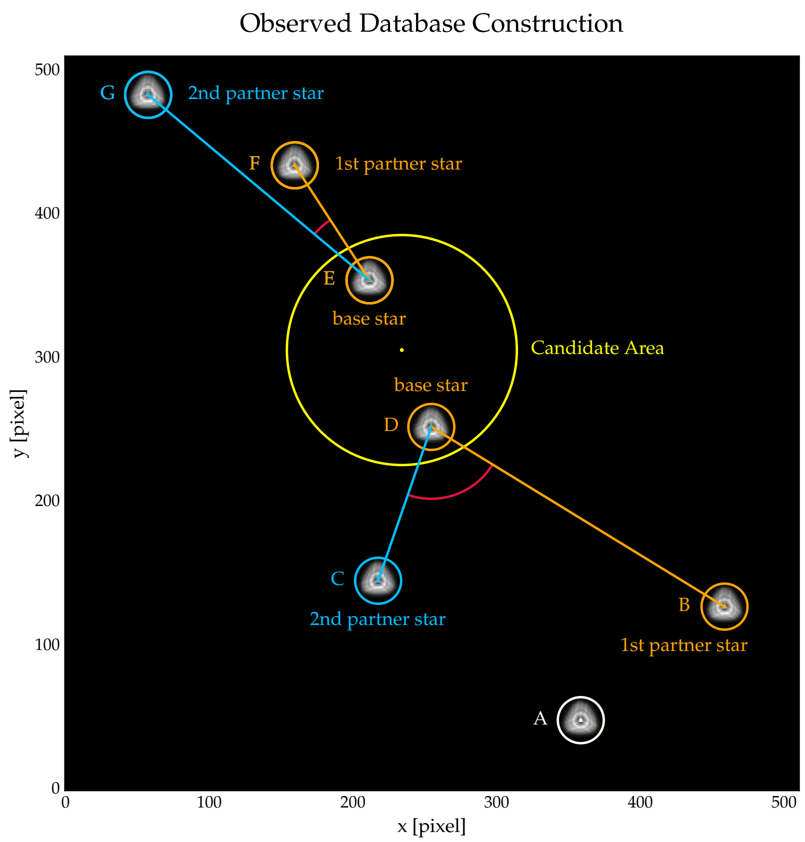

Figure 2-3: Visualisation of the fingerprint construction from target candidates for the Observed Star Database.

The intended *target location* (yellow dot) is at the center of the *candidate area* (yellow circle), which covers all possible offsets of the target star. Its radius is limited by the maximum pointing error and may vary for different observations. Any star within this area (in this case D and E) might be the desired target star, so each of them is used as base star. Like this, all possible Sets of Fingerprints are created through combinations with the remaining 6 stars.

Positional Uncertainties for Fingerprints The star positions provided by the *Star Extraction* can sometimes be inaccurate to about 1.5 px (see section 4.1.2). Since this error propagates into the calculation of the inter-star distances, it may introduce a variation of the expected star separations. In an attempt to compensate this behaviour, the edge lengths and the vertex angle are being quantised. The detailed quantisation process is described by the following example:

Consider a maximum separation error between two stars δr as $\pm$ 3 px (customisable). Therefore, the separation of 238.93 px of the stars D and B will be detected as 238.93 $\pm$ 3 px. Since all measures in the database are stored as integers, it opens the range of 7 possible values in [235, 241] for this edge alone. To account for the extreme compressed and stretched cases of 235 px and 241 px the quantisation is done with a factor of two δr:

$$\text{edge length r = [DB] = 238.93 px, } \delta\text{r = 3 px}$$

$$(r - \delta r)/2\delta r = 39.32 \tag{2.1}$$

$$(r)/2\delta r = 39.82 \tag{2.2}$$

$$(r + \delta r)/2\delta r = 40.32 \tag{2.3}$$

This transforms the edge [DB] to 39.82 ± 0.5 px and can be represented by the significantly shorter quantised interval of [39, 40].

The method comes with several advantages. While the maximum number of values for a particular edge is reduced by a factor of $x = (1 + 2 \cdot \delta r)/2$, the database size with two edges per fingerprint is affected by x^2. In addition, the theoretical upper limit for the database size is now independent of the position errors of a specific star pair. Therefore, it reduces the number of intervals for a quantised edge to two different possibilities. Lastly, the angle can also be affected, which is especially the case when the position errors of the two partner stars are oriented along the line of their (unused) edge. Since this depends on the specific orientation of a star triplet, the resulting error for the vertex angle can be highly variable within the fingerprints of a specific base. For this reason, there is no general maximum error that can be assumed for the angle quantisation as described for the edges. Instead, everything is quantised by a fixed interval of 5 degrees, which is chosen to be a trade-off between the angle accuracy and the resulting size of the database. Similar to the quantisation of the edges, this also leads to the allocation of a vertex angle interval of size two. Considering all uncertainties for both edges and the vertex angle gives a maximum of up to *eight* variations for a single *fingerprint*. Together they form the *Fingerprint Subset* for each star triplet in the observed case. Therefore, each fingerprint in the *Reference Star Database* is described by this *Fingerprint Subset* in the *Observed Star Database*. The variations are indicated by the subscripts 1 and 2 for the two possible quantised classes of each feature. By convention single *fingerprints* are described by round brackets () and *Subsets of Fingerprints* by curly brackets {}. An example for a set with the maximum number of fingerprints can be seen in Tab.: 2.3.

Subset {[DB], [DC], θ(DBC)}
(DB_1, DC_1, $\theta(DBC)_1$)
(DB_1, DC_2, $\theta(DBC)_1$)
(DB_1, DC_1, $\theta(DBC)_2$)
(DB_1, DC_2, $\theta(DBC)_2$)
(DB_2, DC_1, $\theta(DBC)_1$)
(DB_2, DC_2, $\theta(DBC)_1$)
(DB_2, DC_1, $\theta(DBC)_2$)
(DB_2, DC_2, $\theta(DBC)_2$)

Table 2.3: Fingerprint Subset with additional entries that cover the uncertainties for the Observed Star Database.

Database Index While the *Reference Star Database* is strictly ordered and has a total number of fingerprints given by $(n-1)(n-2)$ (n is the number of stars), the *Observed Star Database* is more complex. Here, the variable size of the *Fingerprint Subsets* prevents an order based navigation, and an index system for the database navigation becomes a necessity. In this system a *base index* and *value index* are used to store the *address* and the *quantised value* of the first entry for each *Fingerprint Set*. Besides the ability for database navigation, these indices also enable faster search operations during the matching process, which is described in section 2.2.2.

Database Size An a priori calculation of the exact database size is not possible since the number of angle classes per *Fingerprint Subset* and the number of *target candidates* can vary for different orientations of a specific FOV. However, with n_c being the number of target candidates and n the number of stars in the FOV, the maximum database size can be estimated:

$$max = n_c \cdot (n-1) \cdot (n-2) \cdot 8 \tag{2.4}$$

$$min = n_c \cdot (n-1) \cdot (n-2) \cdot 4 \tag{2.5}$$

Here, 4 and 8 mark the minimal and maximal number of *fingerprints per subset* and n_c is limited to 10 target candidates for the on-board software. With $n = 7$ and $n_c = 2$ for the example case in Fig.: 2-3 the full *Observed Star Database* has a theoretical maximum of *480 fingerprints*. Tab.: 2.4 shows this database.

Sub-Database for base star D

Set for Base DA	Set for Base DB	Set for Base DC
{[DA], [DB], θ(DAB)}	{[DB], [DA], θ(DBA)}	{[DC], [DA], θ(DCA)}
{[DA], [DC], θ(DAC)}	{[DB], [DC], θ(DBC)}	{[DC], [DB], θ(DCB)}
{[DA], [DE], θ(DAE)}	{[DB], [DE], θ(DBE)}	{[DC], [DE], θ(DCE)}
{[DA], [DF], θ(DAF)}	{[DB], [DF], θ(DBF)}	{[DC], [DF], θ(DCF)}
{[DA], [DG], θ(DAG)}	{[DB], [DG], θ(DBG)}	{[DC], [DG], θ(DCG)}

Set for Base DE	Set for Base DF	Set for Base DG
{[DE], [DA], θ(DEA)}	{[DF], [DA], θ(DFA)}	{[DG], [DA], θ(DGA)}
{[DE], [DB], θ(DEB)}	{[DF], [DB], θ(DFB)}	{[DG], [DB], θ(DGB)}
{[DE], [DC], θ(DEC)}	{[DF], [DC], θ(DFC)}	{[DG], [DC], θ(DGC)}
{[DE], [DF], θ(DEF)}	{[DF], [DE], θ(DFE)}	{[DG], [DE], θ(DGE)}
{[DE], [DG], θ(DEG)}	{[DF], [DG], θ(DFG)}	{[DG], [DF], θ(DGF)}

Sub-Database for base star E

Set for Base EA	Set for Base EB	Set for Base EC
{[EA], [EB], θ(EAB)}	{[EB], [EA], θ(EBA)}	{[EC], [EA], θ(ECA)}
{[EA], [EC], θ(EAC)}	{[EB], [EC], θ(EBC)}	{[EC], [EB], θ(ECB)}
{[EA], [ED], θ(EAD)}	{[EB], [ED], θ(EBD)}	{[EC], [ED], θ(ECD)}
{[EA], [EF], θ(EAF)}	{[EB], [EF], θ(EBF)}	{[EC], [EF], θ(ECF)}
{[EA], [EG], θ(EAG)}	{[EB], [EG], θ(EBG)}	{[EC], [EG], θ(ECG)}

Set for Base ED	Set for Base EF	Set for Base EG
{[ED], [EA], θ(EDA)}	{[EF], [EA], θ(EFA)}	{[EG], [EA], θ(EGA)}
{[ED], [EB], θ(EDB)}	{[EF], [EB], θ(EFB)}	{[EG], [EB], θ(EGB)}
{[ED], [EC], θ(EDC)}	{[EF], [EC], θ(EFC)}	{[EG], [EC], θ(EGC)}
{[ED], [EF], θ(EDF)}	{[EF], [ED], θ(EFD)}	{[EG], [ED], θ(EGD)}
{[ED], [EG], θ(EDG)}	{[EF], [EG], θ(EFG)}	{[EG], [EF], θ(EGF)}

Table 2.4: Observed Star Database with fingerprints for Fig.: 2-3

As mentioned before, each *Sub-database* is made from *Sets and Subsets of Fingerprints* for the different *target candidates*. The matching process will mostly recognise fingerprints in the Sub-database for target candidate D, which can then be identified as the target star.

2.2.2 Matching Process

With both databases in place, the next and most important step for the target identification is the matching process. Here, every *Fingerprint Set* in the *Observed Star Database* will be assigned to a matching *Fingerprint Set* in the *Reference Star Database*. The process itself consists of the initial *Fingerprint matching*, a subsequent *elimination of ambiguous matching results* and eventually a decision whether the target can be clearly identified.

2.2.2.1 Database Matching

For the matching process the algorithm iterates over every *fingerprint* in each *Fingerprint Set* in the *Reference Star Database*. To avoid repeated full scans of the *Observed Star Database* the address for each fingerprint is derived from matches within the *value* and *base index*. The index supported search drastically reduces the runtime for the matching process at the expense of increased memory usage for the search index. Let us assume a matching attempt for the *reference fingerprint ([DA], [DB], θ(DAB))* with its corresponding entry in the *Observed Star Database* of the sample observation:

First the quantised value of the edge [DA] is searched in the value index. In the above example it can be found in the Observed Sub-database with index 0 in the Set for the base [DA], which also has index 0. These match results are used to limit the search to a sub-sample of the whole Observed Star Database, which reduces the potentially interesting part of the database from originally 480 to only 40 fingerprints. This sub-sample is then used for the scan for the second edge [DB], which is again found at index 0 within the Fingerprint Set for base DA. Utilising this to further reduce the potentially interesting part of the database limits the search sample for the quantised angle to the maximum of 8 fingerprints for the Subset with the edge combination [DA], [DB]. Eventually the reference fingerprint is found at index 2 of the Subset in question. The whole tracking record with all of the above mentioned indices is stored as (0, 0, 0, 2) and is used for the exclusion of false matches at a later stage. This tracking is done for each matched fingerprint and the results can be seen in Tab.: 2.5.

Since the Reference and Observed Star Databases were constructed from the same observation and have the same order of stars, the indices in Tab.: 2.5 can easily be translated to a readable format. Therefore (0, 0, 0, 2) becomes (D, A, B, 2). This indicates that the reference fingerprint was matched with the observed fingerprint that is stored in the Observed Sub-database for *base star D*, build the first edge with *partner star A*, the second edge with *partner star B* and was stored with the *subset index 2*. The translated match result is shown in Tab.: 2.6.

Match results for Fingerprint Sets with base star D

Base DA	Base DB	Base DC	Base DE	Base DF	Base DG
(0, 0, 0, 2)	(0, 1, 0, 1)	(0, 2, 0, 3)	(0, 3, 0, 7)	(0, 4, 0, 3)	(0, 5, 0, 1)
(0, 0, 1, 5)	(0, 1, 1, 0)	(0, 2, 1, 0)	(0, 3, 1, 2)	(0, 4, 1, 2)	(0, 5, 1, 0)
(0, 0, 2, 7)	(0, 1, 2, 1)	(0, 2, 2, 2)	(0, 2, 2, 2)	(0, 4, 2, 2)	(0, 5, 2, 0)
(0, 0, 3, 3)	(0, 1, 3, 1)	(0, 3, 2, 4)	(0, 3, 2, 4)	(0, 4, 3, 7)	(0, 5, 3, 2)
(0, 0, 4, 2)	(0, 1, 4, 0)	(0, 2, 3, 1)	(0, 3, 3, 7)	(0, 4, 4, 2)	(0, 5, 4, 1)
		(0, 2, 4, 0)	(0, 3, 4, 4)		

Table 2.5: Raw initial results for matches with base star D.

Match results for Fingerprint Sets with base star D

Base DA	Base DB	Base DC	Base DE	Base DF	Base DG
(D, A, B, 2)	(D, B, A, 1)	(D, C, A, 3)	(D, E, A, 7)	(D, F, A, 3)	(D, G, A, 1)
(D, A, C, 5)	(D, B, C, 0)	(D, C, B, 0)	(D, E, B, 2)	(D, F, B, 2)	(D, G, B, 0)
(D, A, E, 7)	(D, B, E, 1)	(D, C, E, 2)	(D, C, E, 2)	(D, F, C, 2)	(D, G, C, 0)
(D, A, F, 3)	(D, B, F, 1)	(D, E, C, 4)	(D, E, C, 4)	(D, F, E, 7)	(D, G, E, 2)
(D, A, G, 2)	(D, B, G, 0)	(D, C, F, 1)	(D, E, F, 7)	(D, F, G, 2)	(D, G, F, 1)
		(D, C, G, 0)	(D, E, G, 4)		

Table 2.6: Translated initial results for matches with base star D.

The maximum number of *matches per base* for this case is $(n-2) = 5$. While this is true for the majority of matched bases, base DC and DE contain an additional false positive entry that is a result of the isosceles triangle of the stars D, C and E. Stars in such orientations cannot be distinguished by the *Angle Method Algorithm* and will introduce false matches. For this reason, the match results are corrected from ambiguous matches in a subsequent step. To ensure that enough matches are left after this correction, ideally five or more stars should be available in observations that use the Angle Method Algorithm for target identification. This increases the number of available fingerprints per base and therefore compensates for deleted matches in problematic cases.

2.2.2.2 Match Result Corrections

Base Specific Correction The first out of three correction steps analyses the matched *observed fingerprints* for each *reference base* separately. Here, all matched fingerprints have to be from the same observed base (same base star and first partner) to be considered valid. Therefore, the so called *star tracker* compares the *base star* amongst all matched fingerprints and discards diverging fingerprints that match with a different base than the majority. In addition, it also stores the matched Observed base star for each reference base. The same is done with the *base tracker* for the partner star. The match record for reference base DC in Tab.: 2.6 is an example for this. While five of the matched fingerprints are formed with C as the first partner star, there is a single fingerprint with partner star E. Since the majority was matched to *observed base* DC, the match for the base DE seems out of place and is considered to be wrong. The contrary is true for the match record of *reference base* DE. In both cases the wrong match is discarded and not considered for the later determination of the *match result quality*. The preliminary number of valid matches for a reference base can be determined by the count of fingerprints made from unique second partner stars. This number is stored for each reference base in the so called *match results histogram* and can be altered by the remaining correction steps. The match results histogram for the example is shown in Tab.: 2.7:

Match Results Histogram

Reference Base	DA	DB	DC	DE	DF	DG
No. of Matches	5	5	5	5	5	5

Table 2.7: Histogram to track the frequency of matches for each reference base.

Here, it also represents the final match result since no further corrections are necessary for this example. Therefore, 100% of the fingerprints in the Observed Star Database could be matched. Further evaluation of this result is discussed in section 2.2.2.3 on the validation metric. Generally, observations might not match that well and are therefore treated with additional corrections steps as described in the following subsections.

Cross Base Correction Although each *observed base* and its *Fingerprint Set* should only match a single *reference base*, some fingerprint variations might match with the wrong reference base as described above. While most of these matches should already be eliminated by the previous correction step, it sometimes happens that fingerprints from one observed base are assigned to multiple reference bases. This behaviour can be observed in very crowded fields with short inter-star distances. In such situations, the distances are prone to be mapped to similar quantised classes that can further match with multiple observed Fingerprint Subsets. The other case for such false positives are matches with reference bases, which are formed from stars that were below the detection threshold or not visible in the current FOV orientation. Such bases might accidentally match 1-2 fingerprint variations but are not corrected by the previous step, due to the lack of real matches.

The *star* and *base tracker* are used to identify *observed bases* that were matched to multiple *reference bases*. In such a case, the reference base that holds identified fingerprints is considered to be the valid match. The respective number of matched fingerprints can be retrieved from the *match results histogram*. The process then discards all matches of the invalid base(s). In addition, all fingerprints that were matched with the valid and invalid reference bases are considered to be ambiguous and are also discarded from the valid reference base. All changes are also reflected in the match results histogram.

Since this particular matching failure is rather rare and not present in the above example, let us consider a hypothetical additional reference star *H* (Fig.: 2-4). Here, *H* is provided as a margin against interlopers (section 3.1.3) that should not be detected under nominal conditions. In this example it is not be detected in the observation, but is located such that it produces the following incorrect match result:

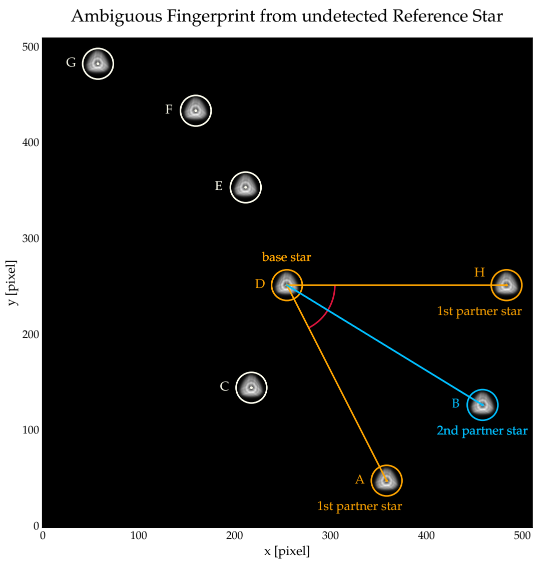

Figure 2-4: Construction of an ambiguous fingerprint from the identical triangles $\Delta(DAB)$ and $\Delta(DHB)$.

Cross Base Validation for base star D

Base DA	Base DH
(D, A, B, 2)	(D, A, B, 1)
(D, A, C, 5)	
(D, A, E, 7)	
(D, A, F, 3)	
(D, A, G, 2)	

Table 2.8: Example for the Cross Base Correction of an ambiguously matched result.

The algorithm would identify base DA and DH to be matched with fingerprints from the same observed base. Since there are more matches for DA, base DH would be discarded as the invalid match. Even though the fingerprint *([DA],[DB], θ(DBA))* was matched for a different variation, it is still considered ambiguous and therefore discarded. As a consequence, this operation would reduce the number of valid matches for base DA to four.

Base Star Correction After the previous correction steps across the reference base matches, the valid base star can be determined. Since the best matching base star and first partner star were determined separately for each reference base, it is possible that the different reference bases were matched to fingerprints of different base stars. As there can only be one valid base star, all matches with the less frequently matched base star are discarded from the match results histogram. Similar to the correction step before, this is a rather rare issue and more common in tighter packed star distributions. Consequently, it did not occur in the example and is shown by the hypothetical match result in Tab.: 2.9.

Hypothetical Match Results for Fingerprint Sets with base star D

Base DA	Base DB	Base DC	Base DE	Base DF	Base DG
(E, A, B, 2)	(D, B, A, 1)	(D, C, A, 3)	(D, E, A, 7)	(D, F, A, 3)	(D, G, A, 1)
(E, A, C, 5)	(D, B, C, 0)	(D, C, B, 0)	(D, E, B, 2)	(D, F, B, 2)	(D, G, B, 0)
(E, A, D, 7)	(D, B, E, 1)	(D, C, E, 2)	(D, E, C, 4)	(D, F, C, 2)	(D, G, C, 0)
(E, A, F, 3)	(D, B, F, 1)	(D, C, F, 1)	(D, E, F, 7)	(D, F, E, 7)	(D, G, E, 2)
(E, A, G, 2)	(D, B, G, 0)	(D, C, G, 0)	(D, E, G, 4)	(D, F, G, 2)	(D, G, F, 1)

Table 2.9: Example for the Base Star Correction of ambiguously matched results.

Here, only reference base DA would be matched with the base star E, while the remaining 5 reference bases clearly fit the fingerprints of star D. Therefore, D is selected as the most likely target star and all matches with base star E are discarded from the match results.

Statistical Correction Even though a solution for the target star has been suggested at this point, a last step is taken to clean the match results histogram from problematic matches. First, the remaining accidental matches with unused reference bases are discarded (similar to the case in Cross Base Corrections in section 2.2.2.2). The same is true for the sparse leftovers of corrected bases that have significantly less matches than the well matched references bases. The latter is done by calculation of the average number of matched fingerprints per reference base. Together with the respective standard deviation σ, a minimum number of matches m is defined by

$$m_{min} = m_{avg} - 2 \cdot \sigma \tag{2.6}$$

All results from reference bases with less than the minimum amount of matched fingerprints are removed from the match results histogram. This final step marks the completion of the match results correction. All remaining matches are considered to be valid and can be used to determine whether the selected target candidate was matched well enough in order to be clearly identified as the target star.

2.2.2.3 Match Result Validation

The selected target candidate cannot directly be considered as the identified target star for various reasons. Besides the obvious case where the actual target star is not present and a few accidental matches would trigger a misidentification, the specific way how the database matching process was implemented for cases with multiple target candidates is another one. Whenever a fingerprint can be identified within one of the observed sub-databases, the search is not continued to check if it also exists in the remaining sub-databases. This was done for two reasons. It is quite unlikely to encounter the same fingerprint in another sub-database, due to the random nature of star distributions and the way the fingerprint geometry works. Therefore, continuing the search is mostly a waste of computational resources. Overall, the reduced matching times to meet the stricter initial runtime requirements were more favourable. Even though the abortion of the search optimised the execution time and memory usage, it can theoretically lead to an extreme match result like in Tab.: 2.10 on very rare occasions.

Hypothetical Match Results for Fingerprint Sets with base star D

Base DA	Base DB	Base DC	Base DE	Base DF	Base DG
(E, A, B, 2)	(D, B, A, 1)	(D, C, A, 3)			
(E, A, C, 5)	(D, B, C, 0)	(D, C, B, 0)			
(E, A, D, 7)	(D, B, E, 1)	(D, C, E, 2)			
(E, A, F, 3)	(E, B, F, 1)	(E, C, F, 1)			
(E, A, G, 2)	(E, B, G, 0)	(E, C, G, 0)			

Table 2.10: Example of a difficult result for the Match Result Validation.

The algorithm would decide that base star D is dominant in two thirds of the matched reference bases and suggest that base star D is the valid target candidate. Upon closer inspection one can see that star E actually has one more match than star D and generally less than half of the total possible matches were achieved. Considering that base star E can only be matched if there is no prior match with star D in the first sub-database, it could be that E would have matched all of the reference bases DA, DB, DC. Although this is an inherently problematic behaviour of the Angle Method Algorithm, it hardly has any significance for real observational cases. A star distribution to trigger such a case would have glitch degraded star positions and has to be highly symmetric along an axis that separates the two target candidates. One could argue that every matched fingerprint might have matched another one in the next sub-database, but star distributions that fulfil such a level of symmetry are very unlikely. Similar to the isosceles case, it would just be unsolvable and should be solved with photometric means. In an attempt to also avoid these rare cases and to keep such poorly and maybe ambiguously matched orientations from triggering positive target identifications, it was decided that the total number of matched fingerprints in the match results histogram has to be higher than a certain threshold.

Validation Metric The *primary success criterion* that has to be met for a positive identification is defined by the maximum number of fingerprints that is possible for the number of *observed stars n*. Out of the $(n-1)(n-2)$ possible combinations, at least 50% must be matched for a target candidate to be recognised as the target star. In order to match such large fractions of the Observed Star Database, it is required that every observed star is represented by the set of reference stars. For this reason, the thresholds for the *Star Extraction* are configured such that all thereby detected observed stars are brighter than the faintest Reference Star.

This primary criterion is meant to guarantee that the algorithm selects the best possible target candidate. While some reference fingerprints might be wrongly assigned to another Candidate's database, the extreme examples presented in the previous section are exceptions that usually do not occur. This in turn means that the vast majority of fingerprints are unique to their sub-database, which makes it impossible for two competing target candidates to achieve results above 50% at the same time. Therefore, such a result can safely be considered as the successfully identified target star.

This requirement will easily be met for the majority of generally identifiable orientations. An exception are sparsely populated FOV with one or more interloping stars, that are not covered by the reference. In such cases, additional stars have a larger effect on the match quality than it would be the case for observations with plenty of stars. A more detailed description of their effects can be found in section 2.2.2.3. While the match results of such observations can be degraded to the point where the validity criterion cannot be met, they are not necessarily wrong. To save such an otherwise perfectly fine result, a secondary criterion for the validity is used. For this, the maximum possible number of matched fingerprints $n_{fp_{max}}$ is calculated from the number of matched reference bases n_b

$$n_{fp_{max}} = n_b \cdot (n_b - 1) \tag{2.7}$$

Though a less conservative measure, this approach has the advantage, that it is not directly affected by interlopers. Together with the total amount of possible matched reference bases, which is one less than the number of observed stars, this secondary criterion is used to identify the targets that failed the primary one. In this case a valid identification needs matched fingerprints in at least 50% of the possible reference bases. In addition, it is required that for all of these bases more than 65% of $n_{fp_{max}}$ fingerprints are successfully identified. This results in a minimum matching threshold between 32.5% and 50% of the Observed Star Database. If this less stringent criterion also cannot be met as well, a final safety layer in the form of a *tertiary success criterion* can enable a successful identification. Even though the match result will be returned as failed at this point, the *Angle Method Acquisition* can be used in combination with the *Magnitude Validation Algorithm*. Thereby, insufficient match results can be saved with a subsequent photometric analysis of the target candidate signal. Although the combination of both methods is a potentially robust way for the identification problem, the photometric verification should not be used on exceptionally bad Angle Method Acquisition results. As described in section 2.3, the photometric accuracy is rather limited. Since the Angle Method Acquisition is designed for faint targets, the other target candidate may lie within the signal tolerance of the Magnitude Validation Algorithm. For this reason, a photometric misidentification could verify a poor and potentially wrong Angle Method result, which in turn would lead to a misidentified target star. To prevent such false positives, the Angle Method match result must satisfy the primary criterion with a relaxed 40% threshold to allow a photometric validation. The main difference to the *secondary criterion* is the lack of the additional base specific requirements. This makes it applicable to generally poor identification results and still is accurate enough to be considered as an indicator for a successful identification. In general, the calculated offsets from successful identifications are reported to the AOCS via the *centroid report service* of the IFSW [Reimers et al., 2016].

Effects of Interloping or Missing Observed Stars Additional and missing stars affect the result in different ways. While a missing star only increases the negative impact of fingerprints that cannot be assigned to a reference base, an interloper introduces several fingerprints which do not exist in the reference. Depending on the number of observed stars, this leads to corruption of big parts of the Observed Star Database and therefore prevents successful identification. The effects of one and two interlopers are shown in Fig.: 2-5 and 2-6. The first shows how a single interloper affects the fingerprints in the Observed Star Data-base. The red line describes the total number of fingerprints and the blue line describes the number of unaffected fingerprints that are still valid. In addition, their respective fractions of the Observed Star Databases are indicated by the red and blue filled areas. The effect is especially profound for observations with a low amount of observed stars. An interloper in an observation with as little as 5 stars results in an Observed Star Database with 50% corrupted fingerprints, that will not be able to match the Reference Star Database. Therefore, such an observation is almost unsolvable by the above defined success criteria for a positive target identification. Fortunately, the impact of interlopers diminishes with a growing number of observed stars and it settles between 10-15% for the targeted optimal star counts.

Introducing a second interloper has more devastating effects and prevents detections with the *primary criterion* until up to 8 observed stars (Fig.: 2-6). Even at higher star counts,

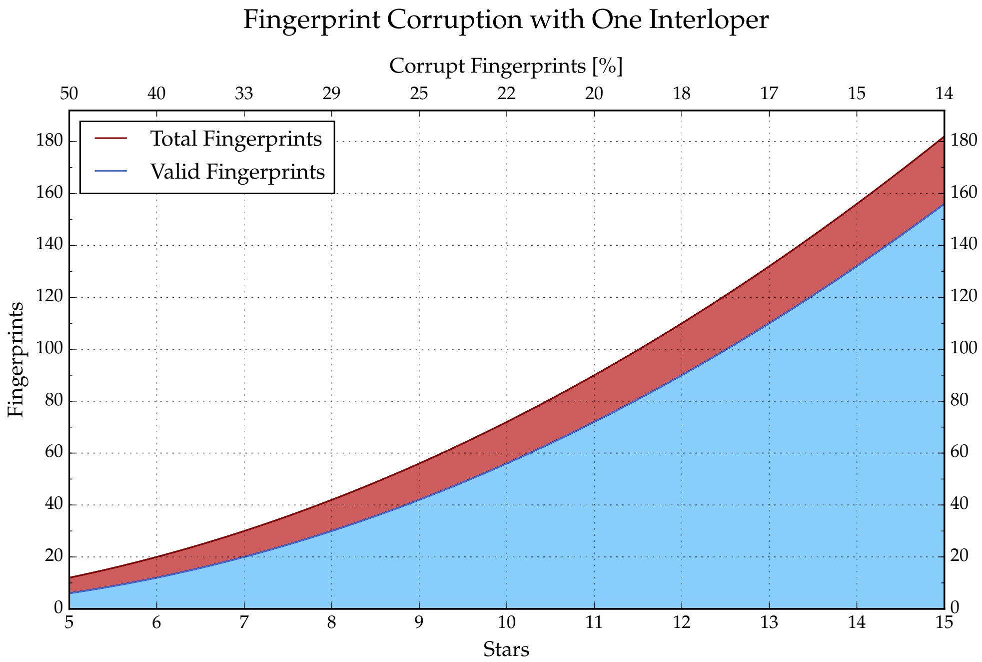

Figure 2-5: Effects of single interloping stars on the Observed Star Database.

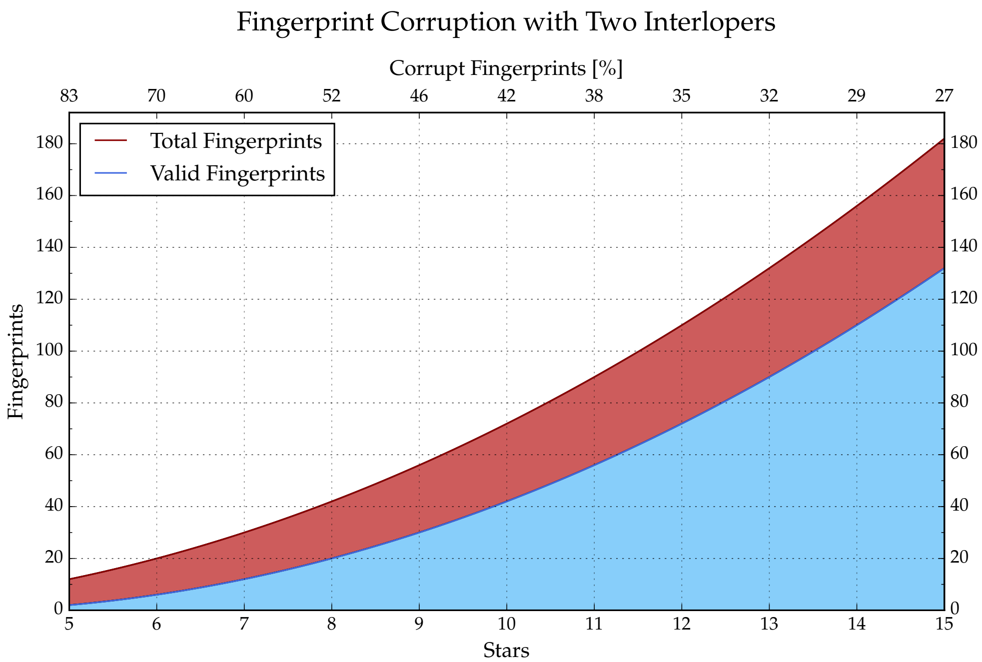

Figure 2-6: Effects of two interloping stars on the Observed Star Database.

the corrupted fraction of fingerprints is still between 25-30% and thus requires very good matching results with the remaining stars. For this reason, the *Star Extraction* thresholds should be configured such that they provide 10 or more observed stars for the *Angle Method Acquisition*. Generally, interloping stars can originate from

- detections of overlapping faint stars
- detections of faint stars due to overlapping cosmics
- detections of extremely bright cosmics
- planets and asteroids

Here, faint stars are stars that were intended to stay undetected. They are usually encountered in crowded fields that favour such overlaps. Misdetections caused by cosmics are usually only encountered during SAA transits. Even though the chances that they affect detections in sparsely populated FOV are low, the calculation of the *detection thresholds* for the Star Extraction is focused on the prevention of such glitch induced detections. Depending on the available reference stars for an observation, detection thresholds are usually configured such that cosmic rays are not expected to interfere with the identification until up to 150 times their nominal rate (see section 3.1.4). Together with the careful selection of reference stars, interlopers are generally avoided and they should only pose a problem in extreme SAA environments and poorly configured acquisitions.

Target Selection Once the target star is identified, its position on the CCD can be used to calculate the offset to the originally intended *target location*. This offset is then reported to the attitude and orbital control system with by the Instrument Flight Software (IFSW).

Identification Failure Simulations have shown that identification failures should be the exception (see chapter 4). Their most common reasons are:

- bad reference positions
- target location changes
- pre-emptive Target Acquisition during slew manoeuvres (smeared images)
- wrong input parameters (eg. wrong target location)

whereas the first three are recoverable by repeated observation. The remainder is usually caused by exceptionally heavy glitch rates or unlucky glitch positions that can result in *offsets for the observed stars*. This affects the *edge lengths* of fingerprints, which then cannot be matched with the Reference Star Database. Repeated observation changes the FOV orientation, glitch positions and possibly also the rate. Therefore, a successive observation under different conditions is the best recovery from identification failure. The number of additional iterations to recover from failures is part of the input parameters that are provided with the *Star Map Command* (see section 3.4). The second recoverable occurrence is during *target location* changes. In the case of the CHEOPS AOCS, a new target is always placed at the CCD position of the previous observation. If it changes between two observations, the target will be placed at the old position but the target candidates are searched in the new *candidate area* for the first new observation. For this reason, the actual target will not be part of the target candidates and the attempt fails. Since the AOCS will place the target star in the correct location for the next attempt, any successive target acquisition iterations should be successful. The same is true for pre-emptive acquisition attempts. Sometimes the acquisition is already started while the target star might still be on the way to its designated target location. As a result, it is either smeared or just not in the right place. Repeated attempts will lead to acquisition success once the slewing manoeuvre is finished.

Critical misidentifications are usually only caused by faulty algorithm configuration. This should be prevented by the mostly automated parameter setup and the ability to simulate the Target Acquisition with the *Star Map Generator Tool* (see chapter 3). Therefore, such cases usually originate from wrong input data or random operator failure. If the acquisition cannot be resolved, the failure is documented and the science operation will be attempted with the latest attitude.

2.3 Magnitude Validation Algorithms

The *Magnitude Validation Algorithm (MVA)* is an identification method that utilises photometry to compare the measured signal of the target candidates to a reference signal that is provided for each observation. Initially, it was only intended to be used as a secondary layer of verification for weak Angle Method Acquisition results, but was later upgraded to the *Magnitude Validation Acquisition Algorithm (MVAA)*. This is designed to serve as the main identification method for sparsely populated FOV, where the lack of a similarly bright target candidate trivialises the identification. It is also used for observations where very luminous targets prohibit exposure times that would be necessary to image a sufficient number of stars for the Angle Method Acquisition.

2.3.1 Magnitude Validation Algorithm (MVA)

This variant is used to confirm weak Angle Method Acquisition results as stated above and hence can only be run in its succession. The MVA requires the *observed position* of the best AMA target candidate, along with an expected *reference target signal* [ADU], the respective *signal tolerance* [%] and an estimate for the *background signal* for its operation. The target candidate in question will be confirmed if the result of the radius photometry is within in the provided tolerance. Otherwise the acquisition attempt is still considered a failure.

2.3.2 Magnitude Validation Acquisition Algorithm (MVAA)

The standalone acquisition variant is slightly more complex, as it also has to perform the target candidate selection from *observed stars*. Comparable to the target candidate selection in the Angle Method Acquisition, available star positions are only considered if they are within the *candidate area* around the *target location* (Fig.: 2-3). A radius photometry algorithm is then used on each of these target candidates to determine the closest match with the *reference target signal*. While ideally only one target candidate matches the reference target signal, there are exceptions that can lead to identification failures. These include:

- multiple target candidates of similar signal within the tolerance
- target candidates with stacked signal from overlapping stars
- signal saturation
- corrupt candidate positions with multiple detections of single objects

The first three cases are unsolvable since they will lead to either ambiguous or completely wrong photometric results. Fortunately, they should usually be avoidable by proper algorithm parameter configuration. Therefore, they will be identified by the ground segment before the observation. The last issue about faulty star positions is expected to occasionally happen with relatively bright objects close to saturation. For this reason, safeguards that are meant to recover failed identifications in such cases are in place. If up to five target candidates match the Target Reference Signal, they are not immediately discarded as multiple ambiguous matches but rather analysed whether they might describe the same object. Cases where the distances are all within the PSF diameter of 24 pixel and the measured signals do not vary more than three percent, are considered to be a multiple detection of a single object. The three percent threshold is chosen well below the signal tolerance, so it only addresses the signal variation that comes with the slight change in position. Therefore, it fails for larger changes where the signal was, for instance, corrupted by the influence of a close neighbour. Another reason for failure is when part of the positions in question are actually from a neighbouring star with a signal within the tolerance. The combination of these geometric and photometric criteria ensure that separate candidates are not accidentally considered as the same object. If they are met, the target candidate with the best signal match is considered to be the most central on the PSF and will be chosen as the identified target. Similar to the result of the Angle Method Algorithm, the outcome of the identification attempt is reported to the AOCS via the centroid report service of the IFSW.

2.3.3 Radius Photometry

The *radius photometry* determines the star signal on the full frame image within a radius of 25 pixel around a provided star position. This radius is expected to contain 98.45 % of the signal within the defocused PSF, which is considered in the calculation of the *reference target signal*. Every pixel in the thereby covered area is corrected from the effects of the background signal (see section 2.3.3.2) and integrated over all pixels to obtain the isolated star signal in ADU.

2.3.3.1 Point Spread Function Shape

The defocused wide shape of the PSF is a trade-off between a large surface that favours the reduction of jitter noise and a small surface to decrease the susceptibility to stray light contamination (SciReq 1.3 Tab.: 1.1). While other factors like cosmic rays and different noise sources also played a role, these two were its main design drivers [Benz et al., 2013] . A simulation of the expected signal distribution for the CHEOPS PSF is presented in Fig.: 2-7. The comparison with the real PSF, as measured with the optical system in Fig.: 2-8 shows strong deviations from the original design. Even though the full signal was contained in a rather compact spherical triangle in the simulation, the real optical system features stronger diffractive effects. These result in a non-symmetric PSF with a less homogeneous signal distribution that extends beyond the anticipated diameter of 24 px. Fortunately, the majority of the signal is within the 25 px radius used for photometry.

Due to the strong focus onto the central pixels, only a small fraction of about 1.5 % of the signal is lost by this. Solving this problem with an extension of the photometry radius would lead to a problematic influence by the signal of close-by stars. Therefore, it is treated like a systematic difference in the calculation of the *reference target signal*.

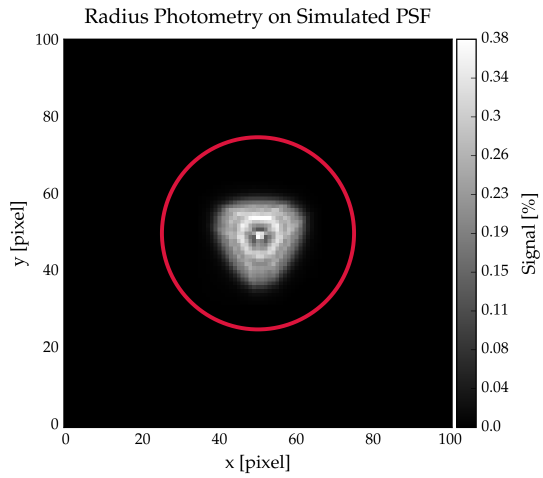

Figure 2-7: Simulated shape and signal distribution of the CHEOPS PSF.

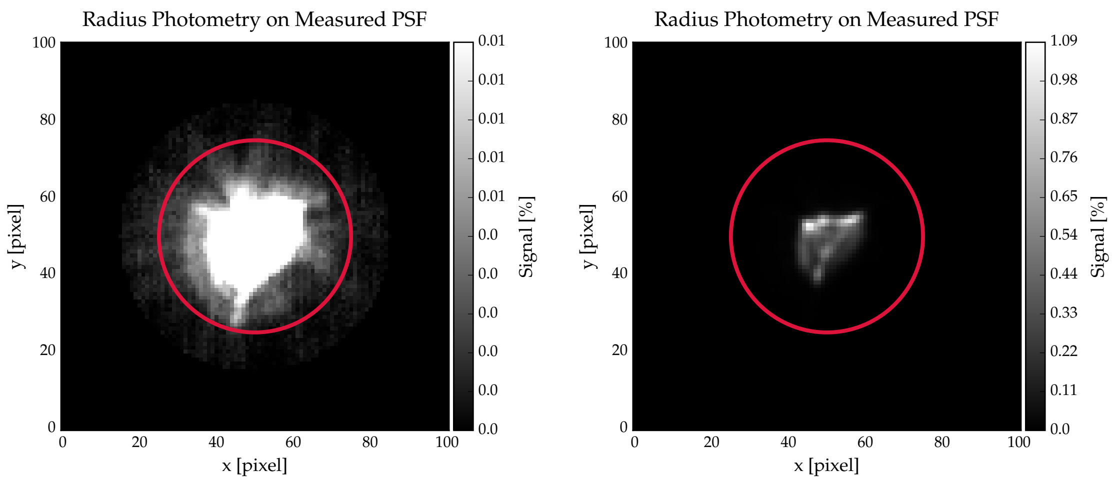

Figure 2-8: Real PSF shape (left) and the high contrast signal distribution (right).

2.3.3.2 Background Signal

The background signal is calculated for the observation specific exposure time and includes estimates for *bias*, *dark current* and *sky signal*. It is estimated rather than directly measured in favour of the execution times, since this reduces the amount of slow operations on the full frame image. The calculation can be seen in Eq.: 2.8 below:

$$\text{bkgd\_signal} = \text{bias} + \text{exposure\_time} \times (\text{sky\_bkgd} + \text{dark\_mean}) \tag{2.8}$$

2.3.4 Reference Target Signal Calculation

The reference target signal in ADU for the photometric methods is calculated from the V-band magnitudes of the Gaia star catalogue. Besides a slight colour correction for CHEOPS V-magnitudes, it is important to account for the object specific spectral distributions, as they highly affect the electron flux on the CCD. A more detailed description of the conversion can be found in section 3.2.3 of the *Star Map Generator Tool*. The prediction of the star signal is currently limited by this conversion. It is accurate to about 10%, which is significantly higher than any other remaining source of signal noise. Therefore, it is also the limiting factor of the photometric validation options. This 10 % discrepancy stems from differences in the signal calculation between the ground segment team and *CHEOPSim* and is currently subject to investigation.

3 Star Map Generation Tool

Most parameters for the *Target Acquisition* are target specific and have to be provided to the spacecraft for each observation. This is done in the form of the *Star Map Command* telemetry package (see section 3.4), which is created by the *Star Map Generation Tool* (SMGT). It is built upon a number of *Python* scripts that enable a full-fledged simulation of the acquisition process. The SMGT core features include an automatic reduction of the FOV specific Gaia star catalogue to the brightest *reference stars* and based on that, the selection of the best suited *Acquisition Algorithm*. Following this, all relevant algorithm parameters are configured accordingly and are then tested in various FOV orientations by the acquisition simulation. Depending on the test results, either the *Star Map Command* can be created, or detailed log files and FOV visualisation can be used to adjust the acquisition process. Since every CHEOPS observation needs such an individually configured Star Map Command, the scripts were designed with large scale automated batch processing in mind. Therefore, their functionality was split to divide the whole process into the the following basic steps:

1. Algorithm parameter determination
2. Test data generation
3. Target acquisition performance simulation
4. Star Map generation
5. Simulation visualisation (optional)
6. Star Map visualisation (optional)

All of the above scripts share their resulting data via an *Output* folder that can be defined in the SMGT constants. A more detailed description of each script will be presented in this chapter.

3.1 Algorithm Parameter Determination

The manual selection of the optimal acquisition algorithm and its respective parameters can be very difficult for non trivial cases that cannot rely on the photometric identification. For this reason, the *Algorithm Parameter Determination* script was designed to autonomously find the best algorithm and an optimised configuration for a given FOV. The result is a set observation specific reference stars as well as values for the *detection threshold* and *extraction radius* for the *Star Extraction*. They are determined in various stages as described in the subsections below. Note that all mentioned magnitudes are meant to be CHEOPS V magnitudes if not stated otherwise.

3.1.1 Algorithm Selection

The Target Acquisition can be configured to use one of the following identification algorithms or combinations of them

1. Magnitude Validation Acquisition Algorithm (MVAA)
2. Angle Method Acquisition (AMA)
3. Angle Method Acquisition with Magnitude Validation (AMAMV)

This selection can either be specified by the operator or left to the Star Map Generation Tool (see section 3.6 on input data and List.: 3.1 and 3.3), which automatically decides according to the reference stars. Generally, the photometry supported acquisition with the MVAA is the simplest method for the target identification and is suitable to be used for FOV, where the target has a distinct brightness compared to its surrounding stars. It will only be used for the automatic configuration when the target is the brightest FOV star and brighter than 10 mag. Fainter or photometrically more ambiguous targets will be identified with one of the two FOV geometry based Angle Method variants. While both of them use the same AMA, the second option is able to use the target magnitude as a secondary validation layer, which helps to confirm weak AMA results. It is used by default for observations that provide brightness data for the target star.

3.1.2 Reference Star Selection

The first configuration step for each identification algorithm is the analysis of the given FOV and as a result, the selection of up to 60 reference stars. This maximum number of stars was chosen as a compromise between the orientation specific reference star coverage for the acquisition algorithm and their memory requirements. The coordinates of the reference stars are shifted such that the target is located in the centre of the FOV and the remaining stars surround it. The star selection is then performed considering the following three criteria:

- **Target Detection Threshold [ADU/s]:**
  A temporary detection threshold that consists of the target magnitude plus a safety margin of two times the magnitude tolerance. This should guarantee target detection and serves as a starting point for the reference star selection.

$$TDT = m_t + 2 \cdot \Delta m_t \tag{3.1}$$

  This threshold is used in units of *ADU/s*. The detailed conversion from magnitudes to ADU is further described in subsection 3.2.3

- **Candidate Radius [px]:**
  A radius defined by the expected absolute pointing error (APE) of an observation. The target star will be found in the *candidate area* which is the area covered by the candidate radius around the intended target location.

- **Maximum FOV Radius [px]:**
  A radius that covers the FOV visibility for all possible orientations. The calculation includes the spacecraft *FOV radius*, *candidate radius* and the intended *target location* offset ΔTL from the FOV centre:

$$r_{FOV_{max}} = r_{FOV} + r_C + \Delta TL \tag{3.2}$$

These three quantities are used to discard all stars, that are located outside of the maximum FOV radius. The remaining stars are then grouped in two sets, that separate them into stars above (brighter) and below (fainter) the target detection threshold. The subset above the threshold is divided further into two groups, which feature objects inside and outside of an area defined by twice the candidate radius. This doubled radius also includes all stars that can be located within the candidate area for all possible pointing errors of the observed case. The selection process can be seen in Fig.: 3-1. In addition to the selection, also the number of stars in each group are stored for later use. After sorting reference stars by their magnitudes, they will primarily be selected from the group of stars above the detection threshold. Any further and more nuanced selection is algorithm specific and will be described in the following subsections.

3.1.2.1 Magnitude Validation Acquisition Algorithm

The selection for the Magnitude Validation Acquisition is the simplest of all three options. Here, only the target star will be provided for the on-board acquisition by the Star Map Command. Since the target star is part of the group of stars within the candidate radius, the number of stars in the candidate area is checked to be non-zero as a fail safe.

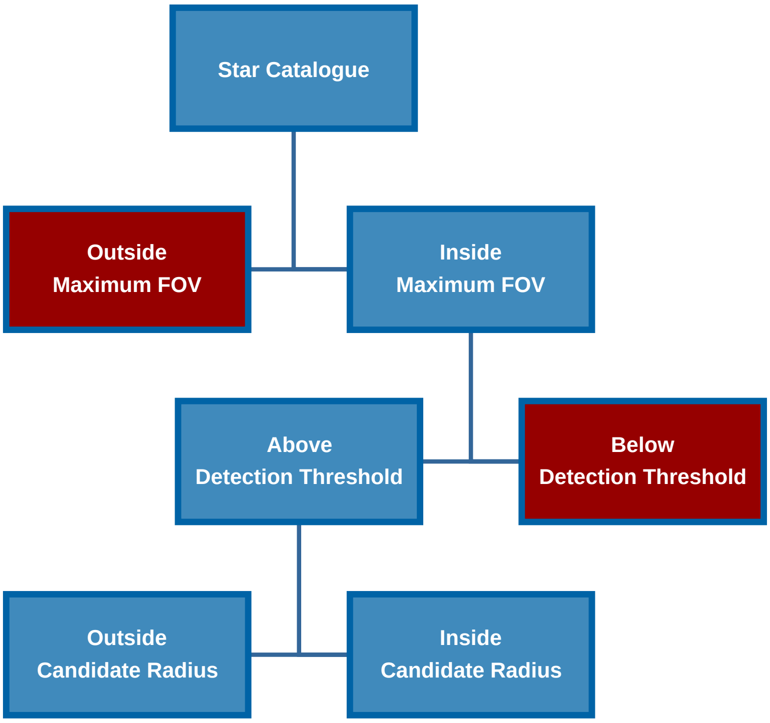

Figure 3-1: FOV grouping process during the star selection.

In addition, the operator is warned about using this algorithm if the target star is fainter than 10 mag. This magnitude is chosen as the threshold at which stars similar magnitudes to the target can appear in the FOV. Although very unlikely, it could possibly lead to misidentifications if the target location changed right before the observation or if it was misplaced by the operator. Since only the detection of the target star is necessary in this case, the Star Extraction is set to use the *Reduced Extraction* mode on the *candidate radius*. In the case of additional stars within the candidate area, their signals are compared with the *reference target signal* to warn the operator if any difficulties are to be expected. In addition, the first reference star below the *target detection threshold* is determined in preparation for the subsequent cosmic ray stability tests.

3.1.2.2 Angle Method Algorithm

A proper star selection for the Angle Method is crucial for its success and difficult to do manually, which was the initial reason for the development of the Star Map Generation Tool. The reference stars have to be selected to cover all stars that the on-board acquisition will be able to detect with the provided configuration. In this step, it is crucial to prevent the detection of any interloping stars, as they will likely degrade identification result (see section 2.2.2.3). Therefore, a minimum star density of 12 stars for a full frame observation is used to calculate the number of reference stars N_{RS} for the area $A_{FOV_{max}}$, that is covered by the maximum FOV radius.

$$N_{RS} = A_{FOV_{max}}/A_{FOV_{obs}} \cdot 12 \tag{3.3}$$

This number was chosen higher than the necessary minimum for the successful operation of the Angle Method for two reasons. The increased number of reference stars enables a configuration of the detection threshold such that the faintest reference stars also cover the most likely interlopers for a given observation (section 3.1.3). Any still occurring interlopers, can be mitigated by the remaining star density as described in section 2.2.2.3 about interloper effects. In combination, this will increase the identification success rates in challenging observations.

The reference stars are then selected from the previously grouped FOV stars. This selection logic depends on whether the number N_a of FOV stars above the target detection threshold exceeds N_{RS}.:

- **$N_a <= N_{RS}$:** In this case, not enough stars are available for the employed detection threshold. Therefore, the whole set of N FOV stars are sorted by their signal in descending order, whereas the target star is kept at the first position. The first N_{RS} stars are then selected as reference stars and the detection threshold will be adjusted in a subsequent step (section 3.1.3).
- **$N_a > N_{RS}$:** Here, the number of available stars have to be reduced further. For this reason, the stars above the detection threshold are sorted by their distance to the target star. The N_{RS} closest stars are then selected as reference stars. To avoid on-board detections beyond the distance of the farthest reference star, the *extraction radius* is set to this distance. Since Star Extraction up to the *candidate radius* is required to guarantee the detection of the target star, it is maintained as a minimum value for the extraction radius. Configurations that break this condition produce a warning.

The above described selection process is visualised in Fig.: 3-2.

3.1.2.3 Angle Method with Magnitude Validation Algorithm

The star selection for this combination of identification algorithms is mostly identical to the selection for the Angle Method Acquisition as described above. The only difference is an additional check to ensure, that the photometric data for the target stars is available.

3.1.2.4 Automatic Selection

Since CHEOPS will also observe many bright targets (see science requirements in Tab.: 1.1), the automated algorithm selection is designed such that it will initially try to set the iden-

Figure 3-2: Reference star selection for the Angle Method Algorithm.

tification method to the Magnitude Validation Acquisition Algorithm. If any of the warnings, as described in section 3.1.2.1 occur, the FOV will be considered unfit for a purely photometric identification. Instead, it will be configured for the Angle Method Acquisition or, if applicable, its combination with and Magnitude Validation. The automatic star selection follows the same logic as the manually configured Angle Method Acquisition (section 3.1.2.3).

3.1.3 Detection Threshold

Whether the initially calculated *target detection threshold* can be used depends on the selected identification algorithm and its respective set of reference stars. While the threshold is usually well configured for identifications with the Magnitude Validation Acquisition, it always has to be altered for the Angle Method Acquisition. This is done with the prevention of interloping stars in mind, as already described for the calculation of the number of reference stars (section 3.1.2.2). As a consequence, the set of reference stars will contain more stars than will be detected by the on-board Star Extraction. In particular, about 3-5 reference stars should remain as margin against interlopers. This is achieved by setting the detection threshold to contain the 85th percentile of the brightest N_{RS} reference stars. The remaining buffer stars are the most likely candidates to become interlopers by additional signal from overlapping stars, hot pixels or temporarily increased cosmic ray flux. The signal dispositions from cosmic rays in particular affect all visible stars of an observations. For this reason, a test that explores their susceptibility to become interlopers was implemented. This is further described in the following section.

3.1.4 Cosmic Ray Stability

Intensive cosmic ray bombardment can sometimes be present during passes through the South Atlantic Anomaly (SAA) or periods of high solar activity. This will introduce an additional and unaccounted component to the background signal for each observation. As a result, stars that are only slightly below the detection threshold can gain enough additional signal to be detected as interloping stars. Since this poses a problem to acquisition with the *Angle Method* algorithms, each reference star selection is concluded with a cosmic ray stability test. Therefore, the expected signal of the faintest reference star is compared to the signal of the first non reference star. The *detection threshold* passes the test if the signal difference is large enough so that the known non reference stars are not detected in cosmic ray environments with up to 150 times the nominal rate. In this case the detection threshold is confirmed and used for the on-board Star Extraction. If the test fails, it is corrected accordingly. The average cosmic ray signal is calculated for the 40x40 px area, that is used for the region of interests during the *Star Extraction* and can be seen in Tab.: 3.1.

Cosmic Ray Rate	**10x**	**100x**	**1000x**
ROI Signal [ADU/s]	105	1015	9673

Table 3.1: Cosmic ray signal deposition for an extraction area of 40x40 px ROI.

This rate was derived from simulated *CHEOPSim* frames that were particularly produced for testing in SAA environments and is presented in section 4.2.4. Due to its similar orbit, the cosmic ray models of *CHEOPSim* are based on the rates that were observed by the Hubble Space Telescope (HST) [Futyan, 2018]. The factor 150 was extrapolated from the tenfold flux and is conservatively chosen to be well beyond the requirement for science operation (see Tab.: 1.1). It will enable target reacquisition while CHEOPS leaves the SAA and will help to optimise the available observation time. All cosmic ray related values can be adjusted in the constants configuration file of the *Star Map Generator Tool*. A visual representation of the increased cosmic ray flux within the SAA is given in Fig.: 3-3.

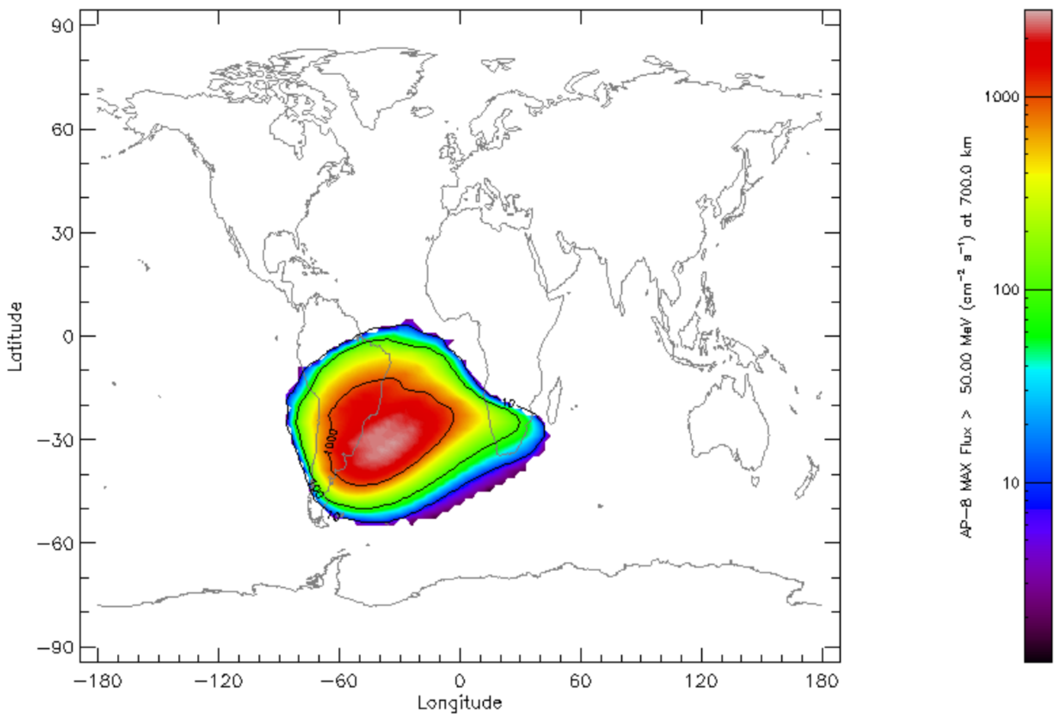

Figure 3-3: Relative increase of the cosmic ray flux within the SAA. This figure is illustrative, to inform on the choice of value for the flux increase and does not represent the SAA model used in *CHEOPSim* [Futyan, 2018].

3.2 Test Data Generation

With all of the algorithm parameters in place, the next step is the simulation of the expected FOV around the target star. This will provide data for the subsequent test of the acquisition algorithm configuration. Therefore, all provided positions from the input star catalogue are converted from RA/DEC to pixel coordinates, shifted and rotated for different FOV orientations and finally distorted to conform with the CHEOPS optics. This input can then be used to simulate an observation with *StarSim* [Ferstl, 2016]. Each step is described in detail in the subsections below. The configuration options for the test data generation are shown in List.: 3.3.

3.2.1 Star Coordinate Conversion

All operations on simulated and observed images will be performed in pixel coordinates. Therefore, a conversion from right ascension and declination as provided by the GAIA catalogue becomes necessary. With a pixel size of about 1″ and the resulting narrow FOV, a gnomonic projection was chosen to transfer the FOV onto the CCD plane. It was implemented by using the *coordinate* functions in the *Astropy* Python library [Robitaille & Astropy Collaboration, 2013]. The resulting *reference frame coordinates* are chosen such that the target star is placed in the centre of an arbitrarily sized reference image, that covers all possible FOV orientations. This reference image can be used for visual inspection of the acquisition results and is described in section 3.5. A further transformation gives the coordinates on the observed 1024x1024px full frame CCD image. These *observed frame coordinates* can be rotated and shifted to either random or pre-defined orientations for the acquisition algorithm performance tests. Simulations are performed in the *random attitude* mode per default. Here the first simulated image matches the orientation of the reference frame coordinates, which simplifies the visual inspection. Any further simulations are rotated and shifted randomly within the defined absolute pointing error. For better statistics, it is suggested to test the acquisition algorithm performance on multiple FOV orientations, since the results can be rotation dependent. This can be configured via the number of *runs* (List.: 3.3). The observed frame coordinates are also used for self evaluation of the Target Acquisition results and its respective simulation log files (see section 3.7).

3.2.2 Optical Distortion Simulation

As with most optical systems, the CHEOPS telescope will introduce a slight, radially symmetric distortion towards its FOV edges. While this doesn't affect target identification with the Magnitude Validation Algorithm, it can possibly degrade the results of the Angle Method Algorithm. This is especially true for FOV with large star separations or non-central Target Locations, where the star distances can be affected by up to 7″ along the diagonals. A visual representation that clearly shows the radially inwards bound distortion is shown in Fig.: 3-4.

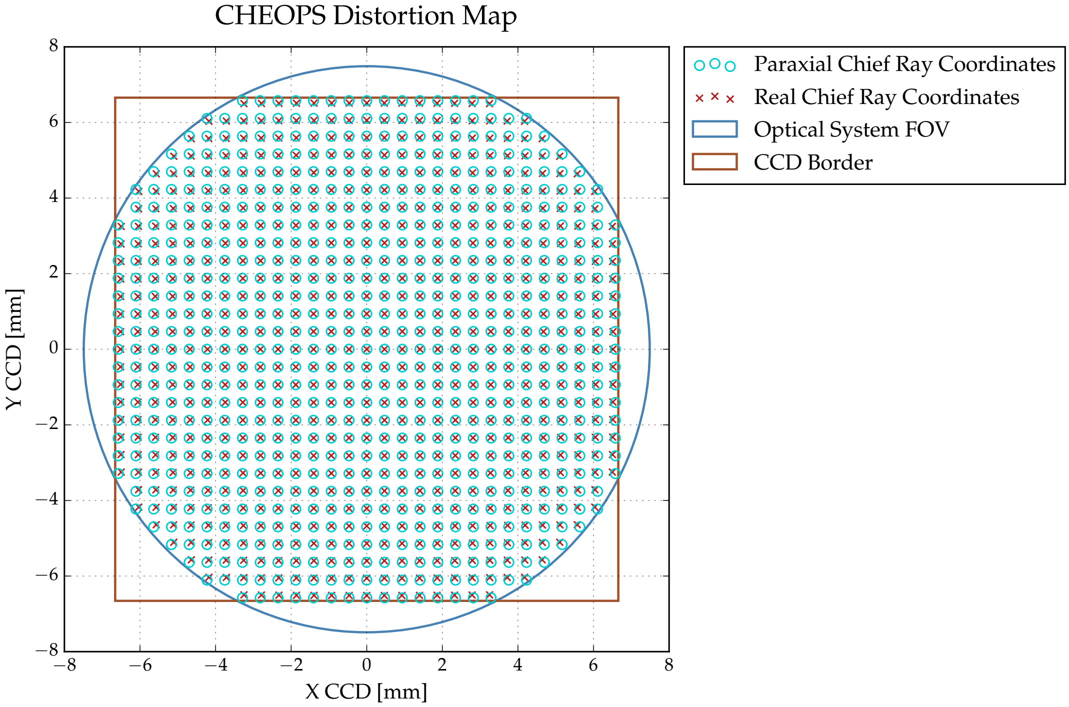

Figure 3-4: Distortion map of the CHEOPS optical system. The difference between the real and paraxial chief rays shows a radial distortion towards the optical axis. Distortion map data based on Ottensamer [2016].

For this reason, a distortion correction was added to the Target Acquisition system and a distortion simulation for all reference star positions was implemented for *StarSim* (see section 3.2.4). The used distortion model is based on the above distortion map and is described by a 4^{th} order polynomial, which is represented by the distortion factor θ in Eq.: 3.4.

$$\theta = 1.0 + a_2 \cdot r^2 + a_4 \cdot r^4 \tag{3.4}$$

Here r describes the star position as a distance from the optical axis, while $a_2 = -3.6994 \cdot 10^{-8}$ and $a_4 = -2.3341 \cdot 10^{-15}$ are the 2^{nd} and 4^{th} distortion terms. The respective correction is applied as part of the on-board instrument flight software (IFSW) and the *Target Acquisition Performance Simulation* script (see section 3.3). Therefore, the Eq.: 3.4 is reused with $a_2 = 3.69355 \cdot 10^{-8}$ and $a_4 = 7.03436 \cdot 10^{-15}$ as correction coefficients. The detailed characterisation of the distortion model, as well as the implementations for the distortion and correction can be found in [Weiss, 2016].

3.2.3 Star Signal Calculation

Representative FOV simulations for the acquisition tests with the *Magnitude Validation Algorithm* require an accurate conversion from the star magnitudes in the catalogue to the detected signal on the telescope CCD. Since the CHEOPS CCD is only sensitive over the range of 330-1100 nm, the spectral energy distribution of the star has to be factored into the calculation of the photon flux. This spectral energy distribution is approximated with a black body spectrum of the respective effective temperature of the catalogue star. The photon flux at a given wavelength is proportional to the energy multiplied by the wavelength ($E = hc/\lambda$). For the case of Vega, the spectral energy distribution (SED) is approximated with a black body with $T_{eff} = 9600K$. A definition of additionally used quantities is given by Tab.: 3.2 [Billot & Futyan, 2017]:

Symbol	Description
X	CHEOPS magnitude
X_0	CHEOPS magnitude of Vega
V	V-band magnitude
V_0	V-band magnitude of Vega
F	Stellar Flux (number of photon/s incident on the telescope aperture) over the range 330-1100nm
F_X	Photon flux (number of photons/s incident on the CCD, after integration over the optical throughput of CHEOPS) over the CHEOPS range of 330-1100nm
F_{X_0}	Photon flux of the Vega (number of photons/s incident on the CCD for the Vega, after integration over the optical throughput of CHEOPS) over the CHEOPS range of 330-1100nm
F_V	V-band Flux (number of photons/s after integration over the transmission of the V-band filter)
F_{V_0}	V-band Flux of Vega (number of photons/s for Vega after integration over the transmission of the V-band filter)
QE	Quantum Efficiency (wavelength dependent, is set for the mission duration)
OT	Optical Throughput (wavelength dependent, is set for the mission duration)
T_{eff}	Effective Temperature of the star considered (in Kelvin)
SED	Spectral energy distribution in the CHEOPS range of 330-1100 nm
e^-	Number of electrons generated by photons incident on the CCD
g	Conversion factor for ADU gained from e^-
ADU	Number of ADUs read from the CCD

Table 3.2: Relevant parameters for the conversion of the CHEOPS magnitude to CCD signal in ADU.

The conversion between V and CHEOPS (X) magnitudes is achieved by defining the X magnitude of Vega to 0.035, which is estimated to be a photon flux of $3.22073906881031 \cdot 10^9$ *photons/s* [Billot & Futyan, 2017]. The respective calculations are based on the standard equations for apparent magnitudes as shown in Eqs.: 3.5-3.7.

$$X - X_0 = -2.5 \cdot \log\left(\frac{F_X}{F_{X_0}}\right) \tag{3.5}$$

$$V - V_0 = -2.5 \cdot \log\left(\frac{F_V}{F_{V_0}}\right) \tag{3.6}$$

$$X - V = -2.5 \cdot \log\left(\frac{F_X \cdot F_{V_0}}{F_{X_0} \cdot F_V}\right) \tag{3.7}$$

For the conversion to *ADU* the number of incident *photons* is first converted into e^- at CCD level (Eq.: 3.9) with the electron production factor γ (Eq.: 3.8). This factor depends on the spectral energy distribution and is provided in the form of a flux conversion table with pre-calculated values for effective temperatures in the range from 2000 to 40000 K.

$$\gamma\left(T_{eff}\right) = \frac{\int SED\left(T_{eff}\right) \cdot QT \cdot QE}{\int SED\left(T_{eff}\right) \cdot QT} \tag{3.8}$$

$$e^- = F_X \cdot \gamma\left(T_{eff}\right) \tag{3.9}$$

The electron flux can then easily be further converted to *ADU* by a multiplication with the approximated electron gain g of 0.436 (as of May 2017).

$$\mathrm{ADU} = e^- \cdot 0.436 \tag{3.10}$$

The resulting flux in *ADU/s* is used for any star signal related calculations such as the *Detection Threshold* (section 3.1.3) or FOV simulations with *StarSim*.

3.2.4 Simulation with StarSim

The simulation of observed FOV was implemented with the *StarSim* software [Ferstl, 2016]. This allows to simulate telescopic observations of stellar fields in consideration of the specific instrumental features of space missions. It is an entirely autonomous Python programme that was initially designed to investigate the performance of high precision centroiding algorithms. The simulated images include features such as detector size, point spread function, the spacecraft jitter and rotation. In particular, *StarSim* is capable of simulating characteristics of charged-couple devices (CCD) like the full well capacity, dark current, hot-pixels, bias, read-noise as well as variations in the pixel sensitivities on an intra-pixel scale. Observations of stellar fields can be simulated by specifying the position and the signal of each star. The signals are usually defined on sensor-level in units of photons per second. Therefore, the signal reduction caused by light passage through the optical components of the instrument (like aperture, beam splitters, dichroics, etc.) have to be pre-calculated. The final star signals in the image are further affected by the specified quantum efficiency and exposure time. In the current version of *StarSim* only simulations of monochromatic light are supported. Therefore, the contribution to the total flux of different wavelengths has to be pre-calculated. For the integration into the Star Map Generation Tool the input requirements were adapted to also support fully pre-calculated signals on the detector in ADU. The output files are provided in a compact FITS-format for further processing. In the CHEOPS mission, the satellite will temporarily experience an increased rate of cosmic ray hits during its passage through the South Atlantic Anomaly. Cosmic ray hits cause glitches on the image, which are unwanted features in the form of single or multiple bright pixels. In *StarSim*, the rate, intensity, size distribution of glitches can be included in simulated observations. Such models were derived from MOST observations, as CHEOPS will have similar orbit and detector characteristics. The derived models were included in all simulations. The following characteristics were not considered in the simulations: chip temperature, blooming, fringing, dead pixels, charge transfer inefficiency, read-out speeds, wavelength of incident light and dynamic properties like changes of bias in time. A complete list of configuration parameters and features as well as the above mentioned cosmic ray model is described in the master's thesis *Optimised Centroiding of Stars for Space Applications* [Ferstl, 2016].

3.3 Target Acquisition Performance Simulation

After the successful preparation of the algorithm parameters and simulated observations, they can now be utilised to test the expected Target Acquisition performance. Therefore, the configuration is applied to the Python analogue to the *Star Extraction*, *distortion correction* and the respective *identification algorithm*. They are then tested on the simulated observation(s). The operator is presented with a coarse overview about the validity of the result and one of three verdicts:

- Successful
- Weak, review suggested
- Failed, review necessary

For the last two cases, extended log files that document each step of the Target Acquisition are available for debugging (see section 3.7).

During the development and initial testing of the acquisition algorithms, it was noticed that the most common source of acquisition failures are jointly detected positions that stem from combined signals of overlapping PSFs. Since this can lead to the complete inability to solve certain FOV with the Angle Method Acquisition, an alternate version of the performance simulation was implemented. With this, the detected star positions from the first simulation can be used as set of reference stars for another iteration of the performance test. Usually, this solves the position offset between the combined and the actual position from the star catalogue, but it might introduce a slight offset to the detected target position. The detailed procedure to replace the initial reference star with the *Star Extraction* output is described in the *Read Me* file of the *Star Map Generator Tool*.

3.4 Star Map Generation

The generation of the *Star Map* is the final step and the main purpose of the *Star Map Generation Tool*. The Star Map is the payload package of the *Star Map Telecommand*, which is described in section 3.4.1. It is a 286 byte large stack of binary data that contains all relevant configuration parameters for the *Target Acquisition* as outlined in the previous sections. This package size is also maintained for payloads with less than the maximum amount of reference stars. In such a case, the remaining space is filled with zeroes. The same is true for unused algorithm specific parameters, that are not required for the current observation. In addition, the SMGT provides functionality to inspect previously created Star Maps.

3.4.1 Star Map Layout

Star Map Telecommand			
Size [Bit]	Data Type	Parameter	Description
32	UINT	OBSID	Unique identifier for the observation
16	USHORT	AcqAlgoId	
32	UINT	SPARE	Former parameter "TargetStar" has been deleted
2208		SkyPattern	Algorithm Data - details following below
The SkyPattern is made up of the following data structure			
24	UINT24	Target_Location_X	Position on the CCD (in centipixels where the target is intended to be located. Origin = bottom left pixel corner (centre of bottom left pixel is thus [50/50]), counting in Cartesian coordinates.
24	UINT24	Target_Location_Y	same for y-axis
8	UCHAR	Algorithm ID	which algorithm is to be selected for the Target Acquisition 0 = None, 1 = MVA, 2 = AMA, 3 = AMA+MVA
16	USHORT	SPARE	former execution time (removed)
16	USHORT	SPARE	former delay time (removed)
16	USHORT	Distance Threshold	Absolute distance between measured position and Target_Location under which we switch from acquisition to centroiding.
8	UCHAR	Iterations	Maximum number of iterations. Default: 10
Algorithm Parameters			Parameters needed for the tuning of the algorithm. These are generated by the SMGT
16	USHORT	SPARE	former Rebinning Factor. Now hard coded.
16	USHORT	Detection Threshold	Sets the detection threshold for the Star Extraction. Default: 5200 [10 ADU]
16	USHORT	SE_Reduced_Extraction	Limits the Star Extraction to a radius around the expected Target Location. Default: False
16	USHORT	SE_Reduced_Radius	Sets the reduced extraction radius for the Star Extraction. Default: 392 pix
16	USHORT	SE_Tolerance	Maximum positional error in Star Extraction results. Default: 5 pix
16	USHORT	MVA_Tolerance	Maximum photometric error for the Magnitude Validation Method. Default: 15 percent
16	USHORT	AMA_Tolerance	Maximum error for distance vectors. Default: 3 pix
16	USHORT	Pointing_Uncertainty	Maximum expected pointing error from the Target Location. Default: 150 pix
32	UINT	Target Signal	Signal of the target in ADU/s
16	USHORT	Number of Stars	Number of stars included in the sky pattern
1920	BINARY	Pattern	Data field ("Sky Pattern") with star entries according to algorithm 920 bits = 120 shorts

Table 3.3: The detailed contents of the Star Map Telecommand.

3.5 Visualisation

The visualisation of the acquisition results is an optional step to identify FOV geometry related issues with the acquisition algorithm or its configuration. Therefore, the user can select any previously simulated FOV by its observation ID, which is then resimulated with its respective acquisition algorithm configuration. The presented FOV information can be seen in Fig.: 3-5. It includes the FOV from the perspective of the *reference frame coordinates* (left), the simulated CHEOPS on-board view in the *observed frame coordinates* (right) and two sliders to control the contrast (bottom).

3.5.1 Reference Frame FOV

This view features all provided stars from the star catalogue. It also highlights all selected Reference Stars (red circle) and is centred around the *target star* (green circles). In addition, it also displays the orientation of the *CHEOPS full frame observation* (yellow square) and the location of the *science frame* (cyan square), which is centred around the selected *target location*. The large circles mark the *maximum covered FOV* (blue), the *reduced extraction area* (orange) and the *candidate area* (red). The latter includes all stars that could be mistaken for the target. It is larger than the Candidate Area in the CHEOPS FOV, since all possible FOV orientations are considered for the reference view.

3.5.2 CHEOPS Frame FOV

While all of the colour codes for the FOV description are identical to the ones in the reference FOV on the left, the star markers now highlight the *observed positions* (red) and the *identified target* (green). In addition, *two arrows* (yellow) indicate the necessary corrections in the x and y direction so that the target star will be moved to the intended target location. This side by side comparison of the *observed stars* (right) and *reference stars* (left) provides a rather quick way to visually verify the acquisition results. It is also very useful to determine the reasons behind identification failures. The two most common reasons are interloping star detections or jointly detected overlapping stars, which can be spotted easily. Once identified, the problematic stars can often be excluded by a manual adjustment of the detection threshold, which can also be estimated from the visualisation.

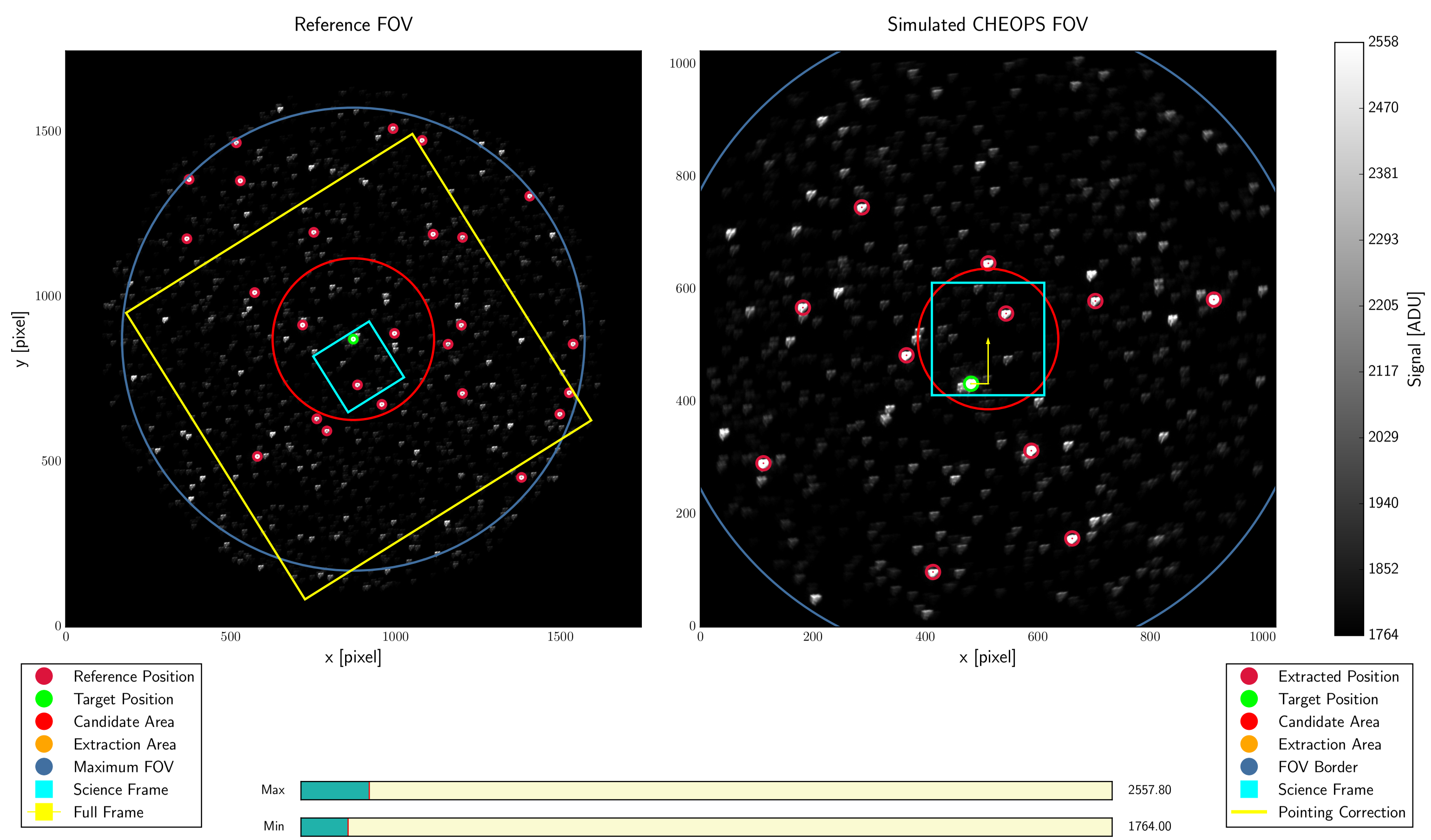

Figure 3-5: Visual output of the *SMGT* as seen by the operator .

3.6 Input Data

The Star Map Generation Tool uses field of view (FOV) specific data to automatically determine the Target Acquisition related parameters. All necessary parameters are provided with a XML file and a star catalogue in FITS format. The former contains observation specific data such as the intended target location on the CCD [px] and an estimate for the pointing error [px]. The latter features the star positions (RA/DEC), brightness (mag) and effective temperature [K] of all possibly visible FOV stars. Examples of the config files are shown in List.: 3.1, 3.2 and Tab.: 3.4 below.

```xml
<TACQ_Config>
  <Data_Block>
    <!-- Star Map specific parameters                                        -->
    <General>
      <!-- Unique identifier for the observation                     (INT) -->
      <OBSID>0000</OBSID>
      <!-- Define selected Target Acquisition algorithm
           0...None, 1...MVA, 2...AMA, 3...AMA + MVA                 (INT) -->
      <Algorithm_ID>3</Algorithm_ID>
      <!-- Absolute distance between measured position and Target_Location
           under which we switch from acquisition to centroiding.    (INT) -->
      <Distance_Threshold>5</Distance_Threshold>
      <!-- Maximum number of iterations. 0 = inf (INT)                      -->
      <Iterations>10</Iterations>
      <!-- Intended target position on the CCD (in centi-pixel).
           Origin = bottom left pixel corner, Cartesian coordinates. (INT) -->
      <Target_Location_X>51150</Target_Location_X>
      <!-- same for Y axis (INT)                                            -->
      <Target_Location_Y>51150</Target_Location_Y>
      <!-- Star tracker induced pointing uncertainty in pixel        (INT) -->
      <Pointing_Uncertainty>120</Pointing_Uncertainty>
      <!-- Acquisition Exposure Time in milliseconds (INT)                  -->
      <Exposure_Time_Acquisition>10000</Exposure_Time_Acquisition>
      <!-- Path to the text file that contains the FOV information (STRING) -->
      <Star_Catalogue_Filename>StarCatalogue.fits</Star_Catalogue_Filename>
      <!-- Star Map output filename                               (STRING) -->
      <Star_Map_Filename>StarMapName.bin</Star_Map_Filename>
    </General>
    ...
  </Data_Block>
</TACQ_Config>
```

Listing 3.1: General parameters in Target Acquisition configuration file

All user defined input parameters are stored in the *<General>* branch. The resulting acquisition parameter output is added and stored in this XML file. They can be found in their respective branches as seen in List.: 3.2.

```xml
<TACQ_Config>
  <Data_Block>
    ...
    <!-- Star Extraction specific parameters                              -->
    <Star_Extraction>
      <!-- Threshold for the star detection [ADU/s]                (INT) -->
      <SE_Detection_Thld>1020</SE_Detection_Thld>
      <!-- For crowded FOV. Only scans zone around target location (BOOL) -->
      <SE_Reduced_Extraction>False</SE_Reduced_Extraction>
      <!-- Reduced star extraction radius                          (INT) -->
      <SE_Reduced_Radius>400</SE_Reduced_Radius>
      <!-- Worst case star extraction position tolerance [px].     (INT) -->
      <SE_Tolerance>5</SE_Tolerance>
    </Star_Extraction>
    <!-- Angle Method Algorithm specific parameters                       -->
    <Angle_Method_Algorithm>
      <!-- Positional uncertainty [px] for fingerprint creation.   (INT) -->
      <AMA_Tolerance>3</AMA_Tolerance>
    </Angle_Method_Algorithm>
    <!-- Magnitude Validation Algorithm specific parameters               -->
    <Magnitdue_Validation_Algorithm>
      <!-- Signal uncertainty of the target star. Fraction [0-100]. (INT) -->
      <MVA_Tolerance>5</MVA_Tolerance>
    </Magnitdue_Validation_Algorithm>
  </Data_Block>
</TACQ_Config>
```

Listing 3.2: Algorithm parameters in Target Acquisition configuration file

Example Star Catalogue

ID	Target	RA [Deg]	DEC [Deg]	Mag CHEOPS	T_{EFF} [K]
1	true	199.016200	-8.093400	11.899261	5920
2	false	199.007275	-8.079949	18.336101	3850
3	false	199.012275	-8.118769	17.579065	5280
4	false	199.012275	-8.119259	17.996101	3850
...	...	...	...	...	...
n	false	199.012275	-8.120469	17.946101	3850

Table 3.4: Contents of a typical star catalogue FITS file.

In addition, a second XML file is used to configure all simulation related options. These include the number of simulations per FOV, rotation rate, orientation etc. They are usually not observation specific and can be reused over a wide range of different cases. The whole range of options is presented in List.: 3.3.

```xml
<SIM_Config>
  <!-- Simulation specific parameters                                          -->
  <Simulation_Control>
    <!-- Number of simulation runs                                     (INT) -->
    <Runs>1</Runs>
    <!-- Automatically select the best identification algorithm      (BOOL) -->
    <Automatic_Algorithm_Selection>False</Automatic_Algorithm_Selection>
    <!-- Automatically calculate the exposure time according to FOV  (BOOL) -->
    <Auto_Exposure_Time>False</Auto_Exposure_Time>
    <!-- Maximum Exposure time in seconds                            (FLOAT) -->
    <Max_Exposure_Time>10.0</Max_Exposure_Time>
    <!-- Minimum Exposure time in seconds                            (FLOAT) -->
    <Min_Exposure_Time>1.0</Min_Exposure_Time>
    <!-- The speed of the rotation in degrees per second. [0-360]    (FLOAT) -->
    <Rotation_Rate>0.067</Rotation_Rate>
    <!-- Minimum SNR for reference star detection                      (INT) -->
    <Signal_to_Noise_Ratio>50</Signal_to_Noise_Ratio>
    <!-- Below factors are only used if Random_Attitude is set to True       -->
    <Random_Attitude>True</Random_Attitude>
    <!-- x-coordinate of real pointing                                 (INT) -->
    <Pointing_x>552</Pointing_x>
    <!-- y-coordinate of real pointing                                 (INT) -->
    <Pointing_y>552</Pointing_y>
    <!-- Rotation angle in degrees                                     (INT) -->
    <Field_Rotation>90</Field_Rotation>
  </Simulation_Control>
</SIM_Config>
```

Listing 3.3: Simulation parameter configuration file

3.7 Simulation Log Files

All previously described modules of the Star Map Generator Tool produce log files to document the most important steps from the above scripts. Generally, there are two different log types. While both are easily readable by humans, one of them is meant to store run specific information between the simulations so they can be combined to a final result. They are stored in the output location in /TACQ_RESULTS/ and can be used as an additional resource for debugging extraction related issues in acquisition failures. The normal simulation logs for the operator are stored in /LOGS/ and include information about:

1. Algorithm Parameters
2. Star Extraction
3. Angle Method Algorithm
4. Magnitude Validation Algorithm
5. General Simulation Results

The first one provides photometric and geometric information about the Reference Star distribution. In addition, it also contains the results for the Detection Threshold and cosmic ray stability calculations.

The algorithm specific log files (2-4) document every step where data is manipulated. This is especially helpful to identify problems in the Star Extraction process (see Fig.: 2-1) and during the correction steps in the database matching of the Angle Method Acquisition (see section 2.2.2).

Finally, the general log file offers an overview about individual simulation result as well as the combined statistics for all simulations in a observation ID. The latter is calculated from the individual logs in /TACQ_RESULTS/ and serves as a self evaluation functionality for the SMGT results. Information presented here includes *average position errors* of the Star Extraction, *number of detected stars*, *average database matching results*, *average signal error* and *position correction errors*. It is meant to quickly evaluate the SMGT outcome for larger numbers of simulations per FOV.

4
Performance Evaluation

All of the *Acquisition Algorithms* went through several performance tests to determine their optimal configuration and ensure reliable execution in various observational conditions. These tests took place in three different stages:

1. The earliest one featured a prototype of the *Star Extraction*, *Angle Method* and *Grid Method*. It was meant as a proof of concept for the selected algorithms, that were tested on a handful of simulated CHEOPSim images. While the *Star Extraction* and *Angle Method* performed according to our expectations, the *Grid Method* turned out to be too ambiguous with the small number of available stars. While it could have been used, it probably would have needed a more time consuming configuration by the operator. As a consequence, it was dropped in favour of the *Angle Method*.
2. As soon as the core functionality of all *Acquisition Algorithms* was implemented the *Prototype Test Campaign* was used to identify problems in the code. The results also helped to determine the best configuration strategies for the *Star Extraction* and the *Angle Method*. In addition, their strengths and weaknesses could be identified, which was crucial to build the automated *star* and *algorithm selection* routines.
3. The *Performance Test Campaign* was used to test the final implementation of the *Acquisition Algorithms*. Therefore, typical and complicated observational cases were provided by CHEOPSim. They were designed to represent a broad spectrum of situations, that will be encountered during the lifetime of the CHEOPS mission.
4. Eventually the *Star Map Generation Tool* was put through a large series of real science targets in the *Science Case Test Campaign*. This was done in order to assess the automated configuration algorithms and overall identification success on real cases.

Selected results of the *Prototype*, *Performance* and *Science Case Test Campaign* will be presented and discussed in the sections below.

4.1 Prototype Test Campaign

The *Prototype Test Campaign*[1] was performed after the core functionality of all algorithms was implemented. Therefore, a large number of randomly populated FOV was simulated with *StarSim* (see section 3.2.4) and evaluated with the Python implementations of *Star Extraction* and the *Angle Method*. Depending on the test purpose either specific or realistic brightness distributions were used in those FOV. The detailed description of the different model FOV, as well as the test methodology and results are subject of this section.

4.1.1 Brightness Distribution Model

For the brightness distribution for the random FOV simulation the Kepler Input Catalog (KIC) [Latham et al., 2005] was chosen in hindsight of possible follow up observations with CHEOPS and due to the fact that the Gaia catalogue was not yet available at the time. The KIC features stars down to 21 mag and even though it is not complete to this limit, it covers the magnitude range of all possible targets and the vast majority of the background stars for the anticipated exposure times. Roughly 13.2 million stars in the KIC sky were used to estimate the number of stars as well as the brightness distribution for an observation with CHEOPS. The cumulative distribution can be seen in Fig.: 4-1 below:

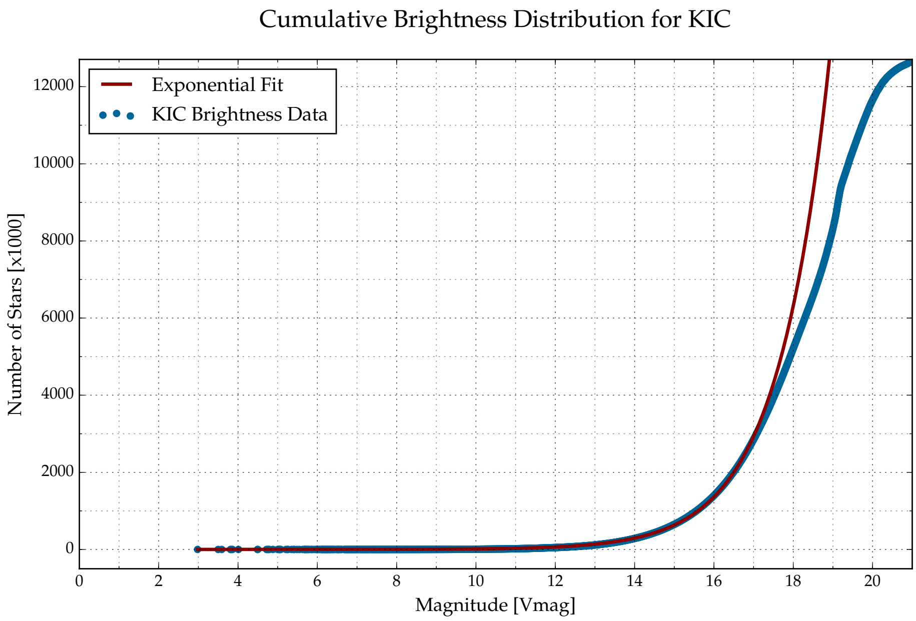

Figure 4-1: Cumulative Brightness Distribution of the Kepler Input Catalog.

It can clearly be seen that the catalogue slightly stops following the exponential trend and starts being incomplete around 17 mag. This effect is even more prominent from 19 mag

[1]Note that some of these results have also been published in Loeschl et al. [2016]

onwards. Since the main focus in the simulations was on targets from about 6-13 mag and background objects down to 15-16 mag, it was decided to exclude stars fainter than 17 mag from the fitted model. Anything below this limit will hardly contribute to the short acquisition exposure times of up to a maximum of 10-20s.
The cumulative brightness curve was fitted with an exponential model. In addition, it was adjusted for the CHEOPS FOV to result in the number of <17 mag stars that can be expected in a typical observation. The resulting model for the star count can be seen in Eq.: 4.1:

$$N = \frac{A_{FOV}}{A_{KIC}} \cdot [a \cdot \exp(b \cdot x) - c] \tag{4.1}$$

$$a = +6.42963071$$

$$b = +0.76650186$$

$$c = -0.47527595$$

$$A_{KIC} = 177^{\square^\circ} \tag{4.2}$$

Using the CHEOPS FOV radius of 19.2′, the CCD sensor size of about 17′ and Eq.: 4.3 to calculate A_{FOV} gives an overlapping area of $0.073^{\square^\circ}$ and therefore a total number of $N = 1210$ stars for a simulated observation.

$$A_{FOV} = (\pi - 4\theta) \cdot r^2 + 4 \cdot a \cdot r \cdot sin\theta \tag{4.3}$$

Note that only about 21 of them are of magnitude 12 or brighter, so the majority of those stars will contribute to the background signals in the observations. Compared to the typical observations that were provided for the *Final Test Campaign*, this population can be considered to be a rather crowded case. This is the result of a rather poor fit, that overestimates the number of bright targets in the FOV. Nevertheless, the model was used to stress the following *Angle Method* performance tests, as the crowded case introduces an additional difficulty of overlapping stars.

4.1.2 Star Extraction Performance

The Star Extraction performance was tested with a Monte Carlo simulation approach. Therefore, 10000 different FOV were populated with magnitude 12 stars, which are the faintest planned targets for nominal observations (SciReq 1.2 Tab.: 1.1). These 10000 FOV were split into 10 sets of 1000 simulations with exposure times ranging from 1 to 10 seconds. This was meant to identify possible correlations between the signal strength and detected position accuracy, but no such correlation was present in the data. Hence, it can be assumed that magnitude 12 stars achieve a high enough signal to noise ratio to be clearly distinguishable from the background. As a consequence, the sets were recombined and evaluated as a large single data set.

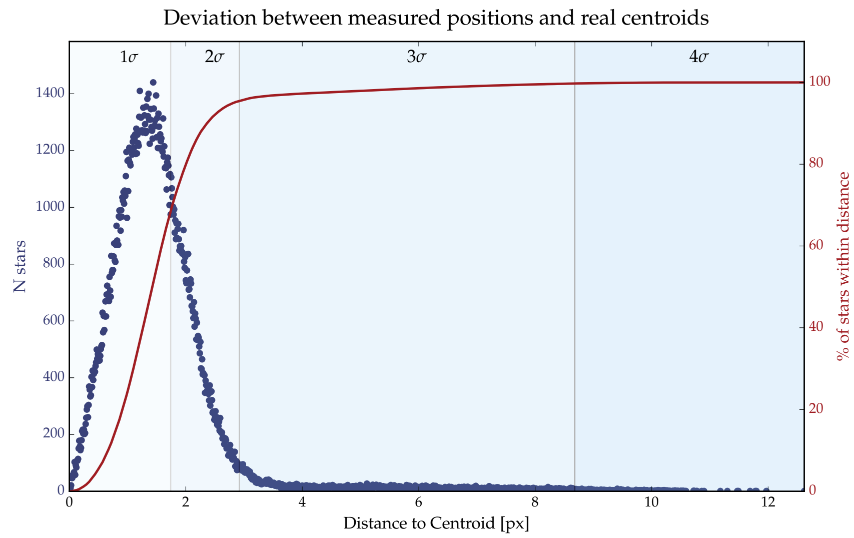

Figure 4-2: Blue data points show the frequency of a certain positional error. The red line is the respective cumulative distribution. The coloured areas in the background indicate the 1–4 σ regions. N=208580

This joint data set consists of 212938 stars of which 97.95% were detected. The results in Fig.: 4-2 show that the extraction error clearly peaks close to the actual positions, but has a long tail of outliers which ends at a distance that corresponds to edge of the PSF. The red cumulative distribution intersects with the border of the 2σ region at 2.9 px. Therefore, 95.45% of extracted stars will be detected with a position accuracy better than 2.9 px from their actual centroid. Calculating the average within the 2σ sub-sample gives a

typical position error of 1.46 ± 0.84 px

compared to an overall position error of 1.57 ± 1.05 px with a maximal error of 12.62 px if the whole data set is taken into account. These values are well in line with the empirically determined ±3 px intra-star lengths error, for which the Angle Method yields the best results.

Closer analysis of the bad fraction of centre of gravity (CoG) results has shown that they exclusively result from cases where two or more stars are imaged close enough that their PSFs overlap. Here, the overlapping neighbour's signal introduces errors, ranging from a small offset to the calculated CoG, to a joint position that won't be recognised as an expected star. This effect directly depends on the overlappers' positions and their relative differences brightness. The closer their positions or magnitudes, the higher is the calculated centroid offset. If both stars have a similar brightness above the detection limit, it usually leads to the detection of a joint position in the overlap region. This is the explanation for both the tail and also the remaining missing 2.05% of non detected stars. Since no targets that overlap with similar bright stars can be observed due to the high precision photometry requirements, this case will not present a problem for the targets within the science requirements of CHEOPS (see SciReq 1.1 & 1.2 Tab.: 1.1). While those joint positions do have an effect on the *Angle Method*, it will not drastically be affected by this. If an observation has a high enough star density to produce this issue, it usually also has enough stars to diminish major problems by the increased size of the observed star database. For more details see section 2.2.2.3 on the effects of interloping stars.

It is noteworthy to mention, that two stars with bad position errors don't necessarily influence the subsequent *Angle Method* results, due to the two dimensional nature of the issue. Major impacts in the algorithm are only expected when the position errors are antiparallel in plane of the connecting edge between two stars. Luckily, this is rather unlikely due to the random nature of the geometrical distribution of the stars. Other effects, like image rotation for longer exposure times in this simulation, also don't seem to affect the results. In this case, smeared objects from long exposures will be detected at the centre with the used CoG algorithm. Though it doesn't find the latest star position on the CCD, the relative positions between the stars are conserved, which is the crucial information for the subsequent identification algorithm. While exposure times, that are significantly longer than 10 seconds won't be necessary for the majority of observations, they can pose a problem to the detection of smeared faint objects. In such situations, it is possible that the detected star signal falls below the Detection Threshold, as it is smeared over areas larger than the region of interest. Luckily, such cases will mostly affect objects far away from the rotation axis, which should be the case exclusively for non target stars. Generally, any such problem should be identified during simulations with the Star Map Generation Tool and can be addressed accordingly.

4.1.3 Angle Method Performance

The initial assessment of the acquisition performance with the Angle Method was meant to proof its feasibility by obtaining general statistics on the algorithm reliability. Therefore, a first test involved Monte Carlo simulations of 1000 random orientations, that were expected to help with the identification of unexpected and difficult situations for the algorithms. Since the non-symmetric PSF introduces a rotational dependency of the signal distribution within overlapping stars, a second series of simulations was performed at different orientations of a distinct FOV. The results for both test cases are presented in the following subsections.

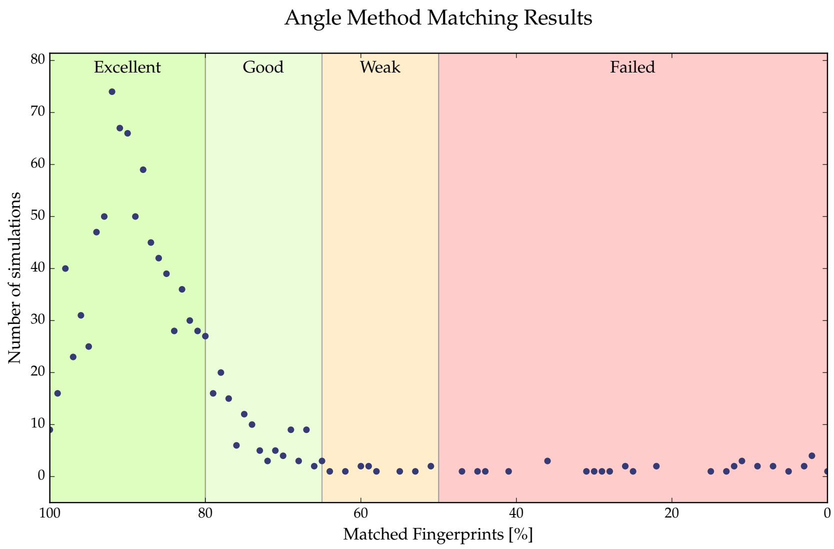

Figure 4-3: Results for simulations the 1000 distinct FOV. Blue data points show the frequency of a certain match result. The coloured background indicates the quality of the match result. It is generally recommended to manually review weak and failed results.

4.1.3.1 Random FOV Tests

The random FOV testing involved the simulation of 1000 distinct FOVs according the the brightness model that was presented in subsection 4.1.1. Each image contains a total of 1210 stars up to magnitude 17, though most of them are lost in the background with the used exposure time of 10s. All 1000 simulations feature a magnitude 12 target with a random pointing error within 120″ from the intended Target Location.

The experiment was meant to provide a general understanding for the frequency of identification problems as well as their sources. In this data set 96.5% of the observations could be identified with a strong average result of 84.94% matched fingerprints. Fig.: 4-3 shows that 95.1% of the results matched more than 65% of the fingerprints and therefore fall into the categories *excellent (>80%)* and *good(>65%)*, which don't necessarily need any additional manual inspection or configuration.

Close inspection of problematic cases showed that the degradation of matching results exclusively originated from inaccurate star position detections. Since a sufficient number of stars to account for the occasional overlap of FOV stars was present in the simulations, all identification failures were caused by insufficient separations and the resulting joint detection of the target and their closest neighbour star. Even though such orientations are not expected during nominal operation, a further analysis and solution to this problem is discussed for the test series with orientation specific FOV in subsection 4.1.3.2.

In addition to the identification success, the measured target position was also compared to its true position for each FOV. Again, only the 95th percentile was considered to assess the nominal operation performance without the influence of the overlapping targets. This gives an **average position error of 1.59 ± 0.81 px**, which is in line with the results from the earlier *Star Extraction* test series.

4.1.3.2 Orientation Specific FOV Tests

The purpose of this test series was to investigate if the ability to solve a specific FOV depends on its observed orientation. Therefore, 100 orientations with the same properties as in the previous test were simulated for a total of 42 different FOVs, which gives a combined data set of 4200 simulated observations.
While the vast majority did not show any rotational dependency, 2 of the 42 FOV were partly affected by identification problems. In particular, a total 24 orientations failed to match, whereas the majority of these attempts could be attributed to a single FOV with 21/100 failures. As expected, these problems were again caused by insufficient separation of the target and a similarly bright close neighbour. Since this is a recurring problem the case was used to tune the *Star Extraction* for better results with short separations. In combination with slight parameter adjustments, the failure rate could be drastically reduced such that only 1 FOV showed matching problems in 2 orientations.

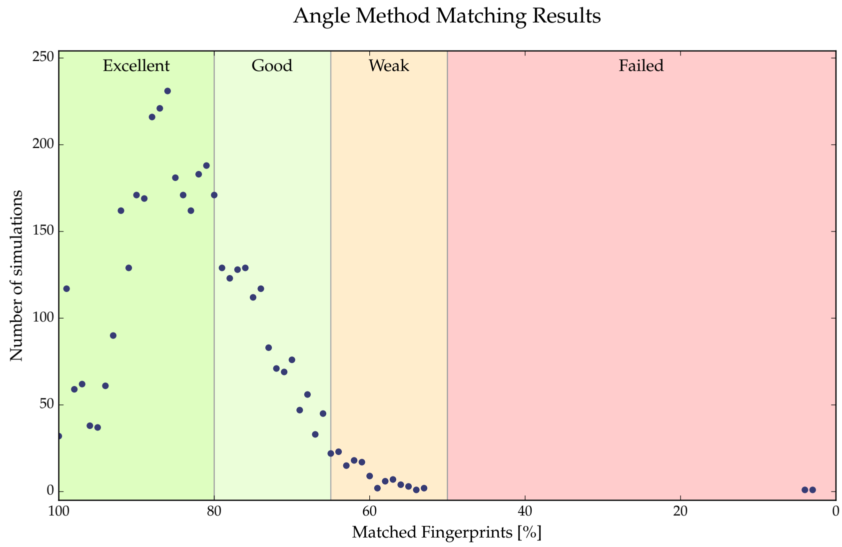

Figure 4-4: Results for simulations the 42 FOV with 100 orientations each. Blue data points show the frequency of a certain match result. The coloured background indicates the quality of the match result. It is generally recommended to manually review weak and failed results.

Utilising these changes to re-evaluate the whole data set with its 4200 simulated observations increased the overall target identification success rate to 99.93% with an average of 82.63% of matched fingerprints.

The analysis of the star positions revealed an **average position error of 1.65 ± 0.837 px**, which was also in line with previous test results. Fig.: 4-4 illustrates the statistics of the match result quality. Here, almost 97% of the cases fall into the categories *excellent* and *good*, which is a positive outlook to the automation of the Target Acquisition configuration.

4.1.4 Prototype Test Conclusions

The *Prototype Test Campaign* showed that the *Star Extraction* and *Angle Method* are generally viable to address the identification of faint targets in well populated FOV. Given the results of the orientation dependent test series, Target Acquisition failures will only pose a minor problem, as the most of the problematic FOV will be identified and adjusted during ground preparations. If the identification was stable enough to pass the ground simulation but still fails on-board, it is likely to be successful on a successive run, since the problem will probably be related to the specific FOV orientation. Generally, the results suggest that the most effective solutions for on-board identification problems will be:

- adjustments to the *detection threshold* if the target position is affected by a faint overlapping star (ground)
- adjustments to the *Angle Method* inter-star length *tolerance* (ground)
- *multiple iterations* over which the telescope can rotate into better orientations if the problem still appears (on-board)
- a priori simulation of *many orientations* to discover problematic FOV

4.2 Performance Test Campaign

The *Performance Test Campaign* was designed to assess the algorithm performance under the most realistic conditions. Therefore, a number of FOV that represent the typical observational cases for the CHEOPS mission, were created in collaboration with the CHEOPS instrument scientist. These simulations covered the anticipated range of target star magnitudes, FOV populations and special but critical situations:

- *General Cases*: Simulations with different target magnitudes, featuring 6 mag, 9 mag and 12 mag targets in sparsely, medium and extremely crowded FOV as demanded by the *science requirements* (Tab.: 1.1). These 9 star populations are also the base for the subsequent special test cases, for which they were modified accordingly.
- *Large Offset Test*: This data set features various target positions with intended large offsets to the image centre. The goal of this test was to show the Target Acquisition's robustness for intended off-centre target locations.
- *True Jitter Precision Test*: A modified version of the *general cases* that simulates jitter induced changes of the pointing. It was meant to identify possible effects on the target centroid accuracy as well as problems with the inter-star distances, that are measured by the *Angle Method Algorithm*.
- *SAA Extreme Cosmic Ray Test*: Here, the 9 mag targets with medium star populations were simulated for observations during passes through the SAA. The simulations feature additional signal from 100x and 1000x increased cosmic ray rates.
- *Maximum Rotation Test*: This was meant as a stress test for the *Angle Method Algorithm*. The data are based on the faint 12 mag target in an extremely crowded FOV and were simulated for the maximum exposure time with the worst case FOV rotation.

Each test case consists of 25 or 50 (*Maximum Rotation Test*) orientations of a specific FOV. The *Star Maps* were created based on the provided star catalogues and are identical for all orientations of a data set. They are automatically created by the *Star Map Generation Tool* for the majority of cases. It will be explicitly stated if a test case required manual alterations to the configuration parameters to result in a successful identification. Note, that the results represent the ability of the automatic configuration of the *Star Map Generator Tool* at that time and have been used to upgrade it where necessary.

Unlike previously tested data, all simulations are products of the official instrument simulator *CHEOPSim* and the acquisition tests were verified with the real instrument flight software on the CHEOPS instrument hardware simulator. The relevant results and important considerations for the most interesting cases are presented in the subsections below. The complete overview of test results can be found in the performance test report. [Ottensamer, 2017].

4.2.1 Off Centre Acquisition Test

4.2.1.1 Central Magnitude 9 Target, Medium FOV Population

Test Case:	TA_FF_01_verylarge_offset_09mag_10s_2_medium		
Acquisition Algorithm:	AMA	**Simulations:**	25
Successful Identifications:	100.00 % (3/3)	**Mean Identification Quality:**	88.89 %

Table 4.1: Overview of simulation parameters and test results for the current case

The *Off Centre Acquisition Test* was meant to demonstrate the acquisition system's ability to operate on arbitrary target locations on a CHEOPS full frame observation. This first case was configured to identify targets around a candidate area of 150 px around a central target location. Since acquisition with the *Magnitude Validation Algorithm* is generally independent of the target location, the *Angle Method Algorithm* was selected instead.
All three possible targets were correctly identified with an excellent average matching result of 92.59% matched fingerprints (Tab.: 4.1). Here, 2 out of 3 simulations achieved perfect identifications (Fig.: 4-5 right). The *acquisition accuracy* plot (centre) shows an alleged identification fail for case no. 9. Technically this was no AMA failure but can be attributed to not detected position, since the star was already deep in the margins of the *candidate area* and not expected to be found. For this reason, the data point got excluded from the results. If necessary, it can easily be identified with an increased candidate area. This will be configured accordingly, when such offsets are expected during live observations. In addition, a random star in simulation 0 triggered a relatively strong false positive with over 30% of matched fingerprints. This clearly shows why the algorithm can't just select the best result, but has to adhere to the primary success criterion.

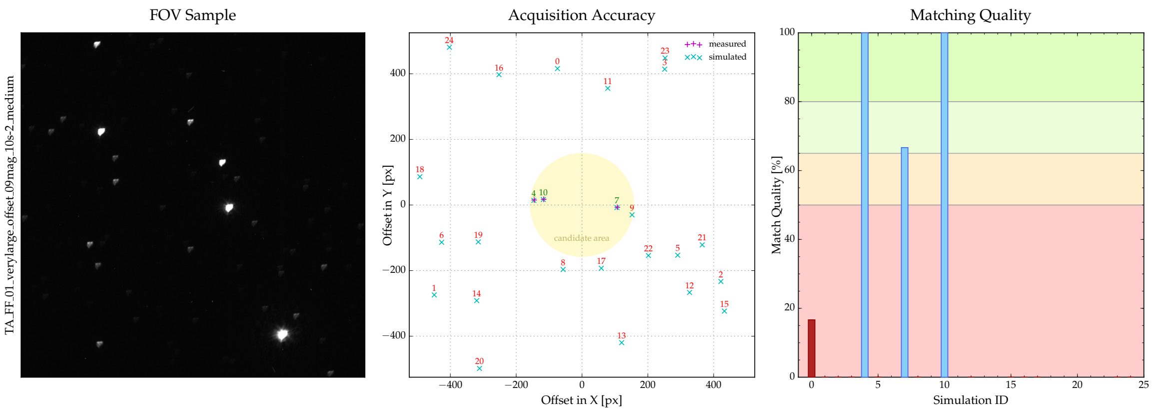

Figure 4-5: Sample FOV (no. 5) for the current test case (left), accuracy of identified target positions (middle), simulation specific matching results (right)

4.2.1.2 Corner Magnitude 9 Target, Medium FOV Population

Test Case:	TA_FF_01_verylarge_offset_09mag_10s-CORNER_2_medium		
Acquisition Algorithm:	AMA	**Simulations:**	25
Successful Identifications:	100.00 % (6/6)	**Mean Identification Quality:**	91.67 %

Table 4.2: Overview of simulation parameters and test results for the current case

The second case of the *Off Centre Acquisition Test* now actually features the off-centred target location. Again, every observation where a target star was detected in the candidate area resulted in a successful identification (Fig.: 4-6 centre). This extremely offset target location in the corner represents one of the challenging cases for the *Angle Method Acquisition*. For this, the reference stars have to be selected to also cover the currently not visible, but potential FOV to the right and below. While the observation specific match results (right) are all excellent for this star constellation, the interesting part are the false positives of the failed match attempts for simulations 4 and 10. Here the close proximity of their target locations causes similar algorithm behaviour and reveals the consistency of the method. Generally, the maximum target location shift is limited by the anticipated *pointing error* and hence the *candidate area* size, since it must always be entirely visible the FOV. Ignoring this requirement might lead to observations with an off screen target position. Therefore, it is recommended to keep the target location as close as possible to the image centre. The large offsets of the not detected targets also show how the expected target location has to be known at the time of Star Map creation to ensure successful identifications. Moreover, it is important to consider that actual observations with CHEOPS will feature FOV vignetting towards the corners, which must also not overlap with the candidate area. This feature is currently not present in *CHEOPSim* simulations.

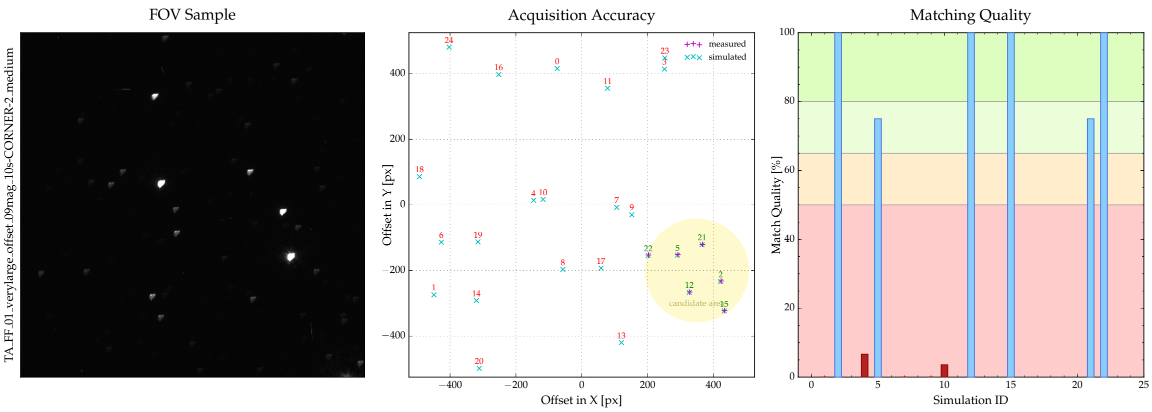

Figure 4-6: Sample FOV (no. 5) for the current test case (left), accuracy of identified target positions (middle), simulation specific matching results (right)

4.2.2 Large Offset Test

4.2.2.1 Magnitude 6 Target, Extreme FOV Population

Test Case:	TA_FF_01_large_offset_06mag_01s_3_extreme		
Acquisition Algorithm:	MVA	**Simulations:**	25
Successful Identifications:	100.00 % (23/23)	**Mean Identification Quality:**	88.87 %

Table 4.3: Overview of simulation parameters and test results for the current case

This test was targeted to investigate any unexpected dependencies between identification success and initial pointing error. Note, that it was also performed on FOV with 6 mag targets in low and medium populations, which produced almost identical results. For this reason, the subsequent discussion also applies to them.
The *FOV Sample* (left) shows that cases with such bright targets are relatively trivial to solve, since there usually won't be a second star of similar magnitude. Consequently, the identification success mostly depends on the correct prediction of the star signal and on accurate *Star Extraction*. Similar to earlier cases, all targets that were properly located within the candidate area could be identified (centre). Simulation 14 is an exception, that was again expected to fail due to the position in the outer margin of the candidate area. This failure turns out to be common for target positions in the outer right margin. The reason for this is the signal distribution in the PSF, for which the *Star Extraction* seems to introduce a slight shift to the right during the centroid detection. Although such behaviour was expected from early tests, it was only corrected for the centroiding report after the Target Acquisition and now has to be considered for the acquisition configuration. The *matching quality* plot (right) shows precisely measured star signals with a systematic offset of about 10% to the expected value. This was caused by outdated conversion tables for the signal calculation in *CHEOPSim* and has been addressed for new data.

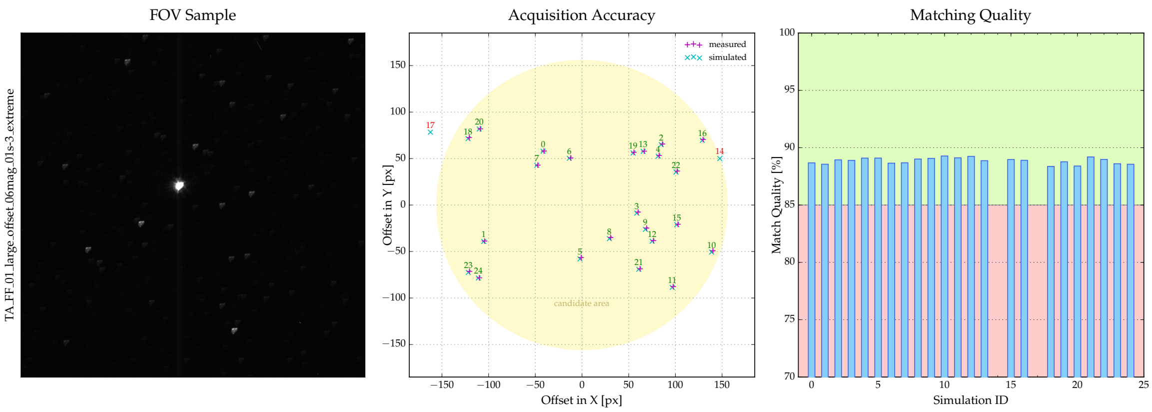

Figure 4-7: Sample FOV for the current test case (left), accuracy of identified target positions (middle), simulation specific matching results (right)

4.2.2.2 Magnitude 9 Target, Medium FOV Population

Test Case:	TA_FF_01_large_offset_09mag_10s_2_medium		
Acquisition Algorithm:	MVA	**Simulations:**	25
Successful Identifications:	100.00 % (24/24)	**Mean Identification Quality:**	87.46 %

Table 4.4: Overview of simulation parameters and test results for the current case

Like the *Magnitude Validation Acquisition* results before, the magnitude 9 target produced almost identical results for the low and medium FOV simulations and will not be discussed separately. The simulation results are very close to what was presented for the magnitude 6 targets in subsection 4.2.2.1. Although the *FOV Sample* (left) shows more bright targets, it does not introduce any ambiguity for a photometric identification. Generally, the presence of multiple comparatively bright objects in the narrow CHEOPS FOV is rare outside observations of star clusters. Therefore, it does not present a problem in the majority of such cases. Unlike previous cases, the *acquisition accuracy* plot (middle) features positively identified targets in the outer margins of the candidate area. This is possible, due to their location on the left, which is not negatively affected by the inherent right shift of the *Star Extraction*. The *matching quality* plot (right) again shows a similar precision and the systematic offset and is coherent with previous results. Unlike the 6 mag target observations, this case also allows extended exposure times without the risk of saturation, which in turn allows to resolve surrounding fainter objects. Therefore, this kind of FOV is also suited for target identifications with the *Angle Method Acquisition*. Consequently it can also be solved for observations outside the CHEOPS science requirements, that cannot be done with the photometric method. This is shown in the next test case.

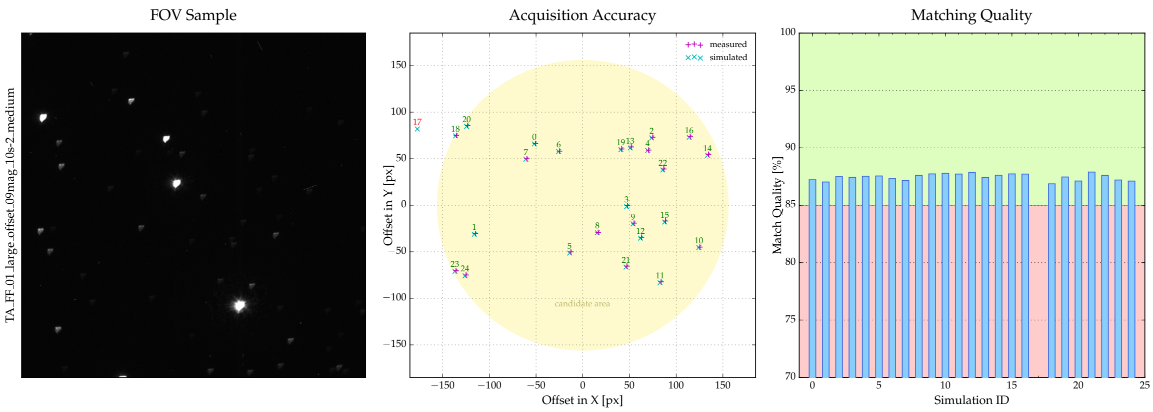

Figure 4-8: Sample FOV for the current test case (left), accuracy of identified target positions (middle), simulation specific matching results (right)

4.2.2.3 Magnitude 9 Target, Extreme FOV Population

Test Case:	TA_FF_01_large_offset_09mag_10s_3_extreme		
Acquisition Algorithm:	AMA	**Simulations:**	25
Successful Identifications:	100.00 % (24/24)	**Mean Identification Quality:**	91.23 %

Table 4.5: Overview of simulation parameters and test results for the current case

The *Angle Method Acquisition* is the best identification method when photometric identification is corrupted by overlapping signals from surrounding stars. An example for this is provided in the *FOV Sample* (Fig.: 4-9 left). Here the "central" bright star signal combines with a background star and therefore won't be recognisable through its signal estimate from the star catalogue.
While the *acquisition accuracy* plot (centre) is almost identical to the previous one, the *Matching Quality* plot layout (right) is new. The visualisation is a vertical version of the matching results in section 4.1.3.2. Successful identification results are classified as *excellent* (bright green), *good* (green) and *weak* (limegreen). Results below 50% are treated as *failed* (red). All of the correctly positioned targets were identified and most of them with excellent results. The slightly degraded matching quality in simulation 2 and 3 are most likely the consequence of an unfortunate overlap of the target and the above mentioned background star. This behaviour is rotation dependent and can introduce a slight offset to the detected target position, which interferes with the matching process.
It is noteworthy to mention, that the excellent results for this use case are mostly due to the exposure time of 10s, which is well within the optimal 5-15s range for identifications with the *Angle Method Algorithm*. This range is set to be the ideal trade off between being sufficiently long to clearly image fainter FOV stars while not being negatively affected by position overlaps from rotationally induced smearing.

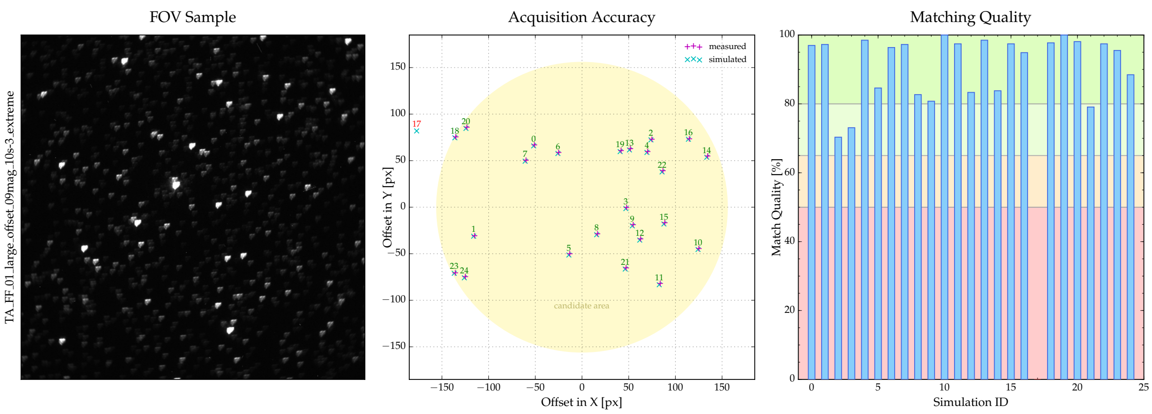

Figure 4-9: Sample FOV for the current test case (left), accuracy of identified target positions (middle), simulation specific matching results (right)

4.2.2.4 Magnitude 12 Target, Low FOV Population

Test Case:	TA_FF_01_large_offset_12mag_60s_1_low		
Acquisition Algorithm:	AMA	**Simulations:**	25
Successful Identifications:	87.50 % (21/24)	**Mean Identification Quality:**	92.38 %

Table 4.6: Overview of simulation parameters and test results for the current case

The test cases on magnitude 12 targets are the first ones that will only be identified by the *Angle Method Algorithm* to avoid a photometric misidentification with surrounding FOV stars. All of the magnitude 12 test cases are intended to stress the algorithm with the maximum possible exposure time of 60s, as this adds smearing and possible overlaps of FOV stars. The *FOV Sample* does indeed show strong smearing for stars with larger distances to the rotation axis. This should not pose a problem since the star positions will always be detected in the centre of each smeared signal, as long as reference stars don't combine or partly leave the FOV. The latter would lead to signal loss and as a consequence the star is below the detection threshold.

The majority of valid targets could be identified with an average *good* to *excellent* matching quality. Identifying the cause of the 3 failures is not too obvious at the first glance. Since the target star position and clear signal should make it an easy detection, the complete absence of any matching results simulations 5 and 12 suggests that there was an insufficient amount of stars for the *Angle Method Algorithm*. An inspection of the simulation log confirmed this. The best solution for this issue is a reduction of the detection threshold to enable the detection of further FOV stars. Note, that manual alterations to the detection threshold should not undercut the signal of the faintest reference star and possibly leave 2-3 reference stars below the new threshold (see section 3.1.3).

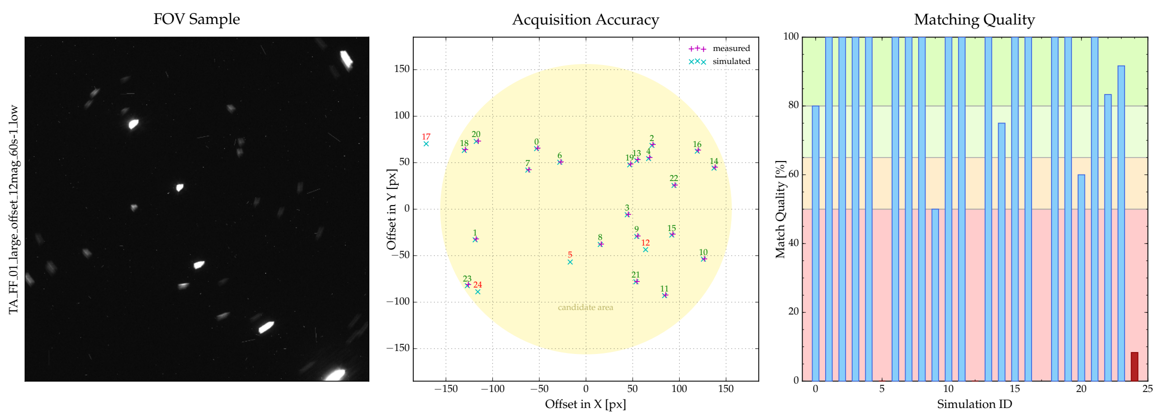

Figure 4-10: Sample FOV for the current test case (left), accuracy of identified target positions (middle), simulation specific matching results (right)

4.2.2.5 Magnitude 12 Target, Medium FOV Population

Test Case:	TA_FF_01_large_offset_12mag_60s_2_medium		
Acquisition Algorithm:	AMA	**Simulations:**	25
Successful Identifications:	95.83 % (23/24)	**Mean Identification Quality:**	65.12 %

Table 4.7: Overview of simulation parameters and test results for the current case

Compared to the previous simulation in section 4.2.2.4, the medium FOV populations partly eliminate problems, but also introduce new ones. While the identification issues from insufficient FOV stars disappeared due to a slightly increased number of detected stars, the average matching quality reduced drastically by almost 30%. Therefore, most results are placed in or close to the *weak* category. Simulations 3 and 21 fell below the general success criteria, whereas the latter could be validated with the secondary criteria as described in section 2.2.2.3. Close inspection of the simulation logs reveals that the general number of detected stars (5-10) in the observations was often quite low, even though the number of FOV stars increased compared to the previous test case. At this level, single misdetections can have large impacts on the matching results (see section 2.2.2.3), which was ultimately the reason for the degraded results and failures. Again, the manual adjustment of the *detection threshold* will result in more detected stars and therefore improve the matching qualities. Generally, this behaviour depends on the individual star population. Since the *Star Map Generation Tool* was designed according to the brightness model in section 4.1.1, it assumes a workable number of stars above the magnitude 12 target. This will not necessarily be met for faint populations or cases where some stars are lost due to the effects of strong rotation and smearing. Having identified this issue for the faint observational cases, it was treated in an updated version, where the star selection algorithm was improved.

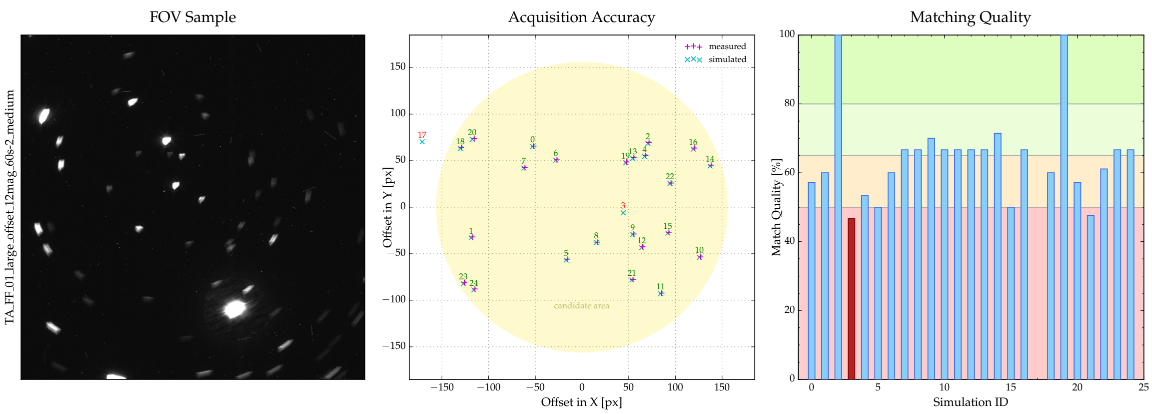

Figure 4-11: Sample FOV for the current test case (left), accuracy of identified target positions (middle), simulation specific matching results (right)

4.2.2.6 Magnitude 12 Target, Extreme FOV Population

Test Case:	TA_FF_01_large_offset_12mag_60s-ALT2_3_extreme		
Acquisition Algorithm:	AMA	**Simulations:**	25
Successful Identifications:	58.33 % (14/24)	**Mean Identification Quality:**	58.37 %

Table 4.8: Overview of simulation parameters and test results for the current case

The simulations for the magnitude 12 target with extreme FOV populations and with 60s exposure times are especially interesting. However, they came with a few problems, that needed manual adjustments of the *Star Map*. While the high star density and thereby resulting position overlaps lead to difficulties with the *Angle Method Acquisition*, the main issue is the slightly overlapping, close proximity neighbour to the target star. This positional arrangement inhibits scientifically meaningful photometric measurements and is not relevant for the anticipated observations with CHEOPS. Nonetheless, it represents a FOV that is crowded enough to be plagued by matching problems, due to bad positions from joint detections. For this reason, in order to enable any positive target identifications, the reference stars from the star catalogue had to be replaced with the detected joint star positions from the *Target Acquisition Performance Simulation* (see section 3.3). The second special feature is the crowded FOV with *candidate areas* containing more reference stars than can be provided for the acquisition. This leads to guaranteed identification failures, since all additionally detected stars negatively affect the result as interlopers. As a consequence, the candidate area is automatically reduced, which can be the cause of non-identifications if the pointing error cannot be reduced accordingly. This has been the cause for the failures of simulations 10, 14, 16, 18, 20, 23 and 24. In this particular case, the candidate area reduction was triggered by an outdated and too restrictive condition, that was relaxed for improved results in the latest version of the *SMGT*.

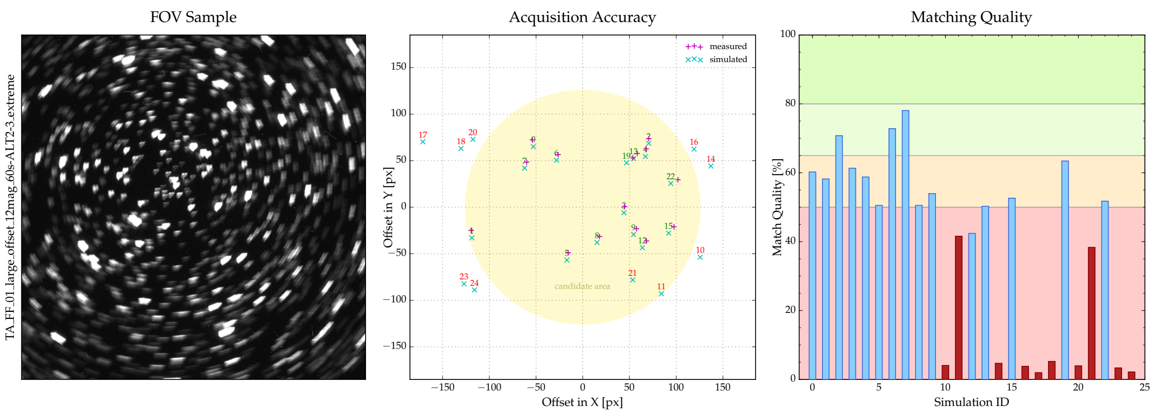

Figure 4-12: Sample FOV for the current test case (left), accuracy of identified target positions (middle), simulation specific matching results (right)

4.2.3 True Jitter Precision Test

4.2.3.1 Magnitude 9 Target, Extreme FOV Population

Test Case:	TA_FF_01_true_jitter_09mag_10s_3_extreme		
Acquisition Algorithm:	AMA	**Simulations:**	25
Successful Identifications:	100.00 % (25/25)	**Mean Identification Quality:**	76.92 %

Table 4.9: Overview of simulation parameters and test results for the current case

The *True Jitter Precision Test* was meant to identify potential identification issues that stem from the additionally introduced star motion caused by the spacecraft jitter. The simulated test cases are built from the same sky as the non-jittered versions, but feature different FOV orientations. Since the photometric identification with the *Magnitude Validation Algorithm* is not affected by small position offsets, it produces almost identical results as in the previous cases without jitter (section 4.2.2.2). For this reason, they will not be discussed separately. The results for the medium FOV population are included in this section, due to their similarity to the ones with the extreme population FOV.
The *acquisition accuracy* plot (centre) shows a systematic offset, between the measured and the real centroid, of 1.54 ± 0.14 px to the top right. This is in line with the previously detected systematic shift and the *Star Extraction* performance in section 4.1.2. It is most likely caused by cancellation effects of the random jitter motion that is present at short time scales. Even though the extracted centroids are not directly affected, the *match quality* plot (right) shows degradation of about 20% compared to the jitter free results in section 4.2.2.2. This can indeed be attributed to the jitter induced motion and is caused by slightly smeared PSFs, which favour the detection of joint star positions. Overall it should not cause major problems, since the acquisition was always designed with this effect in mind and on it average still produces *good* matching results.

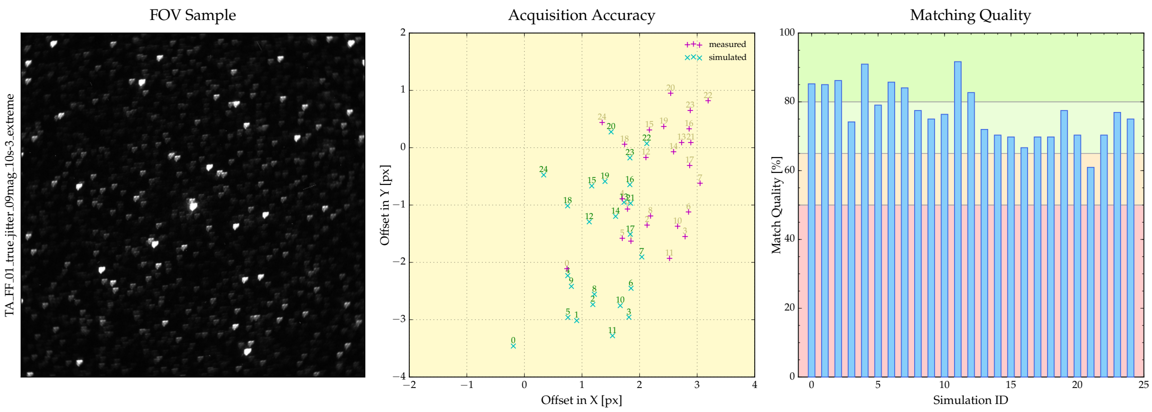

Figure 4-13: Sample FOV for the current test case (left), accuracy of identified target positions (middle), simulation specific matching results (right)

4.2.4 SAA Extreme Cosmic Ray Test

4.2.4.1 Magnitude 9 Target, Medium FOV Population, 1000x Cosmic Ray Rate

Test Case:	TA_FF_01_true_jitter_09mag_10s_CR1000x_2_medium		
Acquisition Algorithm:	AMA	**Simulations:**	25
Successful Identifications:	100.00 % (25/25)	**Mean Identification Quality:**	87.08 %

Table 4.10: Overview of simulation parameters and test results for the current case

The *SAA Extreme Cosmic Ray Test* was meant to assess the possibility to acquire new targets during passages through the South Atlantic Anomaly. For this purpose, the magnitude 9 target in medium FOV population was simulated with 100x and 1000x of the nominal cosmic ray (CR) rate for the CHEOPS orbit. The 100x CR observations could be identified with an average matching quality of 90.47% and won't be discussed separately due to their similarity to the previous cases with normal cosmic ray rates.

The acquisition on 1000x CR observations initially failed on every FOV with the automatically generated *Star Maps*. This was caused by unexpected detections of faint interlopers, that were not considered for the reference stars. These only exceeded the detection threshold by the additional signal deposition from the heavy CR bombardment. Manually increasing the detection threshold to values that prevent false positive detections fixes the acquisition for such extreme cases. While this resulted in a 100% success rate with *good* to *excellent* results, it has to be known in advance to acquire targets in such harsh environments. Since the additional signal possibly interferes with the high precision photometry, acquisition under such conditions will be the exception. To ensure acquisition success under moderate cosmic ray rates, the detection threshold calculation considers the signal deposition up to a 150x increased CR rate, to prevent the accidental detection of interlopers. More information on the CR signal can be found in section 3.1.4.

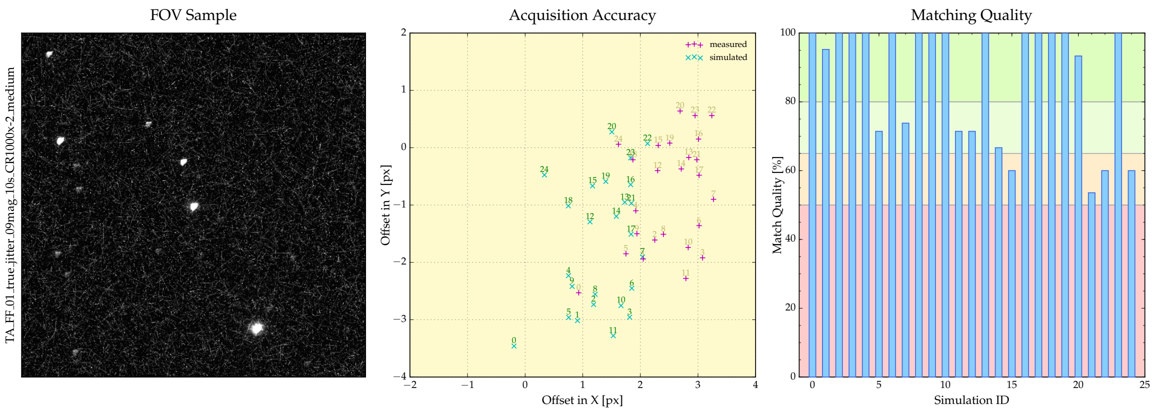

Figure 4-14: Sample FOV for the current test case (left), accuracy of identified target positions (middle), simulation specific matching results (right)

4.2.5 Maximum Rotation Test

Test Case:	TA_FF_01_true_jitter_12mag_60s_MAXROT_3_extreme		
Acquisition Algorithm:	AMA	**Simulations:**	50
Successful Identifications:	80.00 % (40/50)	**Mean Identification Quality:**	50.02 %

Table 4.11: Overview of simulation parameters and test results for the current case

The *Maximum Rotation Test* was intended as a worst case scenario to bring the *Angle Method Acquisition* to its limits and ultimately case it to fail for the majority of simulations. The simulation is based on the jittered version of the magnitude 12 target in the extremely crowded FOV with 60s exposure time and maximum FOV rotation rate.
The *FOV Sample* clearly shows the strong smearing effects and commonly joining star signals in the outer regions. To make things even worse, the target also partly overlaps with its closest background star. While the automatic configuration was never intended to solve anything like this and initially failed, manual adjustments to the configuration actually resulted in surprisingly good results with an 80% successful identification rate. Therefore, the reference stars were again replaced with the detected positions from the simulation. In addition, the *Star Extraction Radius* was reduced to exclude extremely smeared objects on the side. This achieved weak but positive results for 38% of the observations. The remaining successful 42% were validated by the secondary success criterion. It is noteworthy, that even though the remaining 20% failed both success criterion, they also correctly identified the target. The large average offset of 6.56 ± 2.28 px, as can be seen in the *acquisition accuracy* plot (centre), is caused by the combined position of the target and its neighbour star. Even though an acquisition to the combined position would be possible it will most likely not have any practical use, due to the corrupted photometric data of the target star.

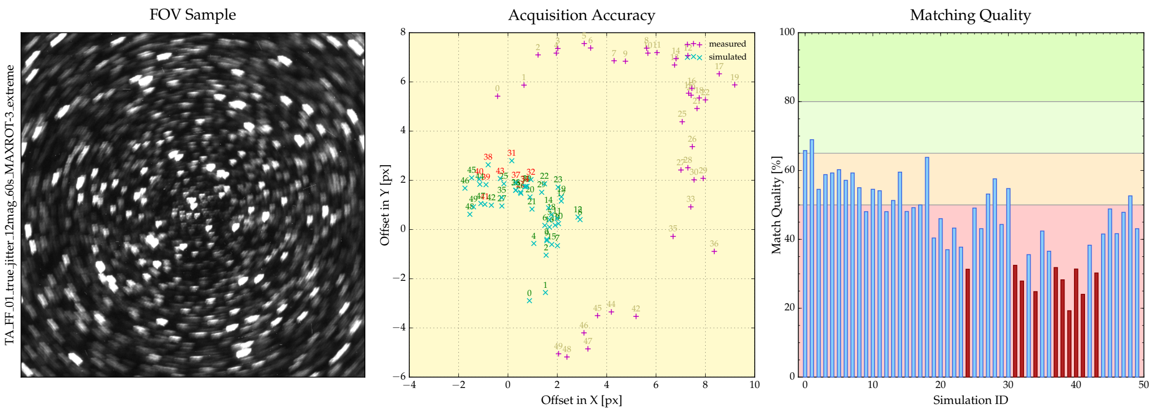

Figure 4-15: Sample FOV for the current test case (left), accuracy of identified target positions (middle), simulation specific matching results (right)

4.2.6 Execution Times

In addition to the PC based tests for the *Target Acquisition* C-code, the performance tests were also executed on the *Data Processing Unit* (DPU) of the CHEOPS engineering model. The DPU is built around the GR712RC Dual-Core LEON3FT SPARC V8 processor, which is derived from a *reduced instruction set computer* (RISC) lineage and adapted for the operation in the radiation intense space environment. Even though the stock processor is capable of a 100 MHz clock speed, it has been reduced to 25 MHz, which has the advantage of reduced heat emissions and a synchronised operation with the SRAM. To meet the execution time requirements of three seconds (Tab.: 1.2), the processing power of the 2^{nd} core and double-precision high performance floating-point unit will be dedicated to this software during Target Acquisition operations.

The execution times for the different Acquisition Algorithms in the *Large Offset Tests* (section 4.2.2) can be seen in Tab.: 4.12, 4.13 and 4.14. Depending on the identification algorithm the *Target Acquisition* took a total of approximately 1.74s to 1.95s:

- A close inspection shows that the times are mainly dominated by the *image retrieval* ($\sim$ 0.87s) and *Star Extraction* ($\sim$ 0.82s), which are both limited by the memory access of the full frame image.
- The pure *Angle Method Acquisition* ($\sim$ 0.06s) is the fastest method for easy conditions in uncrowded FOV (Tab.: 4.12). Here the *candidate area* will not contain many stars besides the target, which results in a small *Observed Star Database* and therefore less memory access.
- Crowded conditions like in Tab.: 4.14 on the other hand produce larger databases and significantly slow down the *Angle Method Acquisition* execution time ($\sim$ 0.25s). In this case, the successive *Magnitude Validation* ($\sim$ 0.03s) brings the overall acquisition time down to a total of 1.94s.
- Lastly, the *Magnitude Validation Acquisition* is slow due to memory intense photometric measurements on the full frame image. Depending on the number of *target candidates*, execution times can vary from $\sim$ 0.03s (single radius photometry) to $\sim$ 0.24s. The time can be reduced to the value of a single radius photometry if the *detection thresholds* is configured to only detect the target star. This was implemented as the default for the latest version of the *Star Map Generation Tool*.

Overall the execution time tests produced excellent results, where the obtained times were far below the targeted three second requirement.

	Function	# of executions		max execution time [s]
		total	per frame (~)	
a	**TargetAcquisition**	25	1	**1.734657**
b	**CropCopyFromSibAndUnpack**	25	1	**0.87758**
c	**star_extraction**	25	1	**0.802931**
d	**angle_method_acquisition**	25	1	**0.056264**
e	target_magntitude_validation_acquisition	0	0	0.000000
f	target_magnitude_validation	0	0	0.000000
g	create_ref_DB	23	1	0.014713
h	create_obs_DB	23	1	0.008610
I	match_databases	23	1	0.030736
j	determine_match_quality	23	1	0.000018
k	calculate_target_shift_AMA	3	0	0.000009
l	rebin_image	25	1	0.673981
m	find_pixel_of_interest	25	1	0.011325
n	calculate_distance	0	0	0.000000
o	group_pixel_of_interest	50	2	0.001383
p	reduce_to_average_pixel_of_interest	25	1	0.056372
q	reduce_to_brightest_pixel_of_interest	25	1	0.059226
r	sort_group_after_brightest_pixel	224	9	0.000018
s	calculate_center_of_gravity	25	1	0.000713
t	find_target_candidates	23	1	0.000028
u	calculate_dAng	348	14	0.000080
v	stretch_fingerprint	696	28	0.000011
w	find_base0	644	26	0.000035
x	find_base1	17388	695	0.000028
y	find_matches	17388	695	0.000037
z	find_majority_matches	23	1	0.001698
aa	find_unique_matches	1932	77	0.000030
ab	correct_multiple_base_matches	23	1	0.000052
ac	find_valid_star_candidate	23	1	0.000179
ad	perform_radius_photometry	0	0	0.000000

Table 4.12: Execution times for the 9 mag target in a medium FOV population with the *Angle Method Acquisition*. Top-level functions (bold) contain the execution times of their sub-routines, e.g. the execution time given for *TargetAcquisition* is the cumulative total of all function calls.

	Function	# of executions total	per frame (~)	max execution time [s]
a	**TargetAcquisition**	25	1	**1.948299**
b	**CropCopyFromSibAndUnpack**	25	1	**0.877595**
c	**star_extraction**	25	1	**0.841365**
d	angle_method_acquisition	0	0	0.000000
e	**target_magntitude_validation_acquisition**	25	1	**0.240547**
f	target_magnitude_validation	0	0	0.000000
g	create_ref_DB	0	0	0.000000
h	create_obs_DB	0	0	0.000000
I	match_databases	0	0	0.000000
j	determine_match_quality	0	0	0.000000
k	calculate_target_shift_AMA	0	0	0.000000
l	rebin_image	25	1	0.674649
m	find_pixel_of_interest	25	1	0.011657
n	calculate_distance	877	35	0.000010
o	group_pixel_of_interest	50	2	0.024542
p	reduce_to_average_pixel_of_interest	25	1	0.071466
q	reduce_to_brightest_pixel_of_interest	25	1	0.056731
r	sort_group_after_brightest_pixel	899	36	0.000018
s	calculate_center_of_gravity	25	1	0.002186
t	find_target_candidates	0	0	0.000000
u	calculate_dAng	0	0	0.000000
v	stretch_fingerprint	0	0	0.000000
w	find_base0	0	0	0.000000
x	find_base1	0	0	0.000000
y	find_matches	0	0	0.000000
z	find_majority_matches	0	0	0.000000
aa	find_unique_matches	0	0	0.000000
ab	correct_multiple_base_matches	0	0	0.000000
ac	find_valid_star_candidate	0	0	0.000000
ad	perform_radius_photometry	149	6	0.028441

Table 4.13: Execution times for the 6 mag target in a medium FOV population with the *Magnitude Validation Acquisition*. Top-level functions (bold) contain the execution times of their sub-routines, e.g. the execution time given for *TargetAcquisition* is the cumulative total of all function calls.

	Function	# of executions total	per frame (~)	max execution time [s]
a	**TargetAcquisition**	25	1	**1.957253**
b	**CropCopyFromSibAndUnpack**	25	1	**0.877222**
c	**star_extraction**	25	1	**0.813921**
d	**angle_method_acquisition**	25	1	**0.245184**
e	target_magntitude_validation_acquisition	0	0	0.000000
f	**target_magnitude_validation**	3	1	**0.028386**
g	create_ref_DB	25	1	0.005351
h	create_obs_DB	25	1	0.171364
I	match_databases	25	1	0.062379
j	determine_match_quality	25	1	0.000017
k	calculate_target_shift_AMA	14	1	0.00001
l	rebin_image	25	1	0.675639
m	find_pixel_of_interest	25	1	0.020046
n	calculate_distance	3172	127	0.000015
o	group_pixel_of_interest	50	2	0.002377
p	reduce_to_average_pixel_of_interest	25	1	0.059248
q	reduce_to_brightest_pixel_of_interest	25	1	0.05678
r	sort_group_after_brightest_pixel	526	21	0.000013
s	calculate_center_of_gravity	25	1	0.001278
t	find_target_candidates	25	1	0.000055
u	calculate_dAng	27000	1080	0.000085
v	stretch_fingerprint	54000	2160	0.000012
w	find_base0	425	17	0.000123
x	find_base1	6800	272	0.000282
y	find_matches	6800	272	0.000274
z	find_majority_matches	25	1	0.004701
aa	find_unique_matches	1275	51	0.000119
ab	correct_multiple_base_matches	25	1	0.000238
ac	find_valid_star_candidate	25	1	0.000174
ad	perform_radius_photometry	3	1	0.028346

Table 4.14: Execution times for the 12 mag target in an extreme FOV population with the *Angle Method Acquisition* and *Magnitude Validation*. Top-level functions (bold) contain the execution times of their sub-routines, e.g. the execution time given for *TargetAcquisition* is the cumulative total of all function calls.

4.2.7 Performance Test Conclusions

The *Performance Test Campaign* demonstrated the robustness of the acquisition algorithms under various conditions, that represent the typical future observational cases. These include

- Acquisition in far off-centred target locations
- Acquisition of targets with magnitudes within the science requirements (Tab.: 1.1)
- Acquisition of targets with large offsets from their intended target location
- Acquisition of targets within extreme cosmic ray environments
- Acquisition of targets in periods of maximum FOV rotation

In all tests it was possible to identify the target star in the majority of the orientations. Due to the excellent execution times, that surpassed the Target Acquisition requirements (Tab.: 1.2), no further attempts to optimise the *Observed Star Database* access have been made.

Generally, the results were used to develop problem solving strategies, as outlined for the respective test cases above. They ultimately led to many improvements in the star selection process as well as general bug fixes for the final version of the *Star Map Generation Tool*. An assessment of its ability to automatically configure the *Target Acquisition* for the majority of CHEOPS science observations is subject of the final section of this chapter.

4.3 Science Case Test Campaign

After the successful demonstration of the acquisition abilities in the previous test, the *CHEOPS Science Team GTO target list* [CHEOPS Science Team, 2017] was automatically configured and evaluated with the *Star Map Generation Tool*. This currently contains 492 potential science targets, that have been proposed for observations with CHEOPS. Given that the input data are valid, it was expected that the vast majority of them will result in correct target identifications. Therefore, the main focus of this test was to determine the amount of cases that will require manual adjustments to the configuration.
The results can be seen in the three histograms in Fig.: 4-16 and Tab.: 4.15 below. All magnitude data have been rounded to the nearest integer. The combined statistics (left) show a significant fraction of unsuccessful acquisitions between magnitudes 8 and 10. A closer look to the algorithm specific results (center and right) shows that the majority of these problematic cases stem from acquisition configurations featuring the *Magnitude Validation Algorithm*. Here a dramatic 109 out of 141 cases failed. This turns out to be an issue with

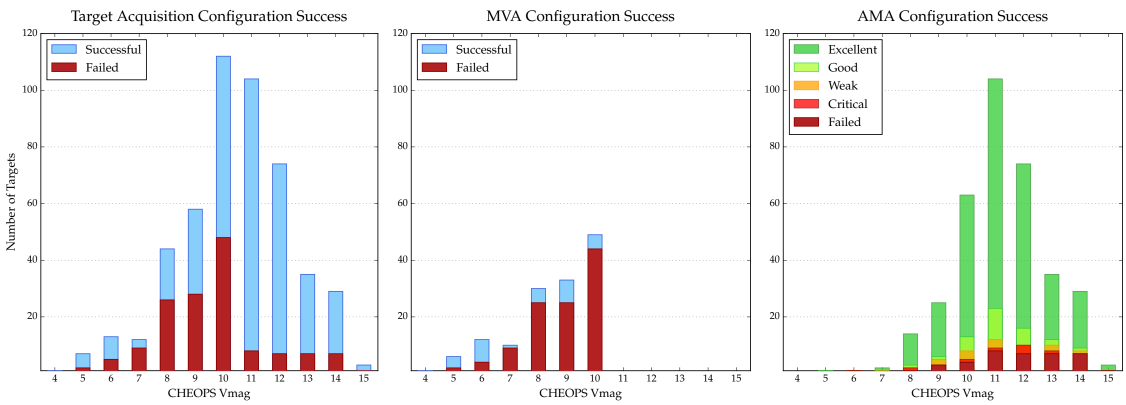

Figure 4-16: Combined target magnitude specific acquisition statistics (left), Magnitude Validation Acquisition specific statistics (center) and Angle Method Acquisition specific statistics (right). The latter also shows the frequency of achieved match qualities.

the provided star catalogues, rather than an algorithmic one. The behaviour is triggered by duplicate target entries in the catalogue, which can stem from two sources. Some objects in the Gaia catalogue have a very high proper motion and might have been overlooked by a filter process during the creation of the catalogue. These objects could easily be identified since their magnitudes were identical for the inspected cases. However, the vast majority was a direct consequence of incorrectly provided user inputs from the web-based CHEOPS observation request form. These happen when the target star ephemeris and brightness information are added manually instead of being taken from the respective Gaia objects. As a consequence, both the position and the magnitude can vary from the Gaia values to such a degree, that an automated filtering process to reliably identify duplicates from legitimately added objects becomes a challenge. If left uncorrected, the object will be integrated twice during the *Test Data Generation* and therefore not match with the expected reference target signal. While such a configuration could work in a real observation with a correctly imaged target, the duplicate entries are still problematic for two reasons:

- They cause it to fail the automated configuration process and require additional attention from the operation scientist, which can be very time consuming.
- They can interfere with the proper selection of the acquisition algorithm, as bright objects can easily be identified with the *Magnitude Validation Acquisition* as long as the target magnitude is unique within the provided tolerance. A duplicate entry will fail this condition and lead to a configuration with the *Angle Method Acquisition*, which is not always appropriate for the brightest targets.

Since this data set is not suited to determine the rate of reliably configured observations, a filter for duplicate entries was implemented. It removes catalogue entries in close proximity of the target star if the duplicates are within a distance of one PSF diameter (~ 24px) and 0.35 mag. These values are selected to represent common magnitude discrepancies amongst duplicates and are supported by the requirement for isolated high precision photometry. The filtered results are presented in Fig. 4-17 below. The new data shows a clear

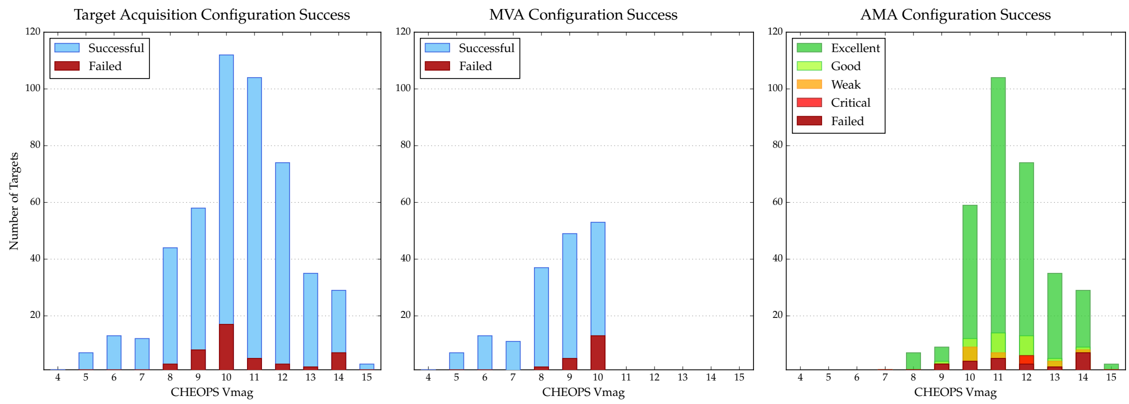

Figure 4-17: Combined target magnitude specific acquisition statistics (left), Magnitude Validation Acquisition specific statistics (center) and Angle Method Acquisition specific statistics (right). The latter also shows the frequency of achieved match qualities.

improvement in *Magnitude Validation Acquisition* success (center) to 149 out of 171 simulations. A close inspection of the remaining 22 fails shows that magnitude differences of duplicates can go up to 0.57 mag, which makes their unambiguous identification and filtering difficult. Within those failed cases only 4 seemed to have a real overlapping star. While this would improve the success rate up to 97.7 % it cannot be considered as exact, due to the coarse nature of the implemented filter algorithm. Furthermore, close comparison of the algorithm specific results shows that a total of 30 cases from magnitudes 8-10, that were initially configured for acquisition with the *Angle Method Algorithm* (Fig.: 4-16 right), are now properly assigned to the *Magnitude Validation Algorithm* (Fig.: 4-17 center).

With a large fraction of the anticipated science cases around and beyond targets of 10^{th} magnitude, the *Angle Method Acquisition* will be used in the majority of observations. Since most of the duplicate entries overlapped well within a PSF radius, they hardly affected the target centroid and therefore did not interfere with the acquisition. To ensure the filter did not manipulate the matching results, all star catalogues of failed cases were manually inspected to verify that no unwanted removal of real overlapping FOV stars took place.

Data Set	**Algorithm**	SUCC		EXLT	GOOD	WEAK	CRIT	FAIL	
	MVA	32	22.70 %					109	77.30 %
Unfiltered	AMA	312	88.89 %	265	28	12	7	39	11.11 %
	Total	**344**	**69.92 %**					**148**	**30.08 %**

Data Set	**Algorithm**	SUCC		EXLT	GOOD	WEAK	CRIT	FAIL	
	MVA	149	87.13 %					22	12.87 %
Filtered	AMA	294	91.59 %	261	20	10	3	27	8.41 %
	Total	**443**	**90.04 %**					**49**	**9.96 %**

Table 4.15: GTO Target List acquisition results with and without duplicate filtering.

The *AMA Configuration Success* (Fig.: 4-16 & 4-17 right, Tab.: 4.15) shows excellent results with and without the duplicate filter. For the filtered observations only 30 out of 321 cases (9.35 %) either fall into the *failed* (27) or *critical* (3) category, where latter indicates an identification with the secondary success criterion. Another 10 cases (3.21 %) were considered to be *weak* results and should be manually adjusted to improve. Generally, most of the identification problems appeared in simulations for the faint magnitude 14 targets. Even though they fall outside of the requirements upon which the *Star Map Generation Tool* was designed, they seem to be unproblematic as long as the target can be observed isolated from its neighbours. Finally, the most surprising result are the 3 magnitude 15 targets, which were identified within the *excellent* category. While a sample of 3 is not large enough for reliable predictions, it shows that isolated faint targets should indeed be observable. Overall a vast majority of 261 simulations (81.31 %) produced *excellent* results, which is closely followed by another 20 (6.23 %) *good* ones. Since everything that matched better than the *weak* category should be reliable without additional input, a staggering 87.54 % of the *Angle Method Acquisition* preparation could be automatically configured. Together with the above estimated 2.3 % of problematic cases with the *Magnitude Validation Acquisition* this is an outstanding result. Given that the issue of duplicate inputs will be solved, it can be seen as a strong indication for smooth and intervention free operation in the future.

5 Conclusion

This thesis presented the implementation and performance testing of an identification based *Target Acquisition* system for the CHEOPS mission. What was initially planned to be the development of an on-board algorithm, evolved into a project for the fully-fledged *Star Map Generation Tool*[1], that includes automated acquisition preview simulations for the configuration parameter verification of each observation.

After an in-depth description of the inner workings for the *Star Extraction*, *Angle Method Acquisition* and *Magnitude Validation Acquisition*, the focus shifted to the various test series over which the software constantly evolved to guarantee reliable operation in various observational environments. While their detailed results are presented in the respective conclusion sections, it is worthwhile to repeat that the acquisition will be successful without additional operator intervention in up to 91 % of the currently considered observations, which also includes various targets below the faintest required magnitudes. The remainder should either be possible after manual parameter fine tuning or suffers from FOV characteristics, that are incompatible with the design to the CHEOPS science requirements. Given that the acquisition software can only be as good as its input data, it is a prerequisite to address the currently known issues to achieve the anticipated results for live operations. These include the multiple entries in the provided star catalogues and the conversion of the Gaia visual magnitudes to CHEOPS ADU, which both have to be solved by their responsible parties. Furthermore, the distortion correction could only be tested with the *Star Map Generator Tool* internal simulations, as *CHEOPSim* lacks the capability to simulate it. Therefore, it is strongly advised to have this verified from an independent source. Since the science team is aware of the above issues, they should be addressed until

[1] The current version of the on-board *Target Acquisition* software and the *Star Map Generation Tool* is available under the GPLv2 license through the University of Vienna.

the launch of CHEOPS in late 2018, to enable for smooth operations with the optimal use of the *Target Acquisition* software.

In the spirit of the traditional space industry approach of reusing and improving upon existing flight proven technology, I will conclude this thesis with an outlook on potential software upgrades for future applications

- While the star identification algorithm can be used for any application with similar FOV characteristics, the *Star Extraction* was designed to specifically work with the defocused CHEOPS optics. For this reason, an update to accepting arbitrary image dimensions and PSF diameters will be a necessity for future reuse.
- Another improvement to the *Star Extraction* would be an improved calculation of the background signal, especially the bias and dark current of the image. This can easily be done by photometric standard techniques or dedicated CCD areas as are the case in CHEOPS, but were not used due to stringent execution time requirements and slow memory access.
- Regarding the feature database creation of the *Angle Method Acquisition*, a potential improvement to the database size could be the inclusion of the target magnitude for the selection of *target candidates*. This would be an easy approach to reduce search times in crowded cases by entirely avoiding the creation of the feature database for stars that thereby could easily be excluded as a potential target.
- The other approach to a reduction of database search times would be an adoption of database sorting or *k-vector* method, as introduced for various identification techniques in the opening chapter.
- Last but not least, the current command line based usage can be upgraded by the addition of a graphical user interface, that provides the ability to manually change the *Reference Star* selection and other input parameters. In combination with the option for side-by-side comparison of the preview simulations, the usability of the *Star Map Generation Tool* can be drastically improved.

Bibliography

Observing with CHEOPS, 2018. https://www.cosmos.esa.int/web/cheops/observing-with-cheops1 [Accessed: 16.04.2018].

P. Alvelda and A. M. S. Martin. Neural network star pattern recognition for spacecraft attitude determination and control. In D. S. Touretzky, editor, *Advances in Neural Information Processing Systems 1*, pages 314–322. Morgan-Kaufmann, 1989. 1.1.3

D. Baldini, M. Barni, A. Foggi, G. Benelli, and A. Mecocci. A new star-constellation matching algorithm for satellite attitude determination. *ESA Journal*, 17:185–198, 1993. 1.1.1

W. Benz, D. Ehrenreich, and C. Broeg. *CHEOPS Definition Study Report (Red Book)*. ESA, 2013. URL http://sci.esa.int/cosmic-vision/53541-cheops-definition-study-report-red-book/. 1, 1.2, 1.2.1, 1.1, 1-6, 1-7, 2.3.3.1

E. Bertin and S. Arnouts. SExtractor: Software for source extraction. *Astronomy and Astrophysics*, 117:393–404, June 1996. doi: 10.1051/aas:1996164. 2.1

N. Billot and D. Futyan. *ReadMe File for the REF_APP_FluxConversion*. University of Geneva, 2017. 3.2.3, 3.2.3

T. Brady, C. Tillier, R. Brown, A. Jimenez, and A. Kourepenis. The inertial stellar compass: A new direction in spacecraft attitude determination. 01 2002. 1.1.3

CHEOPS Science Team. CHEOPS Science Team GTO Target List, 2017. 4.3

G. B. Crew, R. Vanderspek, and J. Doty. Hete experience with the pyramid algorithm. 2002. 1.1.3

J. H. J. de Bruijne. Science performance of Gaia, ESA's space-astrometry mission. *Astronomy and Astrophysics*, 341:31–41, Sept. 2012. doi: 10.1007/s10509-012-1019-4. 2.2.1.2

R. Ferstl. Optimised Centroiding of Stars for Space Applications. Master's thesis, University of Vienna, Department for Astrophysics, 2016. 3.2, 3.2.4

D. Futyan. CHEOPSim *User Guide*. CHEOPS Science Team, March 2018. compatible with *CHEOPSim* release r_9.2. 3.1.4, 3-3

E. J. Groth. A pattern-matching algorithm for two-dimensional coordinate lists. *The Astrophysical Journal*, 91:1244–1248, May 1986. doi: 10.1086/114099. 1.1.1

J. Hong and J. A. Dickerson. Neural-Network-Based Autonomous Star Identification Algorithm. *Journal of Guidance Control Dynamics*, 23:728–735, July 2000. doi: 10.2514/2.4589. 1.1.3

J. D. Hunter. Matplotlib: A 2d graphics environment. *Computing In Science & Engineering*, 9(3):90–95, 2007.

E. Jones, T. Oliphant, P. Peterson, et al. SciPy: Open source scientific tools for Python, 2001–. URL http://www.scipy.org/. [Online; accessed 01.04.2018].

J. L. Junkins, C. C. White, III, and J. D. Turner. Star pattern recognition for real time attitude determination. *Journal of the Astronautical Sciences*, 25:251–270, 1977. 1.1.1

W. Larson and A. Wertz. *Space Mission Analysis and Design*. Space Technology Library. Springer Netherlands, 2013. ISBN 9789401051927. URL https://books.google.at/books?id=lIGengEACAAJ. 1

D. W. Latham, T. M. Brown, D. G. Monet, M. Everett, G. A. Esquerdo, and C. W. Hergenrother. The Kepler Input Catalog. In *American Astronomical Society Meeting Abstracts*, volume 37 of *Bulletin of the American Astronomical Society*, page 1340, Dec. 2005. 4.1.1

C. C. Liebe. Pattern recognition of star constellations for spacecraft applications. *IEEE Aerospace Electronic Systems Magazine*, 7:34–41, June 1992. 1.1.1, 1-2, 1.1.3, 2.2

P. Loeschl, R. Ferstl, F. Kerschbaum, and R. Ottensamer. On-board target acquisition for CHEOPS. In *Software and Cyberinfrastructure for Astronomy IV*, volume 9913 of *SPIE Proceedings*, page 99132W, July 2016. doi: 10.1117/12.2232726. 2, 1

D. Mortari. A fast on-board autonomous attitude determination system based ona new star-id technique for a wide fov star tracker. 93:893–903, 01 1996. 1.1.2, 2.2

D. Mortari. Search-less algorithm for star pattern recognition. 45:179–194, 04 1997. 1.1.2

D. Mortari and B. Neta. k-vector range searching technique. *Advances in the Astronautical Sciences*, 105:449–464, 01 2000. 1.1.2, 1-4

D. Mortari, M. Samaan, C. Bruccoleri, and J. Junkins. The pyramid star identification technique. 51, 09 2004. 1.1.3

R. Ottensamer. CHEOPS optical distortion map. personal communication, 2016. 3-4

R. Ottensamer. CHEOPS-UVIE-TR-005-IFSW Performance Tests. Technical report, University of Vienna, 2017. 4.2

C. Padgett and K. Kreutz-Delgado. A grid algorithm for autonomous star identification. *IEEE Transactions on Aerospace Electronic Systems*, 33:202–213, Jan. 1997. doi: 10.1109/7.570743. 1.1.3, 1-5

B. M. Quine and H. F. Durrant-Whyte. A fast autonomous star-acquisition algorithm for spacecraft. 4:1735–1740, 12 1996. 1.1.2, 1-3

C. Reimers, R. Ferstl, F. Kerschbaum, P. Löschl, A. Luntzer, M. Mecina, and R. Ottensamer. Flight Software Development for CHEOPS, 9 2016. 2.2.2.3

T. P. Robitaille and Astropy Collaboration. Astropy: A community Python package for astronomy. *Astronomy and Astrophysics*, 558:A33, Oct. 2013. doi: 10.1051/0004-6361/201322068. 3.2.1

J. Salgado, J. González-Núñez, R. Gutiérrez-Sánchez, J. C. Segovia, J. Durán, J. L. Hernández, and C. Arviset. The ESA Gaia Archive: Data Release 1. *Astronomy and Computing*, 21:22–26, Oct. 2017. doi: 10.1016/j.ascom.2017.08.002. 2.2.1

P. M. Salomon and W. C. Goss, editors. *A microprocessor-controlled CCD star tracker*, Jan. 1976. 1.1.1

T. Sasaki and M. Kosaka. A star identification method for satellite attitude determination using star sensors. In *15th International Symposium on Space Technology and Science*, pages 1125–1130, 1986. 1.1.1

M. S. Scholl. Star-field identification for autonomous attitude determination. *Journal of Guidance Control Dynamics*, 18:61–65, Jan. 1995. doi: 10.2514/3.56657. 1.1.1

D. M. Shuster and S. Oh. Three-axis attitude determination from vector observations. 4, 03 1981. 1

B. B. Spratling and D. Mortari. A survey on star identification algorithms. *Algorithms*, 2 (1):93–107, 2009. ISSN 1999-4893. doi: 10.3390/a2010093. URL `http://www.mdpi.com/1999-4893/2/1/93`. 1.1, 1.1.3

T. E. Strikwerda and J. L. Junkins. Star pattern recognition and spacecraft attitude determination. *NASA STI/Recon Technical Report N*, 82, May 1981. 1.1.1, 1-1, 1.1.1, 2.2

M. Weiss. CHEOPS Image Distortion Correction. Bachelor's Thesis, University of Vienna, Department for Astrophysics, 2016. 3.2.2

G. Zhang. *Star Identification: Methods, Techniques and Algorithms*. Springer Berlin Heidelberg, 2016. ISBN 9783662537831. URL `https://books.google.at/books?id=VdrJDQAAQBAJ`. 1

G. Zhang, X. Wei, and J. Jiang. Full-sky autonomous star identification based on radial and cyclic features of star pattern. 26:891–897, 07 2008. 1.1.3, 2.2